UNIVERSITÀ
DEGLI STUDI
DI PADOVA

Head Office: University of Padova

Department of Information Engineering

Ph.D. COURSE IN: Information Engineering
CURRICULUM: Information and Communication Technologies (I.C.T.)
31th SERIES

A STUDY ON ORGANIC AND HYBRID EMERGING PHOTOVOLTAICS: MODELING AND RELIABILITY

Coordinator: Prof. Andrea Neviani
Supervisor: Prof. Andrea Cester

Ph.D. candidate: Antonio Rizzo

Contents

Abstract

Since the first observation of the photovoltaic phenomenon, photovoltaics underwent continuous improvement and evolution, expanding its market and applications worldwide. Photovoltaic solar cells can be classified into three generations depending on the technology used: single junction (multi) crystalline (1G), single junction thin film (2G) and hetero-junctions (3G). Organic and hybrid solar cells belong to the 3G generation. Low temperature and typographic printing processing, tunable colors, flexibility and short payback time are but a few of the advantages these technologies possess, making organic and hybrid photovoltaics appealing in terms of both cost and architectonic integration. An almost infinite number of organic and hybrid solar cells are possible, due the high number of combinations that organic chemistry provides. However, depending on the structure and materials used, these devices can be grouped into three categories: dye-sensitized, polymeric and perovskite solar cells. Despite the several advantages, organic and hybrid photovoltaics have lower efficiency, lifetime and reliability compared to inorganic technologies. The best performances single cell efficiency goes from 11.9% of dye-sensitized to 22.1% of perovskite solar cells. However, scaling the area while maintaining high performances is a complex process compared to inorganic PV, mainly due to the absence of industrial expertise. Furthermore, higher susceptibility to oxygen, moisture and UV radiation make organic and hybrid photovoltaics more vulnerable and less reliable than commercially available inorganic photovoltaics. All these issues must be addressed in order to improve the organic/hybrid solar cells efficiency, reliability, lifetime and market expansion.

We investigated the response of roll coated organic solar cells at different bias voltages and illumination levels to implement a detailed impedance model. The technique used for the investigation is based on the combination of standard DC characterization with the impedance spectroscopy at different bias and illumination intensity conditions. We analyzed both fresh and intentionally degraded cells. The impedance spectra show different peaks evolutions, depending on the degradation of the cells. Moreover, the same trend appears by measuring the cells at different illumination levels. To describe the cell impedance behaviors we suggest an electrical model based on distributed elements. By fitting the model to experimental data, we extrapolate the parameters related to electron transport, recombination and accumulation. The main differences between fresh and degraded samples are underlined. In addition, we subjected P3HT:PCBM solar cells to electrical constant current stress and thermal storage. We used the impedance spectroscopy technique combined to conventional DC measurements for device characterization during all stresses. We identified and separated different contributions affecting the open circuit voltage and short circuit current during both stresses. We calculated the photocurrent, measuring current voltage curves in both dark and light at each stress step. A model applied to photocurrent experimental data measured during the current stress allows the estimation of parameters such as generation, recombination, dissociation rate and nearly zero field voltage within the active layer as a function of the stress time. Several mechanisms are behind all these changes; in particular, extrapolated parameters show that the stress mainly affects the recombination rate of the polaron charge transfer states.

On hybrid solar cells, the anomalous electrical behavior of lead halide perovskite opto-electronic devices still prevents their full reliability. Though it is recognized a correlation with the presence of mobile ionic species within the perovskite layer, the phenomenon is still under debate. We report the characterization of methylammonium lead iodide perovskite nanocrystals with a graphitic material patching the nanocrystals surfaces produced by a laser ablation decomposition of an organic solvent on the surfaces of the precursor PbI_2. Electrical measurements indicate that the macroscopic ionic diffusion lowers within thin films based on this material. We show that an electronic coupling between

the nanocrystals and the graphitic material is present and we suggest a passivating effect, which produces a macroscopic reduction of ions motion.

Then, we studied the hysteresis and electric field effects on planar $CH_3NH_3PbI_3$ perovskite devices, synthetized from laser-ablated precursors, by means of electrical characterizations at different scan rates and optical measurements. The aim of our investigation is to characterize the phenomena behind perovskite degradation under prolonged applied electric field. Using a perovskite more resistant to electric field induced degradation, we run long time characterizations that were not accomplishable before. Thus, we distinguished all the degradation-involved phenomena. The results point to the presence of ions migrating in the perovskite when the device is biased. Our data showed that ions migration degrades the interfaces with the consequent creation of degraded layers that limit the current injected in the device and the extracted photocurrent. These layers where detected also by means of optical Raman characterization. In order to explain the details of the mechanisms concurring to the observed behaviors, we presented a qualitative model. The observed phenomena exacerbated by the planar structure are even more destructive on standard solution processed perovskites to which the results can be extended. The same degradation dynamics occur on vertical devices, typical on perovskite solar cells, and the obtained results provide a useful in-depth analysis of the ionic migration effects. Furthermore, we subjected to both storage and thermal stress solid state solar cells based on organ-metal perovskites and using Spiro-OMeTAD as hole transport material. We applied two different sealing techniques to encapsulate the devices, in order to study the differences during the experiment. Applying fast cycle-voltammetry, transient measurement and very slow DC measurements, we correlated the results obtained during the 540h experiment to different degradation dynamics within the cell structure. The correlation allows us to distinguish at least two possible sources of degradation that can help understanding loss mechanisms of perovskite solar cells.

Finally, accurate determination of the lifetime of novel hybrid and organic solar cells is often rather challenging due to very dynamic behavior of such cells over time and ageing curves with shapes of varying nature. Therefore, in order to accurately and reproducibility determine the lifetime of photovoltaic (PV) devices with such a behavior a novel elaboration algorithm was developed, which enables automatic smoothing, filtering and extrapolation of the real lifetime data and reproducibility determining the lifetime parameters defined in the ISOS guiding standards. The algorithm is also capable of predicting the lifetime of devices, not tested until the end of sample life, given that there is sufficient amount of measured data points for performing reliable extrapolation of ageing curves (to a limited time frame).

1 Introduction

The first observation of the photovoltaic principle was in 1839 by A.E. Becquerel who put two AgCl coated platinum electrodes into an acidic solution that under illumination generate current [1]. Photovoltaic technology evolved since Becquerel discovery and solar panels are distributed worldwide nowadays, with applications on huge photovoltaic plants as well as on small domestic power systems. However, the direct conversion of the solar radiation into electric energy is a business dominated by inorganic materials that require expensive and complex manufacturing procedures besides a huge effort on proper disposal facilities and dumps. In the described scenario, a new generation of organic and hybrid photovoltaic devices was born, whose compounds are easier to process and recycle.

1.1 Solar Cell Generations

The several types of photovoltaic solar cells for energy harvesting are usually grouped into different generations classified by the technology used in the solar cells [2].

1.1.1.1 First Generation (1G)

The first generation of photovoltaic solar cells is based on single junction devices. Multi-crystalline and single-crystal silicon solar cells are the most representative and diffused examples of the first generation technology. The 1G is mainly based on lithographic screen printing technology. Since 1G production process is common to semiconductor manufacturing, it found a huge expertise and enormous manufacturer factories to help the scaling to mass production. In 2018, single-crystal solar cells hit 26.1% efficiency that lowers to 22.3% for multi-crystalline as reported in Fig. 1.1.1. Despite in 2005 a single-crystal solar cell with concentrator proved a maximum efficiency of 27.6%, thus approaching the silicon Shockley-Queisser [3] limit of 30% efficiency, the average efficiency for a common solar panels installation is about 17%. Mainly due to silicon wafers production cost, the price per watt of 1G solar cells is still about three to four times higher than traditional energy sources such as fossil fuels and usually it does not include the recycling costs.

1.1.1.2 Second Generation (2G)

The second generation of photovoltaic technologies are still based on single junction devices; however, the aim of 2G is to maintain the same efficiency as 1G using less material. $CuIn(Ga)Se_2$ (CIGS), CdTe/CdS (CdTe) amorphous-Si (a-Si) and polycrystalline-Si (p-Si) are the key-role materials used on 2G solar cells. These materials are usually deposited as a thin film coating (1-10 μm) on low-cost substrates (glass), thus reducing the overall expense of solar panels. Despite the high 21.7% and 21% efficiencies obtained on a laboratory size CIGS and CdTe solar cells, scaling of 2G technology to plant size solar panels reduces the efficiencies to an average 16% and 10.7% [4]. This efficiency drop in large-scale 2G solar panels is attributed to poor material uniformity over large area and material issues. Besides, 2G technology found limited support for scaling to mass production because of the absence of the industrial support that so easily helped the spread of 1G technology [2]. Consecutively, 2G expansion on the market is slower compared to 1G despite the cheaper cost per watt that 2G offers.

1.1.1.3 Third Generation (3G)

The third-generation photovoltaics is distinguished by the usage of multi-junction solar cells. Using multiple band-gap materials the 3G aims to increase the devices efficiency improving the photons harvesting. Hetero-junctions allow an increase in efficiency that overcomes the 30% limit predicted for silicon based technology. The record for multi-junction monolithic cells with concentrator is 46.0% efficiency while it lowers to 38.8% without concentrator; both records were obtained with four junction devices [5]. As the graph in Fig. 1.1.1 clearly shows, the higher the junction number the higher the maximum efficiency the device can reach. However, such outstanding records were obtained using expensive processing techniques and costly III-V inorganic semiconductors. Thus, despite multi-junction solar cells based on III-V inorganic semiconductors proved it possible to overcome the Shockley-Queisser limit on silicon devices, their usage is limited to space constrained applications (e.g.: aerospace) or to power plans using expensive concentrators that maximize the energy harvesting, minimizing the required solar panel area.

3G however includes several other multi-junction solar cells, mostly devices based on relatively inexpensive semiconductors and with low-cost processing. The low cost PV in 3G are Dye-Sensitized Solar Cells (DSSCs), Polymeric Solar Cells and Perovskite Solar Cells (PSCs). Despite the outstanding short payback time and cost per watt, these PV technologies still suffer of lower lifetime expectancy and efficiency compared to inorganic solar cells. However, the potential for scalability and competitiveness make of these PV devices a promising alternative for solar energy harvesting in the next future.

Other PV technologies among 3G are quantum-dot solar cells (QDSCs) and solar cells with nanostructured additions. These technologies represent an evolution of the 3G multi-junction concept since the multi-band gap solar cell is obtained by proper tuning of the quantum-dot material used or by addition of nanoscale inorganic add-ons in the solar cell. Despite carrying very promising possibilities, these technologies have not been tested yet on large area devices and are mainly studied and developed as laboratory size solar cells.

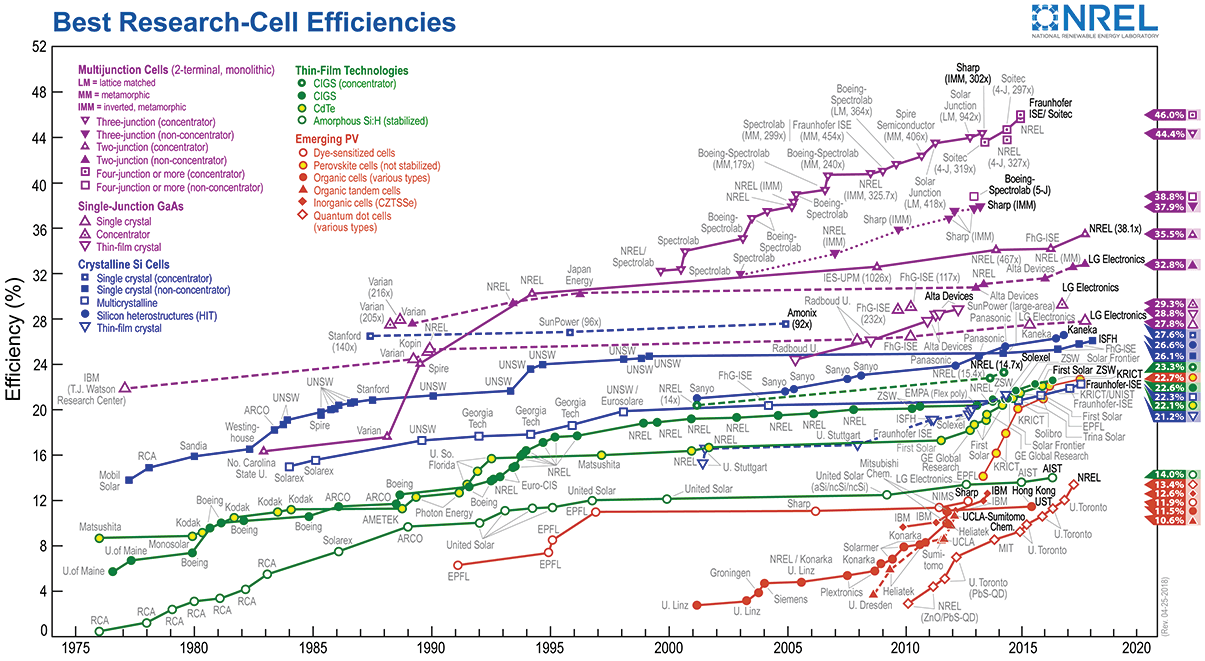

Fig. 1.1.1 NREL plot updated to 2018 showing the efficiency of different photovoltaics technologies.

1.2 Organic and Hybrid Photovoltaics

1.2.1 Genesis and attractiveness

Despite Pochettino firstly observed the photovoltaic effect on organic compounds in 1906 [6], it was only with the development of organic chemistry starting in the ’50 and with several studies on photovoltaics properties of organic compounds (from carotene to phthalocyanines-PC) that a first milestone was posed for a new type of photovoltaic based on organic semiconductors. In 1988, the first solar cell using an organic dye sensitizer was built by M. Grätzel e B. O’Regan [7].

Organic and hybrid photovoltaics are 3G because their working principle is that of a hetero-junction. Usually, these cells use a multi-layer vertical structure, with the photoactive layer sandwiched between two semi-transparent electrodes. Other layers in addition to this simple structure help maximizing the device reliability and optimizing the energy harvesting. The active layer absorbs photon energy, converting this energy into free charges. The correct usage of an electron transport layer (ETL) and a hole transport layer (HTL) help the separation and extraction of the photo-generated charges. Aligning highest occupy molecular orbital (HOMO) and lowest unoccupied molecular orbital (LUMO) with the corresponding electrodes work functions is fundamental to maximize the cells efficiency.

Among the several properties of organic and hybrid semiconductors is the low-cost and low temperature processing. Due to the organic nature and thin film applications, these semiconductors perform exceptionally well also under mechanical stress and thus it is possible to realize photovoltaics devices on flexible substrates, as shown in Fig. 1.2.1. Flexibility is a mandatory for integrating photovoltaics where traditional inorganic solutions cannot be used without affecting the visual aesthetics. Besides, flexibility supports the development of low cost typographic processing such as roll-to-roll techniques, shown in Fig. 1.2.2, increasing the production throughput and thus lowering the PV module cost per watt [8]. Furthermore, the usage of different colors is possible thanks to the almost infinite tuning possibilities given by organic and hybrid semiconductors; an example is the application in Fig. 1.2.3. Indeed, engineering the materials allows altering and modifying the optical and electrical properties of the active layer, optimizing not only reliability and efficiency but also esthetic impact [9].

All the properties and advantages of 3G organic and hybrid photovoltaics make these devices appealing both in term of costs and technology, as a promising renewable energy source.

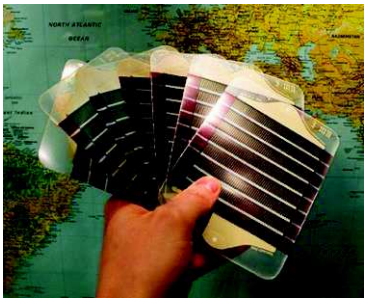

Fig. 1.2.1 Photovoltaics modules manufactured at DTU (Denmark Technical University) on PET substrate. The modules are made of 8 cells on series.

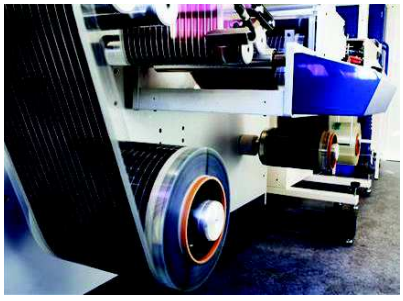

Fig. 1.2.2 LA330 Solar laminator, Roll-to-Roll solar cell printing unit installed a RISØ-DTU (National Laboratory for Sustainable Energy).

Fig. 1.2.3 Windows of the conference center EPFL (École polytechnique fédérale de Lausanne) in Switzerland with colorful embedded organic DSSC.

1.2.2 Structures and operational mechanism

Several structures and materials were developed and studied for organic and hybrid photovoltaics. The two most known structures are described in Fig. 1.2.4a and consist of two transport layers, contacted by the electrodes, sandwiching the active layer. When the anode is at the bottom of the structure, deposited directly on the substrate, the cell is in standard configuration; otherwise, the structure is inverted. Fig. 1.2.4b describes the general desired band diagram for these devices. The active layer has the function of absorbing the photons energy, creating free charges. Depending on the solar cell type, the active layer is made of different organic/hybrid compounds and can be either microporous (as in DSSCs) or compact solid (as in polymeric solar cells and PSCs) semiconductor. The ETL and HTL are specifically selected semiconductors, whose band alignment allow the transportation of a selected charge type while preventing the opposite type from reaching the electrode and recombine. Besides the electrical properties, ETL and HTL are also required optical characteristics such as transparency or UV light absorbance. Transparency at wavelengths where the active layer efficiently converts photons to charges guarantees outstanding conversion efficiencies, while preventing UV from reaching the active layer limits the high-energy photon induced degradation that is typical of organic materials [10,11].

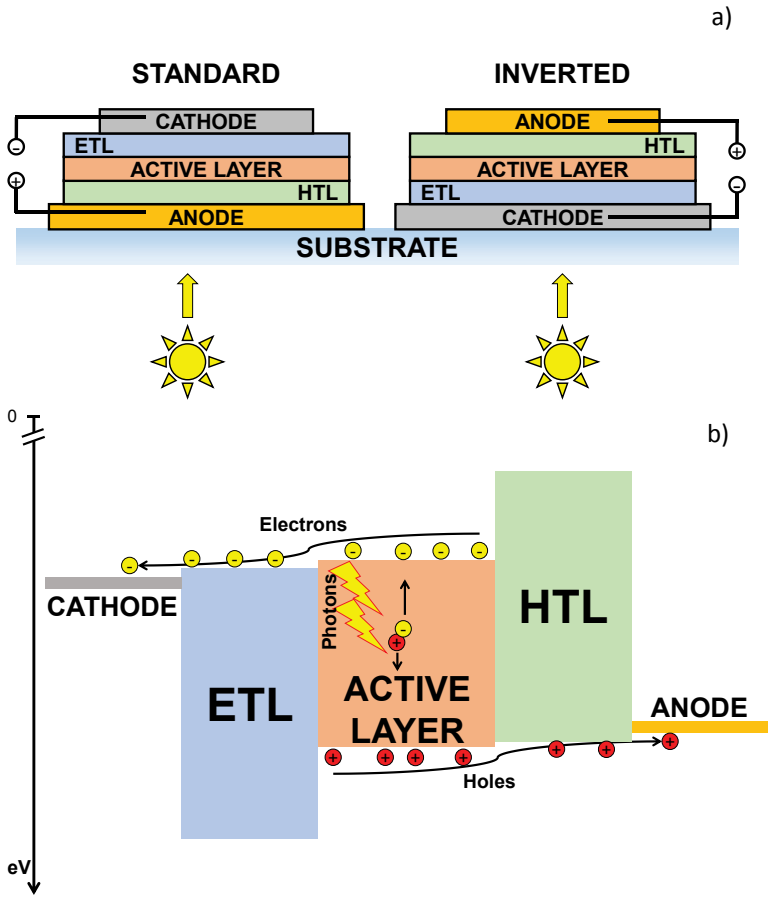

Fig. 1.2.4 a) Standard and inverted structures adopted for organic and hybrid solar cells. b) General band diagram of a hybrid/organic solar cell.

Despite the wide range of substrates, active layers, ETL and HTL possibilities, we can group organic and hybrid photovoltaics 3G solar cells in three main categories:

- Dye-sensitized solar cells;
- Polymer solar cells;
- Perovskite solar cells;

These three groups mainly differ for the type of materials used as active layer. DSSCs use a dye (organic/inorganic) and an electrolyte. The typical cell structure is shown in Fig. 1.2.5a. The dye usually permeates the surface of microporous TiO_2 that is the ETL. Upon exposure to light, once a photon reaches the dye it generates an exciton that separating creates free positive and negative charges. The positive charge moves to the HTL and then to the anode thanks to the liquid electrolyte while the negative charge is exchanged through the porous ETL with the cathode. Polymeric solar cells described in Fig. 1.2.5b make use of a thin film organic active layer, which is a blend of at least two different polymers or molecule forming an organic hetero-junction. Once the photon gets into the active layer, its absorption generates an exciton that is separated thanks to the different HOMO and LUMO energy levels of the polymers in the compound. The generated free charges then reach the right electrode thanks to the selective HTL and ETL. Finally, PSCs represent an evolution of DSSCs. Despite DSSCs traditionally make use of liquid electrolyte, at the beginning of the 21st century a new solid state dye sensitized solar cells was realized, comprehending only solid elements, thus posing the basis for the development of perovskite solar cells. In PSCs, as described in Fig. 1.2.5c, the perovskite active layer is in direct contact with the HTL and ETL. Indeed, despite a porous ETL layer was maintain as in DSSCs to maximize the charge extraction efficiency, there is no electrolyte. Due to the good holes/electrons mobility within the perovskite layer, there is no need for an ionic charge-transport electrolyte and the extraction process is more similar to the one occurring in polymeric solar cells rather than that of DSSCs. The photon exciting the hybrid active layer directly generates an electron-hole couple, similarly to standard inorganic solar cells, then the free charge is extracted thanks to the selectivity of the HTL and ETL. However, the perovskite structure is much more unstable compared to polymers and upon the application of an electric field the structure ionizes and some ions (e.g.: Pb^+, MA^+, I^-) start moving within the perovskite. These ions are responsible of several phenomena (as hysteresis and long time-transient responses) that make PSCs more similar to DSSCs rather than to polymer solar cells.

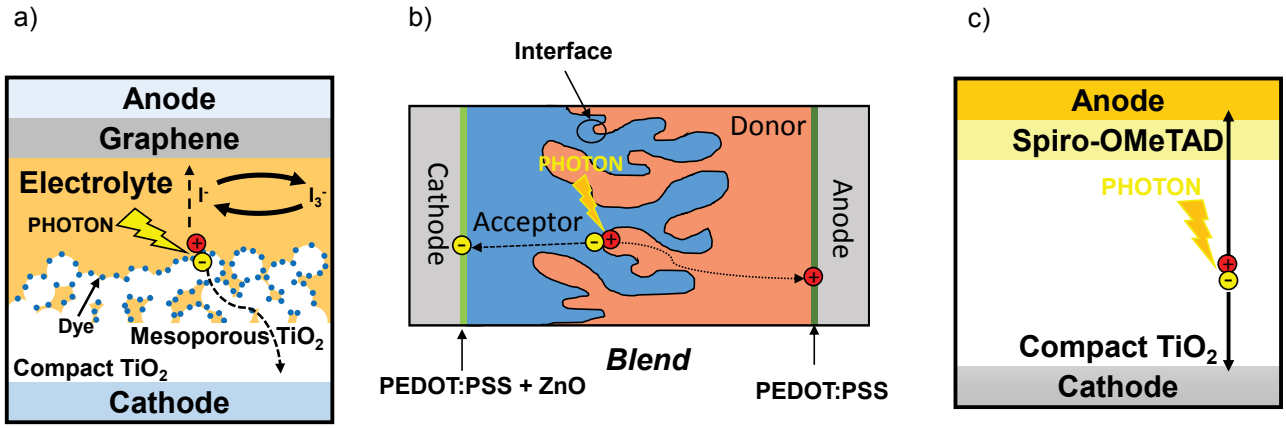

Fig. 1.2.5 Examples of a) DSSC structure, b) polymeric solar cell structure and c) PSC.

As shown in several reviews on organic photovoltaics (OPV) [12], the outstanding innovation of this technology is the usage of economic materials, easier to process and in most cases dispose of, limiting the environmental pollution. DSSCs are made of both organic and inorganic materials. TiO_2, ZnO, SnO are but a few of the oxides used as ETL (cathode), while graphene, Pt nano-particles[13] and $PtCl_2$ are used as HTL (anode). Anthocyanin pigments are the organic molecules usually adopted as dye and selected accordingly to the required optical and electrical properties. Finally, iodine based electrolytes (e.g.: I_3^-) are the most common ionic charge-transport used in DSSCs. Polymeric solar cells make use of synthetized organic molecules and polymers as active layer [14] (e.g.: PCBM, P3HT, PF, PCDTBT, PF8TBT and PF10TBT). In order to enhance the charge separation while limiting charge recombination at the contacts, oxides layers (e.g.: ZnO, MoO_3, TiO_2) are used as ETL/HTL, in combination with other organic semiconductors like PEDOT:PSS or graphene. On the other hand, perovskite solar cells active layer most common materials are $CH_3NH_3PbI_3$ and $FAPbI_3$, while PCBM, PEDOT:PSS, TiO_2, ZnO, NiMgLiO, PTTA, SnO_2, Spiro-OMeTAD are used as HTL and ETL layers. Since PSCs use PbI_2 as the active layer precursor, disposing of these solar cells containing lead iodide is more challenging compared to DSSCs and polymeric solar cells. In order to make PSCs environmental friendly, several researchers are pointing their efforts into the development of new active layers exploiting other substances (lead free) easier to recycle, such as $CH_3NH_3SnX_3$ (where X = I, Br or Cl), $Cs_2AgBiBr_6$ [15] or $CH_3NH_3SnI_{3-x}Br_x$ [16]. Despite the efficiencies reached by lead free devices are still lower than the outstanding record performance of 22.1% reached by PSCs using lead, the quick development of the technology and the huge efforts invested worldwide among the different research centers suggest that in the next future perovskite technology will become safer and economically competitive with silicon photovoltaics.

All the three groups make use of external contacts (electrodes) typically made of Au, Ag or Al for laboratory size devices, while they use conductive carbon-based compounds for large area solar cells and solar panels.

1.2.3 Weaknesses and issues

Despite the conspicuous improvements since the first proof of organic/hybrid photovoltaics capabilities and the competitive processing techniques, these technologies nowadays have not conquered yet a market comparable to standard inorganic photovoltaics. The main obstacle to the expansion of organic/hybrid photovoltaics market relies on the huge gap in terms of reliability and performances if compared to common inorganic (mostly silicon) devices.

An in deep analysis of photovoltaic performances obtained by the different technologies both organic/hybrid and inorganic is reported by Green et al. [4]. From the results of Green et al. research, it is possible to observe that silicon and inorganic (GaAs, CIGS, CdTe, InGaP/InGaAs) PV module efficiencies (ranging from 18.6% to 31.2%) are considerably higher than organic/hybrid PV modules (ranging from 8.7% to 11.6%). Indeed, despite the single cell efficiency of hybrid/organic photovoltaics reaches values as high as 22.1% for PSCs, 11.9% for DSSCs and 12.6% for polymeric solar cells [17], scaling the devices area maintain high performances is a complex task compared to inorganic PV technologies. Accelerated aging tests proved that the reliability of organic/hybrid photovoltaics is considerably lower than that of commercially available inorganic PV [11,18–23], resulting in a shorter lifetime expectancy for the former PV compared to the latter. However, the main issue behind the scaling of organic/hybrid PV technologies is the lack of industrial expertise, in contrast to the enormous amount of skills, technical knowledge and resources that silicon-based IC industries possess. Nonetheless, the recent industrial efforts [24] in the field of organic/hybrid photovoltaics proved that realizing large area PV modules while maintaining high performances is feasible. Paving the way for further research and investments into organic/hybrid photovoltaics.

Nowadays, organic/hybrid PV are primarily used as an alternative when standard rigid silicon PV cannot be installed. Flexibility, colorfulness and easier aesthetical integration of these solar cells make organic/hybrid PV a useful tool for engineers, designers and architects to combine renewable energy harvesting devices into buildings and spaces that were not exploitable before. However, the exponential growth of these innovative technologies foresight a much wider application in the next future and for this reason further research on organic/hybrid photovoltaics is necessary. In order to make these technologies economically competitive and extend their application on a large scale, improved performances in parallel to increased lifetime and reliability are mandatory.

1.3 Measurement Techniques

In order to study solar cells, several techniques are available; these measurements can be electrical, optical or a combination of both. Current-voltage characterization under standard solar simulator is the most common method to assess the cell-under-test efficiency; however, other techniques are available to determine a device (and more in general a semiconductor) physical parameters and reliability. Among the possible parameters that can be extrapolated from electro-optical characterization and modeling are charge carriers mobility and lifetime, internal generation/recombination rates, defects density and distribution, dielectric constant, breakdown electric field, absorbance spectrum, work functions levels and band gap, internal/external quantum efficiencies. On the other hand, the application of stressing factors are intended to accelerate the aging of the device in order to study what would be the device behavior during its future everyday usage. Analyzing the parameters listed above while stressing a device (e.g. applying a strong electric field/current or exposing the device to extreme environmental conditions) allows understanding the critical mechanisms compromising the device reliability and shortening its lifetime. Below is a concise description of the available characterization and stress techniques. Remarkably, among the several techniques listed, some were developed specifically to study organic/hybrid photovoltaics, since these innovative semiconductors have peculiar behaviors that could not be analyzed using standard inorganic characterization measurements.

1.3.1 Characterization

Characterization techniques can be divided in three main groups, depending on the time domain analyzed during the measurements. There are continuous, modulated and transient characterizations.

1.3.1.1 DC measurements

I-V: current-voltage scan that measures that sample steady-state current flowing through the device while applying a voltage, both in dark and under illumination. Fig. 1.3.1a shows the typical I-V curves of a solar cell. In order to guarantee the correct current sampling at each applied voltage it is necessary to wait a hold time at each step, thus letting any transient response to decay. Integrating and averaging the current samples allow increasing the signal-to-noise (SRN) ratio. The standard performance parameters such as fill factor (FF), efficiency (η), short-circuit current (I_{SC}) and open-circuit voltage (V_{OC}) are extrapolated directly from the I-V scan under illumination of a solar cell. Furthermore, using proper models, I-V measures are useful to extrapolate many other parameters both in inorganic and organic/hybrid PV such as series (R_S) and shunt (R_{SH}) resistances or photocurrent. However, while this technique is reliable on inorganic PV, it has to be handled with care when applied on some hybrid solar cells [25].

I_{SC}: short-circuit current measure is an I-V scan under illumination of a single point, the short-circuit condition (0V). The current measured by this characterization is usually estimated from the complete I-V scan in light by proper interpolation around 0 V, as shown in Fig. 1.3.1a. Sometimes however, due to the poor stability of the device under test or when the I-V scan is highly hysteretic, it is preferable to use this dedicated measure to calculate the short-circuit current using a specifically chosen hold time that allows all transient phenomena to end.

V_{OC}: open-circuit voltage characterization measures the potential difference at the electrodes of a solar cell under illumination when imposing a zero-current flowing through the device. Similar to the I_{SC}, the V_{OC} is usually extrapolated from the I-V scan in light (see Fig. 1.3.1a). However, in some cases it is preferable to dedicate a specific measure to calculate correctly the open-circuit voltage.

MPP: the maximum power point measure allows monitoring the current-voltage operating point corresponding to the device maximum output power, correspondingly V_{MPP} e I_{MPP}. While this technique is usually adopted in PV installations to maximize the power conversion efficiency by tuning the operating voltage and current of the modules according to the illumination intensity, it is also useful to analyze the efficiency of devices under real operating conditions and accelerated aging stresses. In particular, the MPP is a useful technique when it is not possible to measure reliable I-V on a solar cell (as in the case of unstable devices).

LBIC: light beam induced current is a powerful tool to determine any defective points on the solar cell area. This measure, as described in Fig. 1.3.1b [26], consists on scanning with a laser beam (resolution < 100µm) the active area of the device under test (both single solar cell and module) while measuring the device I_{SC}. By creating a 2D map of the measured current, it is possible to determine damaged parts in the active area or defective regions due to issues in the manufacturing process.

EQE, IQE: external and internal quantum efficiency techniques measure the photo-generated current of a device under monochromatic light and quantify how many of the incoming photons (EQE) or absorbed photons (IQE) are converted into extracted electrons and holes at the electrodes.

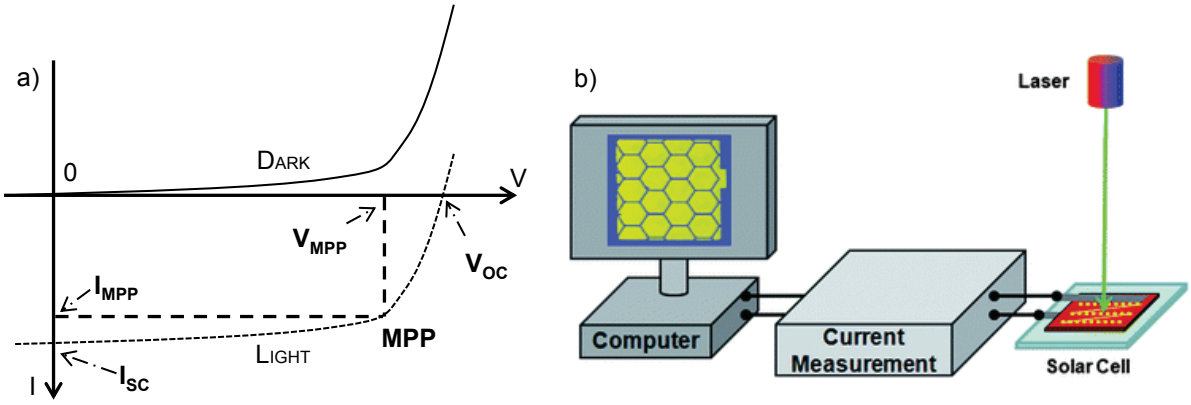

Fig. 1.3.1 Standard current-voltage curves in dark and light of a solar cell a). Representation of LBIC setup as described in [26].

1.3.1.2 AC measurements

IS: impedance spectroscopy is a modulation measurement that characterizes the electrical frequency response of a device under test. By applying a small sinusoidal voltage/current signal and measuring the consequent current/voltage, it is possible to obtain the impedance (module and phase) of the device at a specific frequency. Repeating the measurement in the desired range of frequencies and estimating the real and imaginary parts from the module and phase gives the Nyquist plot of the device impedance, as the example shown in Fig. 1.3.2a. The IS can be measured at different steady-state conditions and illumination levels, with a frequency range going from μHz to MHz depending on the device typology. Impedance spectroscopy in combination with proper impedance modeling are powerful tools to characterize materials and interfaces of devices based on both organic and inorganic semiconductors. Since IS measurements are highly sensitive to noise and erroneous artifices, care must be put in the preparation of IS setup.

C-V: capacitance-voltage measurement is an IS measurement at a single frequency but variable voltage. The model used to fit the resulting impedance is composed of a resistor in parallel with a capacitor and since this model comprehends only two variables (R and C), using real and imaginary parts of the impedance allows estimation of both resistance and capacitance behaviors within the analyzed voltage range. The C-V measurement is traditionally associated to characterization of spatial charge regions (SCR) in inorganic semiconductors. Plotting the $1/C^2$ over voltage graph (see Fig. 1.3.2b) and interpolating the resulting curve gives a useful estimation of parameters such as the material doping type and distribution or the built-in voltage. On organic/hybrid devices however, C-V measurements can be misleading due to the complexity of the samples structure, since the contribution to measured impedance does not come only from a single interface or SCR. However, C-V technique gives useful results when there is an element dominating the impedance of the device, since it describes that element behavior within the analyzed voltage range without requiring a complete IS characterization that is time consuming and that may degrade the device under test.

IMPS, IMVS: intensity modulated photocurrent spectroscopy and intensity modulated photo-voltage spectroscopy are modulation techniques similar to IS but using a frequency modulated light as stimulating source and measuring the frequency modulated photocurrent or photo-voltage at the selected bias voltage or current. The resulting frequency response shows useful data regarding the materials and interfaces role in the charge transport, recombination, extraction and accumulation.

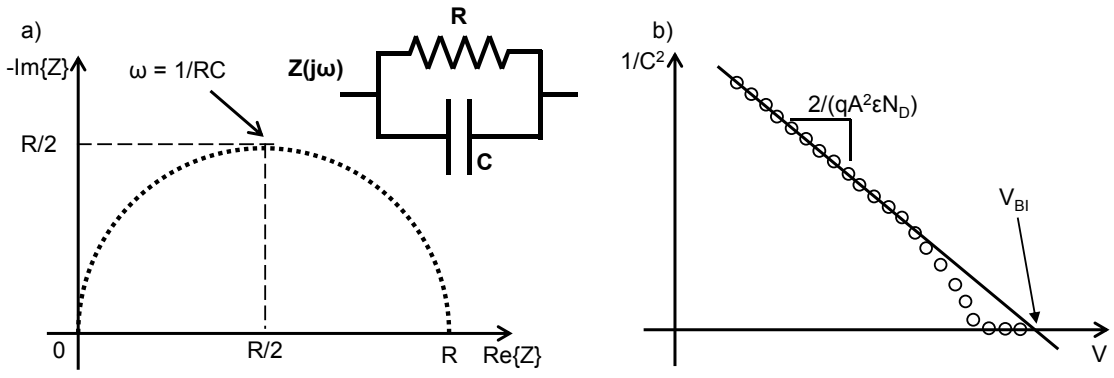

Fig. 1.3.2 Example of IS a) as measured on the resulting impedance from the parallel of a resistor and a capacitor. b) standard $1/C^2$ over voltage plot for a silicon diode.

1.3.1.3 Transient measurements

Suns-V_{OC}: is an electro-optical technique that measures the voltage transients of a solar cell under pulsed light stimulation at different power intensity. Imposing zero-current condition at the electrodes and measuring the V_{OC} transient under controlled light power intensity, it is possible to measure the amount of photo-generated charge present within the device and the equivalent current related to internal recombination at the various intensities [27]. Post-processing the measurement results, the suns-V_{OC} allows estimating a pseudo-current-voltage curve that is not affected by the contribution of the contacts resistance and thus by R_S, as shown in Fig. 1.3.3a. Fast and synchronized light sources and measurement units are required in order to implement a precise Suns-V_{OC} measurement setup, since most of both organic and inorganic devices have very fast photo-voltage transient response.

DLTS: deep level transient spectroscopy technique is a set of measurements at different temperatures in dark that sample the transient current (or capacitance) during a voltage pulse. This technique is commonly applied to inorganic devices to estimate the trap release timings thus extrapolating the defects activation energy, but it can be extended to organic/hybrid devices as well.

OCVD: open circuit voltage decay is a measurement developed specifically to study the first DSSCs. This technique samples the V_{OC} decay of a solar cell after that the light source illuminating the device is switched off. OCVD results elaboration and modeling allow extrapolation of charge carrier lifetime and recombination rates. Fig. 1.3.3b shows as an example the resulting OCVD of perovskite solar cell.

ABVD: applied bias voltage decay consists in the measure of the transient voltage after that the bias previously applied to the device is switched off. Applying bias forces free carriers within the device and measuring the open circuit voltage decay after that the bias is removed allows estimation of recombination rates by means of proper modeling.

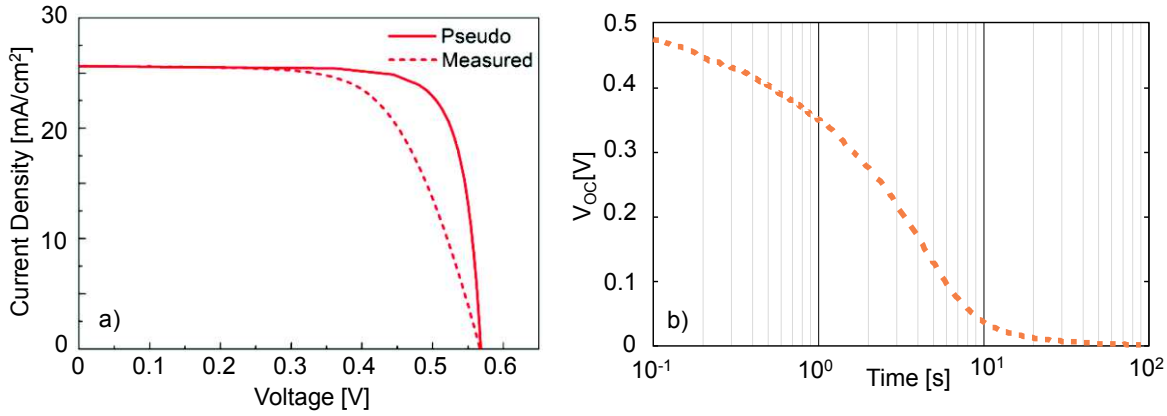

Fig. 1.3.3 Comparison of Suns-V_{OC} and I-V measurements as reported in [28] *a). OCVD example b) of a perovskite solar cell.*

1.3.2 Stress

The aim of the stresses is to accelerate the aging of the device under stress, giving an estimation of what would be the normal lifetime in everyday usage. Furthermore, by applying the above characterization techniques during the stresses, it is possible to estimate the failure mechanisms giving the manufacturer crucial information. Therefore, stressing devices is a fundamental step in the development of reliable and long lifetime PV. Since the stresses point to simulate the effect of everyday usage but on a shorter time scale, there exist several types of stresses on semiconductors. Depending on the key stressing element, it is possible to divide the stresses into few groups: thermal, electrical, light induced and environmental stresses. Furthermore, among the possible key elements discriminating a stress from another is the intensity regulation of the stressing element and the time scale used during the stress. A stress is commonly defined as "ramped stress" when the intensity increases at each step during the stress, while it is defined as "constant stress" when the intensity is the same during all the time of stress. Similarly, stresses can be classified by the timing used during the stress, which can be logarithmic or linear. In the below sections there is a summary of the procedures most commonly used to evaluate a device reliability and lifetime expectancy. By using more than a stress type at the same time, it is possible to study the combined effects of the stresses.

1.3.2.1 Thermal stress

Using specifically designed temperature control systems, the device undergoes storage at controlled temperature, usually high. While this procedure is called annealing when it is short and it helps improving the device performances, prolonged exposure to high temperatures usually leads to a degradation of the semiconductor. In organic/hybrid solar cells, since the building process runs at low temperatures, thermal stress usually plays the role of both annealing and degrading factor. However, at relatively high and low temperatures (compared to operating conditions) thermal stress is particularly detrimental on organic/hybrid semiconductors since it can change both the morphology and the structure of the solar cell materials, while this is less effective with inorganic semiconductors that are processed at hundreds Celsius degrees.

1.3.2.2 Electrical stress

The most important electrical stresses are forward current, reverse voltage, pulsed current/voltage and ESD stresses. These stresses aim to simulate the electrical conditions a solar cell undergoes once connected into a module/panel, in particular on organic and hybrid solar cells, since it is usually not possible to use bypass diodes. Forward current is a consequence of partially shading a cell connected in parallel to others into a solar panel (**Errore. L'origine riferimento on è stata trovata.**a), since the other working devices will see the shaded cell as a load. Reverse voltage occurs when a single cell in a series is shaded (**Errore. L'origine riferimento non è stata trovata.**b); since the shaded cell is not photo-enerating, the current is interrupted and the open-circuit voltage of the remaining cells drops on the shaded one. Pulsed current/voltage might occur when there is a hot-plug connection of the solar cell to the control system, since the solar panel is always on when exposed to the light. Finally, electro-static discharge stress simulates the human body discharges typically occurring during installation and handling of solar panels and modules.

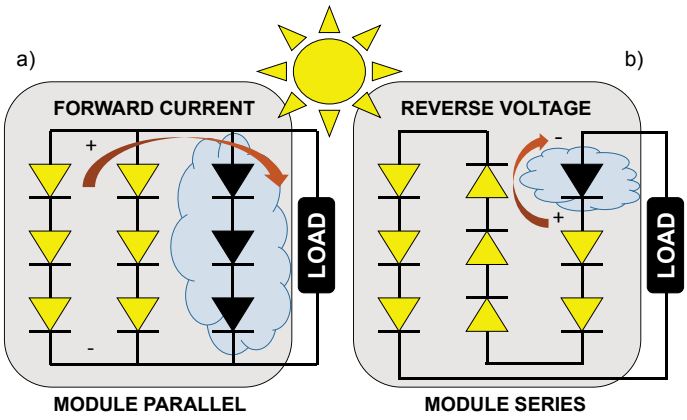

Fig. 1.3.4 . Effects of partial shading on two module configurations: module with parallel rows of cells a) and module with only series of cells b).

1.3.2.3 Light induced stress

Using a solar panel implicitly means that the solar cells will undergo extensive exposure to all the components of the solar spectrum. The most damaging component affecting a solar cell is usually ultraviolet light (UV) due to high-energy photons. UV light is particularly damaging for organic/hybrid solar cells and UV barriers are usually installed during solar panel manufacturing in order to extend the modules lifetime and reliability. By using high intensity UV light and characterizing the device under stress, it is possible to study the mechanisms behind the induced degradation and thus realize suitable countermeasures. Other light induced stresses include high suns exposure, which simulate the usage of concentrators, and modules partial shading usually causing the electrical stresses previously described.

1.3.2.4 Environmental stress

Solar panels are a powerful renewable energy harvesting technology adopted not only in energy plants as an alternative to fossil fuel combustion, but also integrated in home architecture and impact-zero building roofs since it is easily portable and its installation does not require particularly complex facilities. Being exploited worldwide as energy sources, solar panels undergo all types of weather distress and environmental conditions. In particular, organic/hybrid PV are highly susceptible to moisture and oxygen, since these factors affect the materials composition and the internal bonding. Stressing the devices in high humidity or oxygen it is possible to determine the weaknesses of the encapsulation and sealing techniques used to reduce the effects of environmental stresses.

1.3.2.5 ISOS stress

Stresses on inorganic semiconductors are quite standardized and comparable each to other, due to the limited number of inorganic semiconductors used in electronics. On the other hand, stresses on organic and hybrid semiconductors test a much wider spectrum of devices, differing in both structure and materials. In order to give a standardized procedure to stress organic and hybrid photovoltaics in 2011 a consensus on the stability testing protocol was born at the International Summit on OPV Stability (ISOS) [29]. These stressing procedures are the ISOS tests and each test comprehends a combination of stressing factors that simulate the effects of everyday usage in different environmental conditions, light exposures and temperatures, without considering the effects of electrical stressing factors. The standard includes six basic tests, six intermediate tests and three advanced tests, probing the solar cell reliability both outdoor and indoor, under illumination and in dark or at controlled environmental conditions.

2 Organic Solar Cells

Organic solar cells belong to Organic Photovoltaic (OPV) technology. The organic composite used as active layer in these solar cells form an organic hetero-junction exploiting the optoelectronic properties of two or more materials to maximize the cells performances. Fig. 2.0.1 summarizes a few of the most common donor and acceptor polymers used in OPV, as reported in [30]. Therefore, the EQE spectrum of organic solar cells are usually the combination of two or more absorption peaks each centered on a specific material band-gap. As an example, Fig. 2.0.2 shows the EQE of a P3HT:PCBM organic solar cell where it is possible to distinguish the two contributions corresponding to each organic material composing the blend in the solar cell active layer.

Organic solar cells have attracted the attention of many research groups as a low-cost and eco-sustainable alternative to conventional solar cells in some applications [8,31–36]. The device efficiency and the fabrication processing speed of polymer solar cells were significantly improved during the last few years. However, lifetime and reliability are still the bottleneck to the spread of this technology. Indeed, during the operational life of a photovoltaic module, several factors may concurrently contribute in the loss of the cell performances and particularly affect organic photovoltaics. For example, light exposure, high temperature, non-optimal electrical operative conditions and electrostatic discharge (ESD) are just a few of the possible reasons that lead to the cell degradation during its operating conditions. Modeling and analyzing OPV undergoing aging stresses allow the identification of the mechanisms behind the degradation, distinguishing which material and/or mechanism are the main culprits for the lowered performances.

In order to extract the performance parameters (efficiency, fill factor, short circuit current and open circuit voltage) of samples under accelerated stress, the most common way is to carry out periodic current-voltage (I-V) measurements [23,29,37,38]. However, even though these common figures of merit are immediate indicators of the cell performance, they cannot give a comprehensive picture of the several physical parameters, which are crucial to improve the energy conversion efficiency. A more advanced analysis is therefore needed in order to have better understanding of the complex behavior of such parameters. The accurate extrapolation and analysis of photocurrent [39–41] and the study of the impedance spectroscopy [42,43] – for example – represent further investigation tools in organic heterojunction solar cells that can reveal the behavior of these important physical parameters such as generation rate, polaron charge transfer states separation and recombination rate, built-in potential and carrier lifetime.

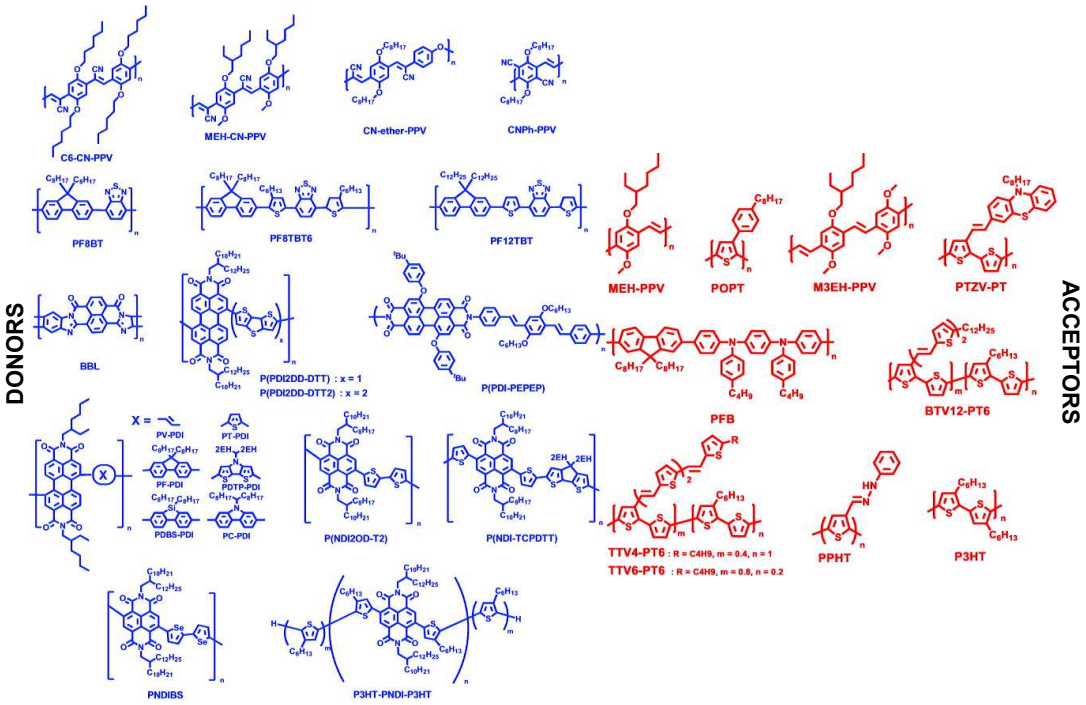

Fig. 2.0.1 Summary of the most commonly used donors and acceptors polymers as reported in [30].

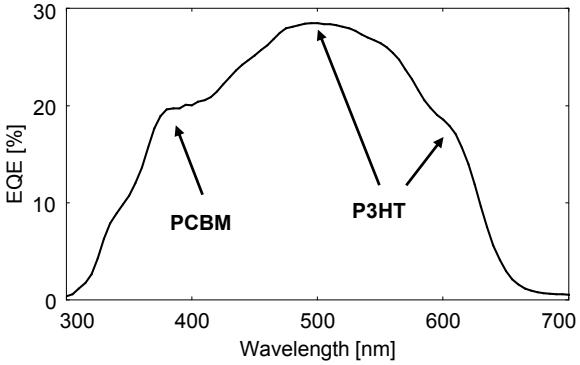

Fig. 2.0.2 External quantum efficiency of a bulk heterojunction organic solar cell based on P3HT:PCBM blend. The EQE peaks correspond to the maximum absorption of PCBM and P3HT.

2.1 Characterization and modeling of organic P3HT:PCBM solar cells as a function of bias and illumination

Section 2.1 is an extracted of the corresponding published paper Ref. J9

2.1.1 Introduction

In order to describe the physical phenomena behind photo-generation on solid organic semiconductors, several works suggested both DC and AC models [37,43–46]. The simplest models proposed in literature link the phenomena related to the physics of organic solar cells (e.g., generation, recombination and transport) to linear equivalent components (resistors and capacitance). However, those first-order models rarely fit to experimental data with an acceptable degree of precision. In addition, the majority of the works in literature describe the polymeric solar cell impedances only at one selected bias point or illumination level. This may be a severe limitation both for the correct interpretation of the impedance data and the accurate description of the role of semiconductor/semiconductor and semiconductor/contact interfaces.

To achieve a better fit of experimental data, more sophisticated models introduce one or more constant-phase-element (CPE), which is an easy mathematical artifice for justifying the dispersion in frequency of many phenomena especially in presence of irregular and porous interfaces. Although this strongly improves the quality of the fit of experimental data, it could bring some confusion on the correct association between model element and the corresponding physical phenomena [47]. In particular, some confusion may come from the correct interpretation of the value of the exponent of the CPE.

In order to overcome many of these limits, in this section we analyzed the dependence of the cell impedance on both bias and illumination level, and we run a complete AC and DC characterization of P3HT:PCBM solar cell. We proposed a more comprehensive model based only on distributed-impedance contributions, avoiding the use of CPE. Finally, we validated the model in a wide range of illumination level and operating bias conditions.

2.1.2 Methods

We considered organic solar cells with a P3HT:PCBM active layer, ZnO blocking layer and PEDOT:PSS as organic conductor [48–51]. The active layer thickness is L=315nm and the active area is 1cm^2. The samples are produced by the solar energy group at the Technical University of Denmark. We carried out the characterization of the samples by using a Solartron SI1260 Impedance Analyzer and an Agilent E5263A Parameter analyzer. We illuminated the cells by using a white LED because the measurement noise floor generated by white LED is much lower, compared to a xenon solar simulator. Besides, the white LED optical power is easily controllable, since it is almost linearly dependent to the bias current.

However, the spectra of the white LEDs differ from the one of the solar simulator, as well as Si cell absorption is different compared to an organic solar cell. We calibrated the LED output power by mean of a reference solar cell and by considering the different shape of the illumination spectrum. We verified that the short circuit current measured on an organic solar cell with both solar simulator and white LED are the same after calibration and correction.

We developed a custom sample holder, to reduce parasitic effects, such as series resistance and inductance. We also kept the overall cable length smaller than 40 cm, because excessive cable length might induce an unacceptable signal delay, with a consequent error on the measured impedance phase. After short-circuit and open circuit calibration, we achieved a reliable impedance measurement up to 8MHz.

We characterized three groups of solar cells:

1) Fresh cells fabricated to reach the optimal performance.

2) PEDOT degraded cells, where PEDOT:PSS used as hole transport layer at the anode contact was exposed to a temperature of 80°C with high moisture and in presence of air for 15 minutes before completing the cell manufacturing.

3) ZnO degraded cells, where the Flextrode [49] was exposed to UV radiation for 1h during building process before the blend deposition and cells encapsulation.

In the following, we will show the curves of three representative cells taken from group 1, 2, and 3. Tab. 2.1-A lists the three groups and the type of degradation.

Group#	Status	Degradation performed
1	Fresh	None
2	Degraded	PEDOT has been exposed for 15 minutes to a temperature of 80°C with high moisture and in presence of air
3	Degraded	"Flextrode" exposed to UV radiation for 1 hour during building process

Tab. 2.1-A Summary of some of the cells used. First column is the cell number. Second column is the cell status (i.e., fresh or degraded). Third Column is the type of degradation the cell underwent during building process.

We summarized the experimental procedure in Fig. 2.1.1. The bias voltages considered are -1.5V to 0.5V, with 0.1V step and 10mV ac signal amplitude, while the illumination levels are 0 Sun to 2 Sun, with 0.2 Sun step.

A complete characterization requires 8 hours. For this reason, before and immediately after the complete characterization, we did a quick characterization including one I-V and one IS in dark and under illumination, to assess any measurement-induced degradation. We verified that any change induced by the measurements is smaller than 5% in the worst case, i.e., much smaller than the variation range of the extracted parameters.

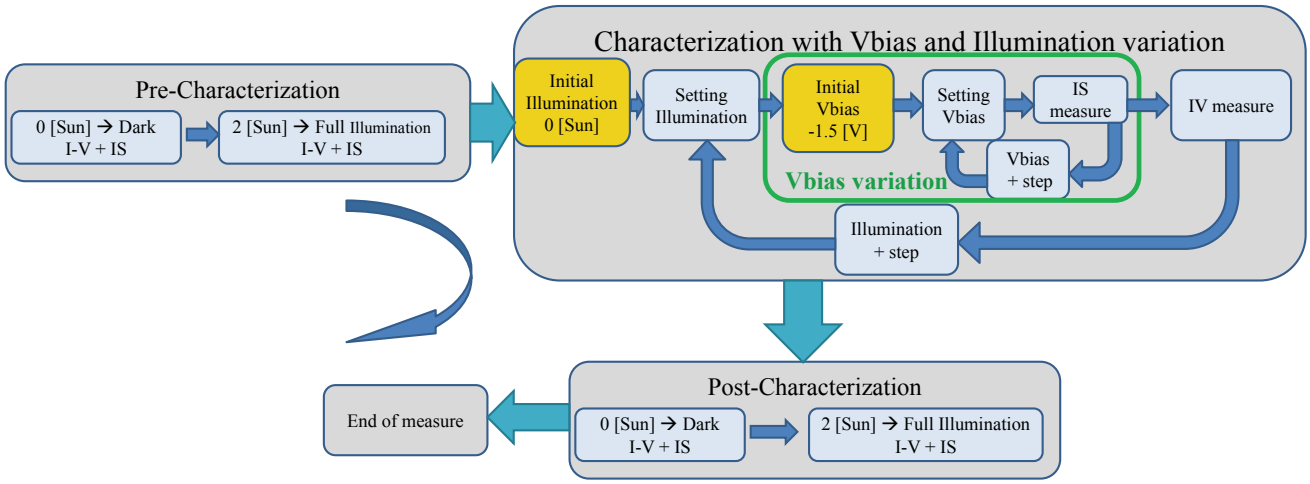

Fig. 2.1.1 Characterization procedure applied for measuring cells; the characterization could take a long time to complete. Cells performances are under control by means of pre, post and on measurements characterization.

2.1.3 Results

Fig. 2.1.2 represents the most important figures of merit of some of the characterized cells as a function of illumination levels. Fresh cells (group 1) and PEDOT:PSS degraded cells (group 2) feature a very similar behavior, showing small variation each-to-other (within the 10%). On the contrary, ZnO-degraded cells (group 3) exhibit a different behavior, indicating that UV exposure significantly changes the short circuit current, the open circuit voltage and the maximum output power. In particular, the short circuit current and the maximum power decreased to 50% and 25% of their initial value, respectively.

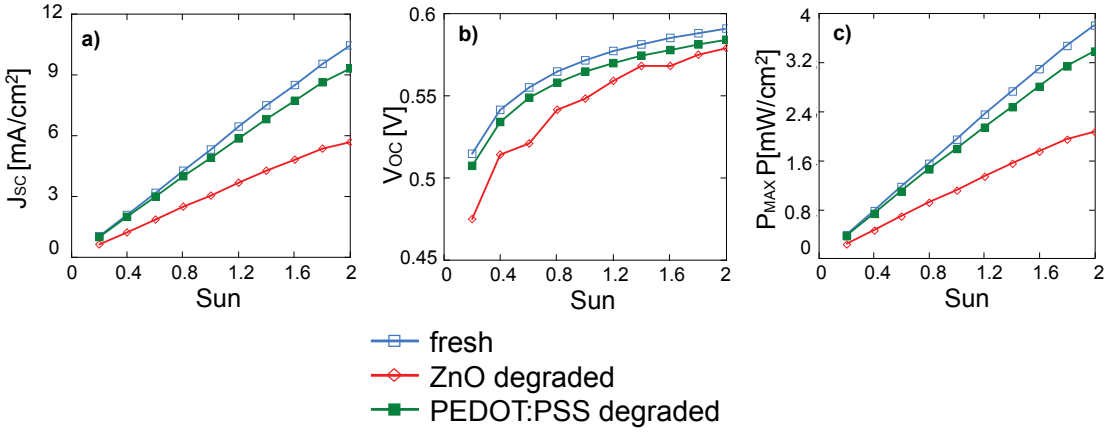

Fig. 2.1.2 Evolution of a) the short circuit current density (J_{SC}), b) open circuit voltage (V_{OC}) and c) maximum power (P_{Max}) under different illumination levels.

Fig. 2.1.3 shows the I-V curves taken at different illumination levels on three representative cells of the groups listed in Tab. 2.1-A. The main differences between fresh and group 3 degraded cells are the S-shape appearing around V_{OC} (Fig. 2.1.3b) and the short circuit current reduction. We relate the S-shape appearing in the proximity of V_{OC} to a degradation of the photo-generated current due to UV exposure [52–54]. It is possible to associate the decrease in performances of cells group 3, with the increased resistance due to ZnO degradation by means of UV light exposure during cells building (which will be confirmed by IS-analysis and modelling presented in the following). On the contrary, the degradation induced by simply exposing PEDOT:PSS to high moisture and temperature during building process (group 2), only slightly reduces the short circuit current (see Fig. 2.1.2c and Fig. 2.1.3c). For this reason, in the following we refer to fresh and degraded cells indicating group 1 and group 3 cells respectively.

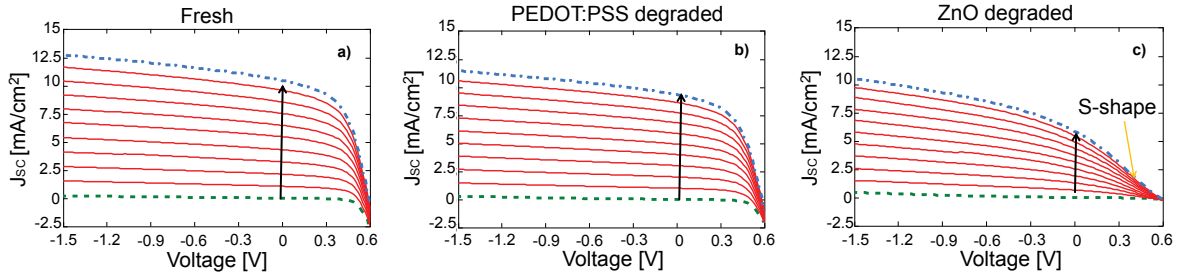

Fig. 2.1.3 J-V on three cells: a) fresh (from group 1); b) PEDOT:PSS degraded cells (group 2); c) ZnO degraded cell (group 3).

2.1.4 Discussions

Fig. 2.1.4 presents the proposed impedance model. Because the active layer might be intentionally or unintentionally unintentionally doped, we divided the active layer in two parts: a carrier depleted region (SCR, Space Charge Region) and a quasi-neutral region (QNR).

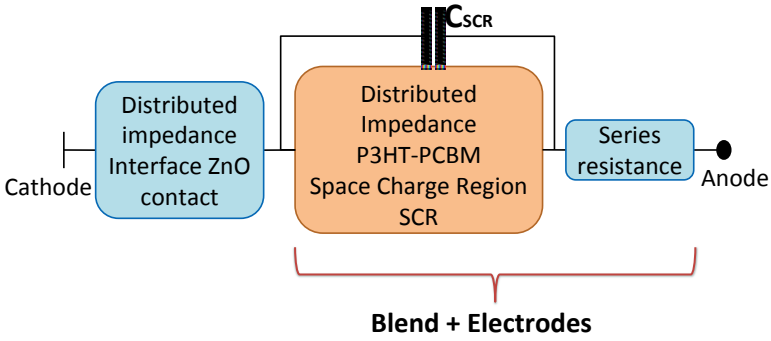

Fig. 2.1.4 Total impedance model representation

In Fig. 2.1.4, the SCR is represented by the distributed impedance:

$$Z_{AL}(j\omega) = \sqrt{\frac{R_{RG}}{R_T}\frac{1}{(1+j\omega C_\mu R_{RG})}}R_T \coth\left(\sqrt{\frac{R_T(1+j\omega C_\mu R_{RG})}{R_{RG}}}\right)$$

where:

- R_T is the transport resistance of the photo-generated carriers across the SCR.
- R_{RG} accounts for all charge transfer between acceptor and donor complexes. If cell is measured in dark, it accounts for the polaron recombination at the acceptor/donor interface. If cell is measured under illumination, it also includes the contribution of the photocurrent, which is voltage-dependent[55,56].
- C_μ is the electrochemical capacitance associated to the charge separation at the acceptor/donor interface within the blend.

The distributed impedance, shown in Fig. 2.1.5, is the same used in several work to describe the interfaces between porous materials [47,57]. In addition, a depletion capacitance (C_{SCR}) in parallel to the distributed impedance accounts for the junction capacitance.

We modelled the ZnO/active-layer interface with another distributed impedance:

$$Z_{ZnO}(j\omega) = \sqrt{\frac{R_P}{R_{TAL}}\frac{1}{(1+j\omega C_P R_P)}}R_{TAL}\coth\left(\sqrt{\frac{R_{TAL}(1+j\omega C_P R_P)}{R_P}}\right).$$

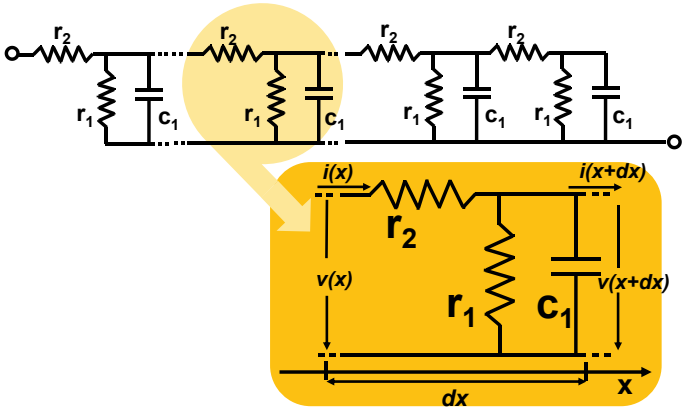

Fig. 2.1.5 Distributed impedance model used to simulate dispersion due to porosity of the material or inter-digitation.

Where:

- R_{TAL} is the transport resistance across the active layer blend.
- R_P is the contact resistance of the active layer/ZnO interface.
- C_P is the capacitance associated to the active layer/ZnO contact.

Finally the overall series resistance R_S includes the contributions of the blend QNR and contacts.

In our model, we assume it is possible to relate ZnO/organic semiconductor and organic semiconductor/organic semiconductor interfaces to distributed impedance like the one described in Fig. 2.1.5. This assumption is based on some well-known morphological and chemical observation on P3HT:PCBM and ZnO found in literature[58–60]. Indeed, distributed impedance well describes the inter-diffusions of polymers within the blend and the interaction of the porous ZnO with the active layer. Furthermore, we underline the use of a distributed impedance with a single side transport resistance in both interfaces. Indeed, the transport resistance in SCR impedance accounts for the electron transport through PCBM polymer, since the mobility of PCBM is generally much lower than the mobility in P3HT[61,62] and thus it justifies the neglecting of the transport resistance of P3HT. At ZnO/organic semiconductor interface we consider a single transport resistance related to the blend since polymer mobility (both electrons and holes) is orders of magnitude lower than electrons mobility in ZnO [63–65].

2.1.4.1 Model discussion and validation

We fitted IS at different bias and illumination levels by using our model. Fig. 2.1.6, Fig. 2.1.7 and Fig. 2.1.8 show some comparisons between model and experimental data obtained on fresh cells and degraded ones. The proposed model well fits data and allows to identify the behavior of each interface as a function of bias and light intensity. In addition, we plot in each figure the separate contribution of each impedance element in order to emphasize the effect of interfaces. Fig. 2.1.9 summarizes the model parameters as a function of bias and illumination level for a fresh cell. We do not show ZnO impedance parameters because they are almost constant with bias and illumination; Tab. 2.1-B lists the average value of ZnO parameters.

As expected the width of SCR saturates for high reverse bias, approaching a value around 170nm in dark (0 sun) calculated as:

$$L = \frac{\varepsilon_r \varepsilon_0}{C_{SCR}}$$

with $\varepsilon_r \approx 3.5$ [66,67]. Under illumination, excitons are photogenerated in P3HT and PCBM. Most of them are separated, generating free polarons that are collected by P3HT (positive polarons) and PCBM (negative polarons), leading to an increase of carriers concentration within the blend, and in turn to a reduction of the depletion width. At 1-sun illumination, the SCR width saturates around 130nm, while at 2-sun illumination it saturates around 100nm.

	R_{TAL} [Ω cm^2]	R_P [Ω cm^2]	C_P [nF cm^{-2}]
Group 1	17.05	2.8	117
Group 3	15	60	250

Tab. 2.1-B ZnO impedance parameters extracted from IS fitting. Parameters are almost constant with both bias and illumination variations. We show the mean value obtained in several fits.

From the Schottky-Mott plot of Fig. 2.1.10a that represents $1/C_{SCR}^2$ as a function of the applied bias, we notice a decrease of the intercept with the voltage axis for increasing illumination level and a decrease in slope. In the hypothesis that we could apply the Schottky-Mott analysis and supposing that the ZnO side (n doped) is much more doped than the blend, we estimate that the hole concentration in P3HT should increase from $p=2.5\cdot10^{16}$ cm^{-3} in dark to $p=7.5\cdot10^{16}$ cm^{-3} at 2-sun illumination. In principle, such increase in hole concentration should come from photogeneration, but this is strongly in disagreement with the number of extracted carrier. Furthermore, calling V_{SM} the intercept with voltage axis [68] we obtain V_{SM}=0.305V at 0-sun illumination, V_{SM}=-0.04V at 1-sun illumination and V_{SM}=-0.324V at 2-sun illumination. We cannot consider V_{SM} to be the built-in potential upper limit; indeed, V_{SM} is far below expected bandgap of the blend, which is around 0.7V [68], and reaches negative values when measured under illumination. Following these considerations, we believe that we cannot apply this analysis to calculate the p carriers concentration in light or built-in voltage both in light and in dark, which is in accordance with other works published by several research groups [68–71].

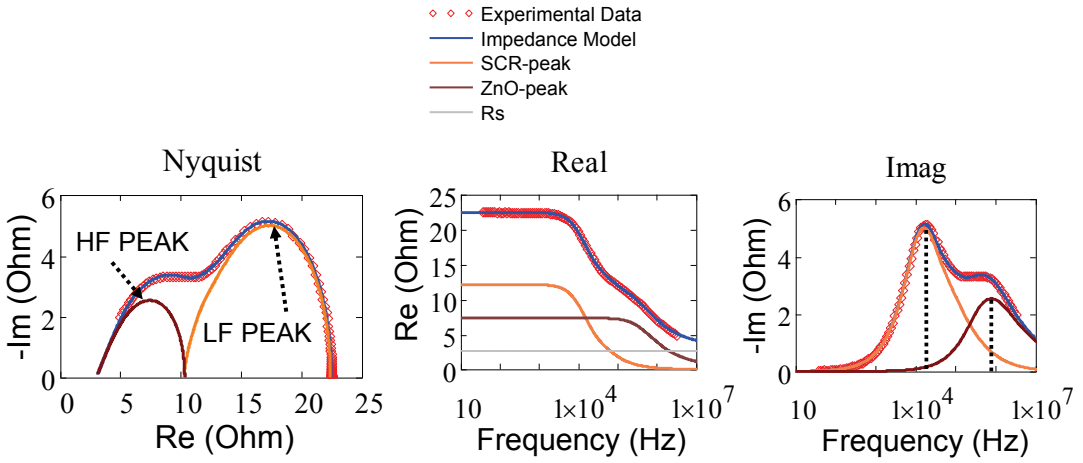

Fig. 2.1.6 Fitting results on IS of group 1 cell. Experimental data measured at 0.5 V forward bias with 1 Sun illumination.

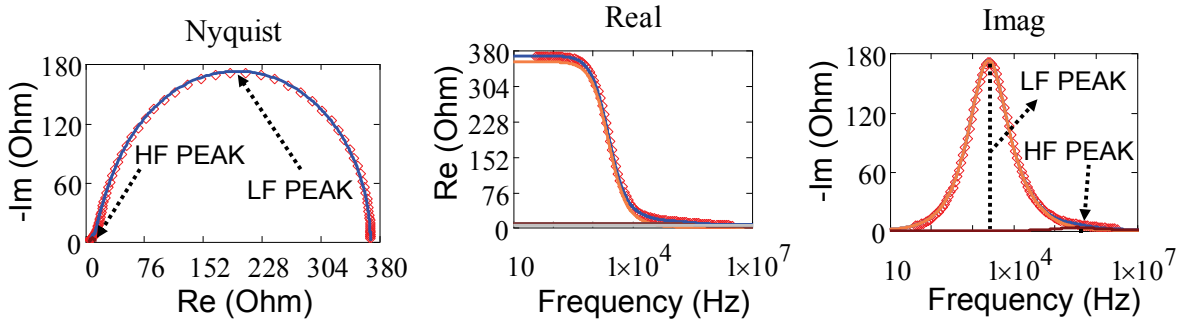

Fig. 2.1.7 Fitting results on IS of group 1 cell. Experimental data measured at 0 V forward bias with 1 Sun illumination.

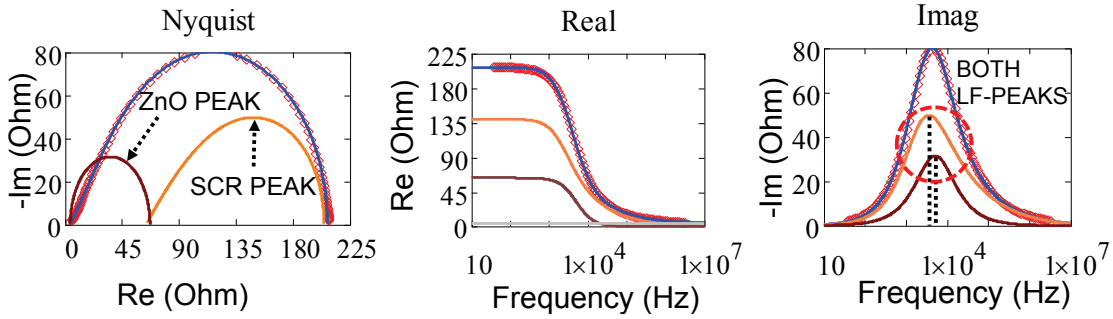

Fig. 2.1.8 Fitting results on IS of group 3 cell. Experimental data measured at 0 V forward bias with 1 Sun illumination.

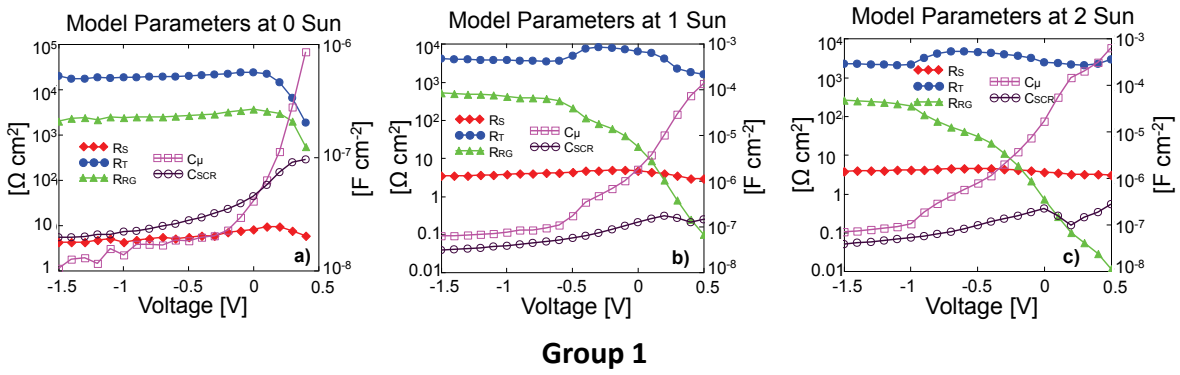

Group 1

Fig. 2.1.9 Parameters extrapolated at several illumination levels (0, 1, 2 Sun) and at varying bias voltage from a cell of group 1. a) are the parameters calculated at 0 Sun, b) at 1 Sun and c) at 2 Sun.

Increasing the illumination level leads to a reduction of resistances R_{RG} and R_T as expected, because they are both carrier-concentration dependent. Instead, the series resistance R_S keeps almost constant with both varying bias and illumination level. In our model the series resistance accounts for both the QNR and contact resistance: being R_S constant, points out that no significant changes of QNR or contacts resistance happen.

On the other hand, the electrochemical capacitance C_μ increases with increasing illumination level, as expected because it is dependent on the amount of photogenerated charges.

The same analysis repeated on degraded cells is shown in Fig. 2.1.10b and Fig. 2.1.11. In ZnO degraded cells blend, we observe a behavior similar to fresh cells, although parameters behavior is noisier. By plotting and fitting $1/C_{SCR}^2$ and applying Schottky-Mott analysis, we obtained a value of carriers concentration from $p=4.7\cdot10^{16}$ cm^{-3} in dark to $p=1.5\cdot10^{17}$ cm^{-3} at 2-sun illumination, values close to what was observed in fresh devices. The resulting V_{SM} at different illuminations is V_{SM}=0.5V in dark, V_{SM}=-0.219V at 1-sun illumination and V_{SM}=-0.45V at 2-sun illumination.

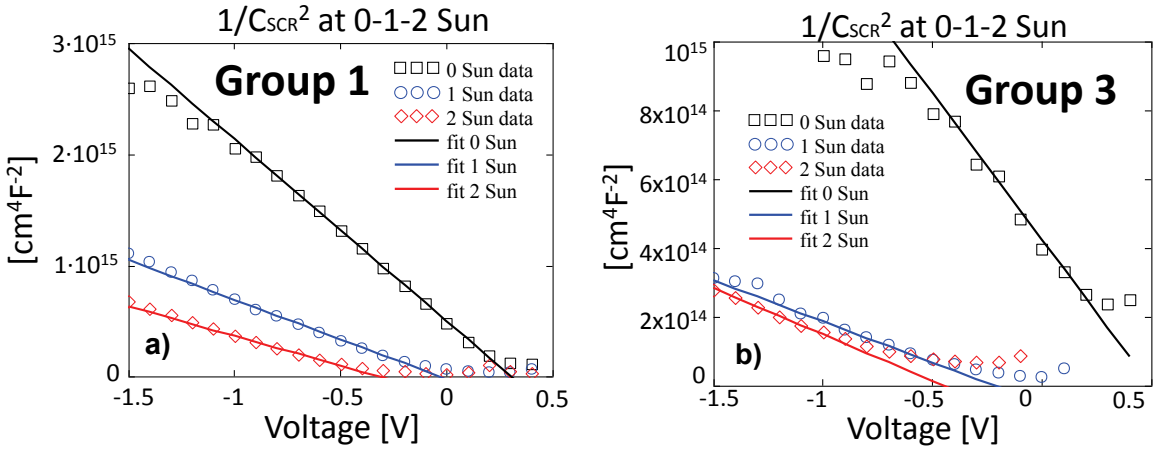

Fig. 2.1.10 $1/C^2$ plot used to apply Schottky-Mott analysis. Symbols used to represent data derived from fitting procedure on experimental data, while continuous lines are used to describe the fit apply to calculate slope and intercept of $1/C^2$ curves. a) represents the data obtained from a cell of group 1, b) represents the data from a cell of group 3.

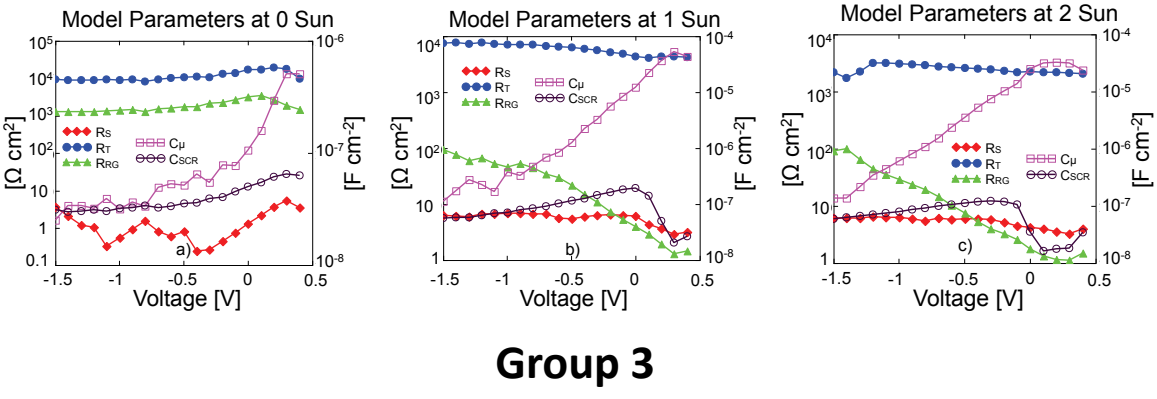

Fig. 2.1.11 Parameters extrapolated at several illumination levels (0, 1, 2 Sun) and at varying bias voltage from a cell of group 3. a) are the parameters calculated at 0 Sun, b) at 1 Sun and c) at 2 Sun.

Fig. 2.1.12 and Tab. 2.1-C show some important physical parameters extracted from SCR [44] as follows:

$$\tau_{\text{rec}} = R_{RG} C_{\mu} \qquad \tau_{\text{diff}} = R_T C_{\mu}$$

$$D_n = \frac{L_{SCR}^2}{\tau_{\text{diff}}} \qquad \mu_n = \frac{qD_n}{k_B T}$$

τ_{rec} and τ_{diff} represent the lifetime constant for recombination/generation (in dark/light) and the time constant of electrons diffusion respectively, D_n is the diffusion coefficient and μ_n is the electron mobility calculated using the Nernst-Einstein relationship ($k_B T$ is the thermal energy). We extrapolated diffusion parameters summarized in Tab. 2.1-C, at forward bias where we assume the drift contribution to be negligible.

	τ_{diff} [s]	D_n [$cm^2 s^{-1}$]	μ_n [$cm^2 V^{-1} s^{-1}$]
Group 1	10^{-4}	$8 \cdot 10^{-7}$	$3 \cdot 10^{-5}$
Group 3	10^{-3}	$1 \cdot 10^{-7}$	$4 \cdot 10^{-6}$

Tab. 2.1-C Electrons diffusion lifetime, diffusion coefficient and electron mobility extrapolated at forward bias for group 1 and 3 cells.

In Fig. 2.1.12 we notice that, although the recombination time constant behavior is similar for group 1 and group 3, there is a constant offset separating the two curves. We will discuss a possible explanation for this shift between fresh and degraded cells in the next section.

Finally, we remark that obtained electrons mobility in PCBM (see Tab. 2.1-C) is compatible with results reported in other works [72,73], although there is more than an order of magnitude of variability in literature [44].

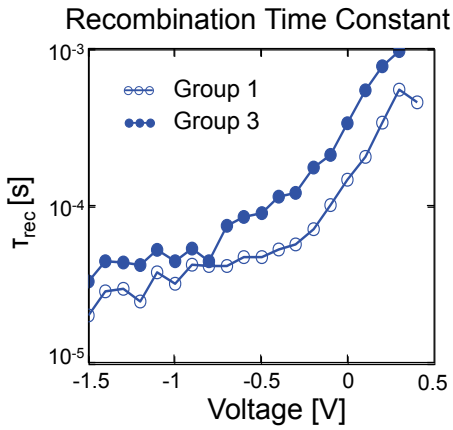

Fig. 2.1.12 Recombination time constant extrapolated from model fitting to IS measurement data performed in dark. Open symbols represent group 1 cells, filled symbols group 3 cells.

2.1.4.2 Comparison between fresh and UV degraded devices

Fig. 2.1.13, Fig. 2.1.14, Fig. 2.1.15 and Fig. 2.1.16 show some of IS data we measured on cells of group 1 and 3. We omitted a direct comparison of IS representing group 2 since they are similar to group 1 and no significance differences are visible. A comparison of reverse bias voltage IS at 1–sun illumination of a fresh cell (Fig. 2.1.13) and a degraded cell (Fig. 2.1.14) does not lead to an immediate distinction. The amplitudes of the impedance peaks are the main differences at reverse bias voltage. The fresh cell IS starts at 0V with a maximum imaginary peak amplitude around 200 Ω and ends at more than 600 Ω at -1.5V. On the other hand, the degraded cell IS imaginary peak starts at less than 100 Ω at 0V and stops at 400 Ω at -1.5V.

A clear distinguish between fresh and degraded cells is possible observing forward IS measurements. Fig. 2.1.15 and Fig. 2.1.16 show the IS run at 0.5V with decreasing illumination levels. Comparing Fig. 2.1.15 and Fig. 2.1.16, we notice that while in fresh cells we clearly identify two different peaks at forward bias in particular at high illumination levels, these peaks are not visible in UV degraded cells. In Fig. 2.1.15 we clearly distinguish the presence of a high frequency (HF) peak and a low frequency (LF) peak. On the other hand, the same set of data represented in Fig. 2.1.16 for a degraded cell does not allow the identification of the two different peaks, although we performed measurements at the same bias and illumination level.

Since the main variation between cells from group 1 and group 3 is the UV exposure of the “Flextrode” during fabrication, we argue that the shift of the HF peak to lower frequency is due to ZnO degradation induced by UV light. As previously demonstrated by Fig. 2.1.8, fitting our model into group 3 experimental data results in the identification of 2 comparable peaks (ZnO and SCR) similar in amplitude and frequency position for some specific bias and illumination. Thus, we associate the shifted peak to ZnO impedance that moves to lower frequency in degraded cells, merging with SCR peak in a single frequency dispersed peak.

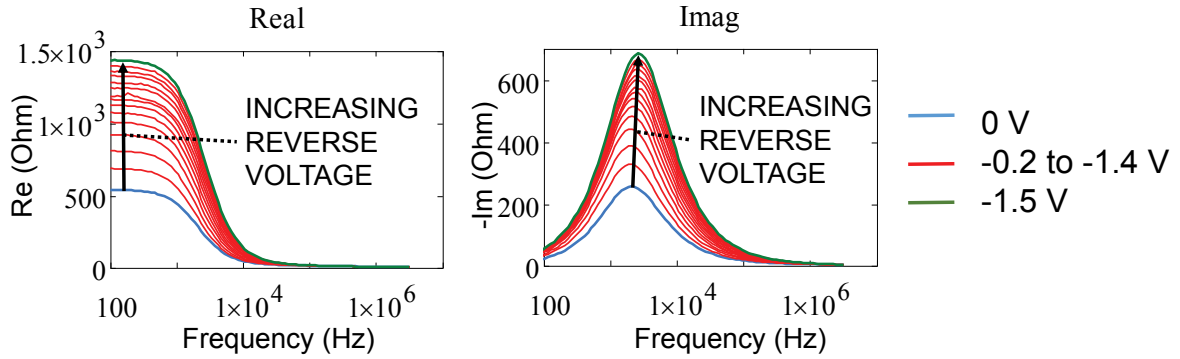

Fig. 2.1.13 Experimental IS of a group 1 with bias varying from 0 V to -1.5 V (increasing reverse applied voltage) at 1 Sun.

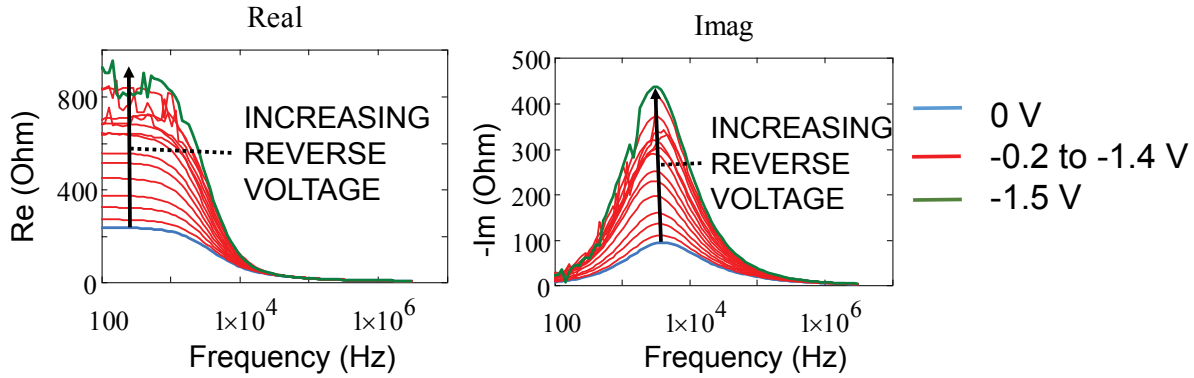

Fig. 2.1.14 Experimental IS of a group 3 cell with bias varying from 0 V to -1.5 V (increasing reverse applied voltage) at 1 Sun.

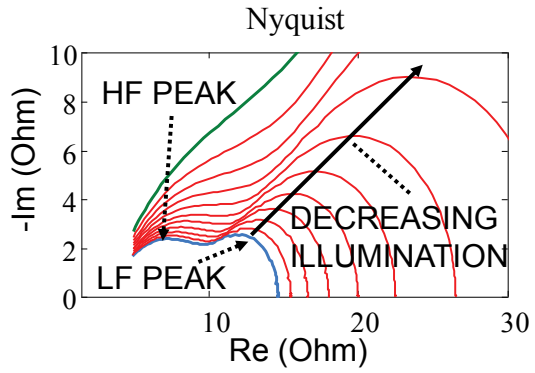

Fig. 2.1.15 Experimental IS of a group 1 cell with decreasing illumination from 2 to 0 Sun at 0.5 V.

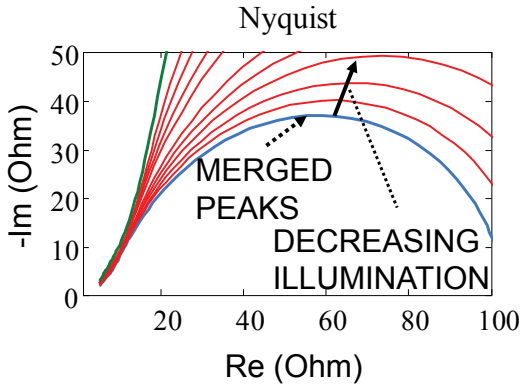

Fig. 2.1.16 Experimental IS of a group 3 cell with decreasing illumination from 2 to 0 Sun at 0.5 V.

Comparing extrapolated parameters in Fig. 2.1.9 and Fig. 2.1.11, for fresh and degraded cells respectively, we notice that although the voltage and illumination dependence is qualitatively similar, the parameter values are quantitatively different. In particular, R_{RG} variation on degraded cells is more than two orders of magnitude smaller than in fresh cells. The same occurs for C_μ variation that is visibly reduced. We explain this change of the parameters dependency from bias, observing the different results obtained for Z_{ZnO} parameters extracted with our model. Referring to data in Tab. 2.1-B, containing averaged value of Z_{ZnO} parameters, and comparing the amplitude of ZnO peak in Fig. 2.1.6 and Fig. 2.1.8 we notice especially from the real part at low frequency (approaching DC) of the Z_{ZnO}, that this impedance is much bigger in degraded cells than fresh ones. The presence in group 3 of a higher ZnO interface resistance that is more than an order of magnitude bigger than in a fresh cell, leads to a higher voltage drop at this interface in both DC and AC measurements. We argue that due to a bigger resistance at the ZnO-blend interface, the voltage drop across this interface drastically increases.

Furthermore, extrapolated fitting parameters (Fig. 2.1.11) from degraded cells do not clearly saturate in reverse bias as in fresh cells (Fig. 2.1.9). We suggest that the electric field dropping across SCR in degraded cells is smaller; applying up to -1.5V reverse voltage does not lead to saturation of SCR width. Thus, the reduced electric field in the SCR does not allow a direct comparison of extracted parameters.

Observing experimental data, we suggest that due to the voltage drop across ZnO interface, we have to compare the values obtained on degraded cells with values extrapolated on fresh cells in a range of bias from -0.8V to 0.1V. Indeed, we can compare both quantitatively and qualitatively parameters shown in Fig. 2.1.11 with those shown in Fig. 2.1.9 in the described range.

The increased voltage drop across ZnO interface would justify also the noisy results on fitting $1/C_{SCR}^2$ curves on group 3 cells, shown in Fig. 2.1.10b. We could not obtain a clear trend of the $1/C_{SCR}^2$ data since we are not at high reverse bias voltage due to low polarization of the SCR.

Finally, the lower electric field applied to the SCR of degraded cells leads to the impedance evolution observed in Fig. 2.1.8, Fig. 2.1.14 and Fig. 2.1.16. The SCR peak at forward voltage is larger than expected due to the lower electric field apply, hence it is comparable with the ZnO peak although we are applying an external potential up to 0.5V. The total impedance is the sum of these undistinguishable components.

2.1.5 Summary

We analyzed heterojunction P3HT:PCBM solar cell by means of I-V and IS measurements at various bias voltage and illumination intensity. This large collection of data allows obtaining a more comprehensive picture of IS peaks and permits us to elaborate a wider model for describing the cell characteristics.

ZnO generates a peak at high frequency in IS curves of fresh cells. This peak moves towards lower frequency values and increases in size when ZnO is degraded by exposing the electrode to UV during the fabrication process. The main peak, which widely varies with increasing reverse bias voltage and illumination, is ascribed to the Space Charge Region impedance. This agrees with the evolution of the extracted parameters as a function of bias and illumination. In particular:

- C_{SCR} decreases in size with increasing reverse bias applied, as expected from the increase of the SCR width. Besides, it increases with higher illumination due to resizing of SCR width.
- R_S is almost constant in all theoretical curves, the small variations are consistent with numerical errors and measurements noise. This parameter accounts for the resistance of the Quasi Neutral Regions and the contacts as well. Incidentally, we believe that any illumination dependence of the QNR resistance should be very small because the concentration of photo-generated carriers should be negligible with respect to the pre-existing carriers.
- R_T keeps an almost constant value with bias but it decreases with increasing illumination level. We suggest this relates to the variable number of carriers present in the spatial charge region with illumination variations.
- R_{RG} increases with increasing reverse bias and decreasing illumination, in both cases due to the lower recombination/generation rate. Besides this parameter tends to saturate at high reverse bias in fresh cells.
- C_μ tends to decrease with increasing reverse bias since it is an electrochemical capacitance related to the distance of polarons pairs, which increases with higher electric field. On the other hand it increases with rising illumination level due to the higher number of polarons generated at the donor/acceptor interface.

Noticeably, due to a higher impedance value of ZnO interface, the polarization conditions of SCR in fresh cells and UV degraded ones are definitely dissimilar and we cannot directly compare extracted physical coefficients without taking into account these differences.

2.2 Effects of current stress and thermal storage on polymeric heterojunction P3HT:PCBM solar cell

Section 2.2 is an extracted of the corresponding published paper Ref. J5

2.2.1 Introduction

Many works studied the standard current density vs. voltage and performance parameters degradation of organic solar cells during several types of stress [23,29,37,38]. While these measurements are a useful tool to assess the main device parameters such as open circuit voltage, short circuit current, fill factor and cell efficiency, they can also provide important physical parameters such as generation rate, exciton separation probability [46,55], and built-in potential [41] in organic heterojunction solar cells.

We investigated the effects of accelerated electrical stress in forward bias condition and thermal storage on these parameters. Forward bias electrical stress emulates the conditions at which a (partially) shaded cell might be brought. In fact, shading due to clouds or dust is a very common scenario that might negatively affect the whole panel reliability. Thermal stress, instead, emulates the heating due to the sun exposure and internal losses. Besides standard I-V measurements, we also employed the Impedance Spectroscopy (IS) technique to obtain a more comprehensive picture of the cell degradation phenomena.

2.2.2 Methods

The 1-cm^2 active area cells are manufactured in roll-to-roll compatible process using a mini-roll coater [32,74]. The active layer of P3HT:PCBM is sandwiched between the front electrode (Flextrodes) consisting of Ag grid, PEDOT:PSS and ZnO and a back electrode of PEDOT:PSS hole transport\electron blocking layer and Ag grid electrode. We used two types of accelerated stress: constant current stress (CCS) in forward bias conditions at 70mA/cm^2, 100mA/cm^2, and 150mA/cm^2 in dark and under 1-sun illumination and thermal storage (TS) at 100°C, 110°C, and 120°C without bias. We periodically stopped the stress to monitor device degradation by means of I-V and IS measurements in both light and dark. IS is taken at 0.5V forward bias (close to the open circuit voltage) in a frequency range from 100Hz to 8MHz. I-V is taken with a voltage from -2.5V to 1V. The total stress time is around 7h for CCS and 31h for TS. We used the Agilent E5263A Parameter analyzer for I-V measurements and Solartron 1260A Impedance/Gain-phase analyzer for IS measurements. We illuminated the cells by using a white LED because the measurement noise floor generated by white LED is much lower, compared to a xenon solar simulator.

2.2.3 Results and Discussions

2.2.3.1 Electrical Stress – CCS

Fig. 2.2.1, Fig. 2.2.2, Fig. 2.2.3, Fig. 2.2.4 and Fig. 2.2.5 summarize the effects of CCS. Fig. 2.2.1 shows the short circuit current density (J_{SC}) during electrical stress. We normalized the values to those measured before stress. J_{SC} decreases monotonically in all the devices and the reduction rate increases for increasing stress current levels. Moreover, if we perform CCSs under illumination, the degradation rate reduces with respect to those performed in dark. This may be associated with a moderate illumination-induced self-heating, which leads to a partial recovery of the CCS induced damage. In fact, when we carry out CCS under illumination, the optical power (100mW/cm^2) results in a slight increase of the device temperature, and in turn, self-annealing, accordingly with our previous findings [23].

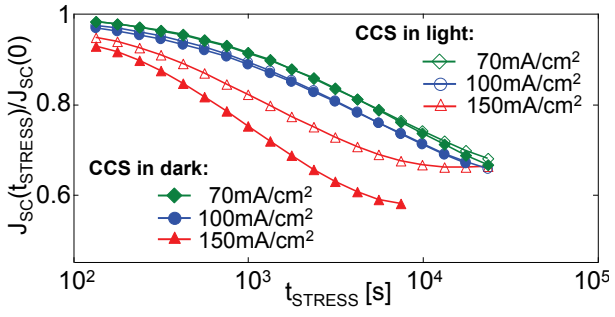

Fig. 2.2.1 Short circuit current (normalized to the fresh value) measured during CCS at different stress current level performed both in dark and under illumination.

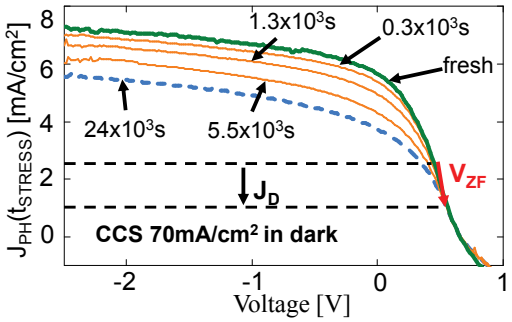

Fig. 2.2.2 Photo-generated current of a cell that underwent CCS at 70mA/cm^2 in dark. Only few of the time steps are plotted for a better clarity. Straight dashed lines describe the diffusion current density at zero-field voltage variation.

In order to gain a more comprehensive picture of the effects of an electrical stress on the photocurrent generation capability of organic solar cells, we calculate the net photocurrent density (J_{PH}) by subtraction of the I-V taken under illumination and in dark. Fig. 2.2.2 shows the resulting photocurrent of one of the cells subjected to CCS at 70mA/cm^2 in dark. In this plot the solid bold (green) line represents the fresh device, the dashed bold (blue) line represents the last step of stress and three solid thin (orange) lines are three intermediate steps.

To extrapolate information from the photocurrent, we used the following model:

$$J_{PH} = qGL\left[coth\left(\frac{V-V_{ZF}}{2V_T}\right) - \frac{2V_T}{V-V_{ZF}}\right] P\left(\frac{V-V_{ZF}}{L}\right) + J_D \qquad (1)$$

Eq. (1) is based on the Sokel-Hughes model for photoconductivity in insulator [46], modified to account also for the dissociation of charge transfer states (P), accordingly to the Braun-Onsager theory [55,56]. In Eq. (1) we defined V the bias applied to the cell, V_{ZF} the voltage corresponding to the nearly zero-field within the active layer (corresponding to an almost flat band condition), L the thickness of the film and G the net generation rate of polaron pairs. P is the function describing the separation probability of a bound polaron pair into two free polarons, which is electric field dependent. Furthermore, we added a constant diffusion contribution (J_D) as described by Limpinsel et al. [41] and Ooi et al.[40] in their analysis to account for the non-ideal contacts and non-constant electric field in the close proximity of the electrodes. In fact, at $V=V_{ZF}$ the cell reach a nearly-flat band state within the active layer. Following the original model from Sokel-

Huges, this should occur when the applied voltage is equal to the difference between the electrode work functions, which is the same point where the photocurrent becomes zero. Instead, due to non-ideal contacts, the zero field condition occurs at a smaller voltage. Hence, charge extraction is still possible. Following the analysis of Ooi [40], the potential barriers at the active layer-electrodes interfaces allow a small diffusion current (J_D) to flow, although the electric field is zero or slightly positive in most of the active layer. In order to distinguish between zero-field condition and zero-photocurrent condition, in the following we will refer to zero field voltage as V_{ZF} and zero-photocurrent voltage as V_{PH0}. For further details on the model the reader may refer to the works of Limpinsel et al.[41] and Ooi et al.[40].

In the plot of Fig. 2.2.2 we underlined also the zero-field voltage and the diffusion current reduction. In Fig. 2.2.3, we show the behavior of V_{ZF} variations during CCS, with respect to its initial value. We notice a general increase of the V_{ZF}, up to 90mV in the worst case (CCS at 150mA/cm^2 in dark). In Fig. 2.2.4, we show the decrease of J_D as a function of the stress time during CCS at different current levels and illumination conditions. Finally, Fig. 2.2.5 shows the estimated separation probability extracted from the photocurrent according to the model of Eq. (1). We notice that for high electric field the separation probability tends to converge to 1, however at low electric field the differences from step to step are more pronounced.

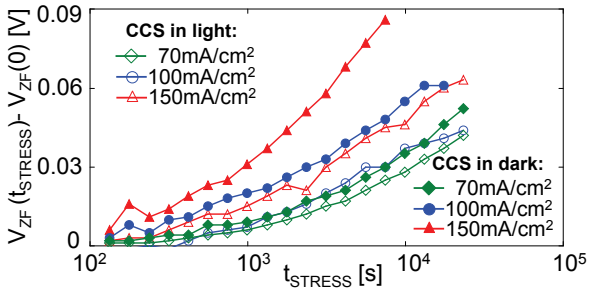

Fig. 2.2.3 Normalized zero-field voltage (V_{ZF}) during CCS at different stress current levels performed both in dark and under illumination.

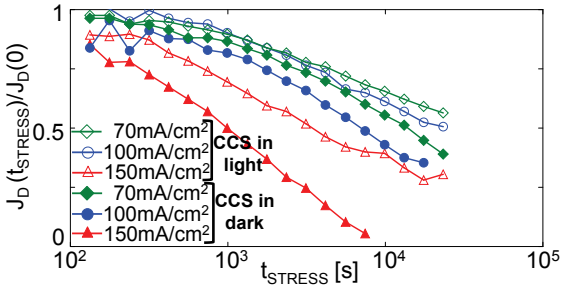

Fig. 2.2.4 Normalized diffusion current density (J_D) contribution at zero-field voltage (V_{ZF}) during CCS at different stress current level performed both in dark and under illumination. J_D during CCS in dark is described with filled symbols, while empty symbols are used for CCS in light.

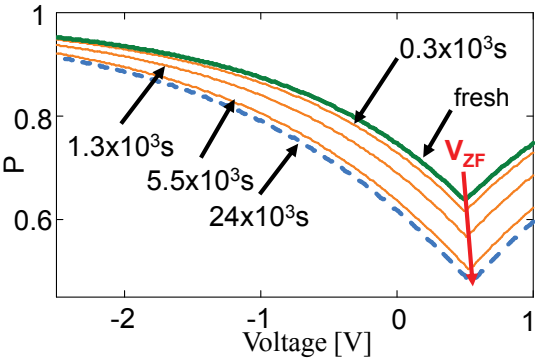

Fig. 2.2.5 Separation probability during CCS at 70mA/cm^2 in dark. P(E) is symmetrical to the zero field voltage. We plotted the same time steps as the photocurrent shown in Fig. 2.2.2.

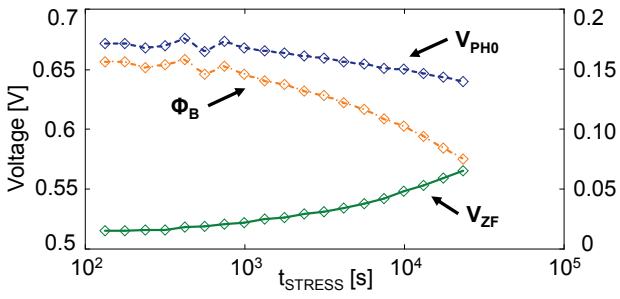

Fig. 2.2.6 Variation of V_{PH0}, V_{ZF} and Φ_B with time of stress during the CCS at 70mA/cm^2. Right scale refers to the potential barrier while left scale to the zero-field voltage and the V_{PH0}.

There are several phenomena contributing to the variation of the short circuit current during CCS. One is the separation probability (see for instance Fig. 2.2.5), which contributes to the reduction of the field dependent photocurrent by up to 38% in the worst-case scenario, i.e., the CCS at 150 mA/cm^2 in dark. Another contribution comes from the V_{ZF} shift that, in turn, has an impact on the diffusion current J_D. We related V_{ZF} shift during CCS to the oxidation of P3HT [73,75]. As previously observed in literature, the exposure of P3HT to oxygen increases the p-type doping, moving the P3HT Fermi level toward the HOMO band. We believe that oxygen and moisture are present during fabrication process and they may permeate the encapsulation layers reaching the active layer [76,77]. The electrical stress may accelerate the oxidation, increasing the effective doping and thus increasing the V_{ZF} value. As expected the higher the CCS current the higher the oxidation rate is.

We may explain the V_{ZF} dependence from the CCS currents and conditions with both the increase of the applied voltage required to maintain the imposed forward current and the temperature increase due to self-heating that can thermally assist in the chemical reactions. Incidentally, in [23] we measured that temperature may increase up to 90 °C during CCS at 150mA/cm^2 in dark. The illumination during CCS produces only marginal changes, probably due to the slightly smaller voltage required to set the CCS current.

Following the analysis of refs. [40,41], the sum of the potential barriers at the interfaces is responsible for the diffusion current J_D. According to the model, we calculate Φ_B as:

$$\Phi_B = V_{PH0} - V_{ZF}. \qquad (2)$$

In Fig. 2.2.6 we show a comparison of V_{ZF}, V_{PH0} and Φ_B during one of the CCS stresses that represents the behavior observed in all CCSs. We notice that while V_{ZF} increases with time of stress (attributed to an increase of p-doping of P3HT), V_{PH0} decreases and thus the barrier Φ_B decreases. Φ_B decrease is one of the possible contributions responsible for the decay of J_D. Indeed, a lowering of the potential barriers decreases the amount of charge extracted at the correct electrode.

The calculation of the diffusion current during CCS, reported in Fig. 2.2.4, confirms previous observations. J_D is the diffusion current at the zero-field potential V_{ZF} and relates to both photo-generation within the blend and selectiveness of contacts. A decrease of diffusion current indicates that the number of dissociated donor/acceptor pairs extracted by diffusion from the active layer is decreasing with the stress time [40]. We observe from experimental data that J_D decays in all performed CCSs. However, we cannot distinguish the generation rate from the potential barrier contribution to the J_D decay. Furthermore, the behavior of J_D and J_{SC} are alike, but not identical. Indeed, while short circuit current (Fig. 2.2.1) on CCSs at high forward bias (150mA\cm^2) tends to saturate, J_D does not. This is a further confirmation that we cannot entirely ascribe the decay of the J_{SC} to this parameter, but the separation probability considerably contributes to the variations of photocurrent.

Finally, to underline the relation between the zero-field potential and the diffusion current density, we notice that the behaviors of these two parameters with time and current of stress are rather similar. The faster is the approach of V_{ZF} to V_{PH0}, the higher is the decay of J_D, as we notice by comparing Figs. 4 and 6. In particular, when Φ_B approaches 0V, as for CCS at 150mA/cm^2, the diffusion current J_D tends to disappear. This enforces the validity of the model applied to elaborate the measurements.

2.2.3.2 Thermal Storage – TS

Fig. 2.2.7 to Fig. 2.2.10 describe the results obtained from the thermal storage stress. Fig. 2.2.7 shows the effects of the TS on J_{SC}, which is very sensitive to the storage temperature and storage time. At 120°C, the thermal storage produces significant damage. Indeed, after the first hour of stress the short circuit current is reduced by up to 50%. Instead, at 110°C we observe an initial small recovery (in the first 3 hours) and then a reduction of J_{SC}. Finally, at 100°C we observe no significant variations except for a marginal recovery, at least for a storage time as long as 31 hours.

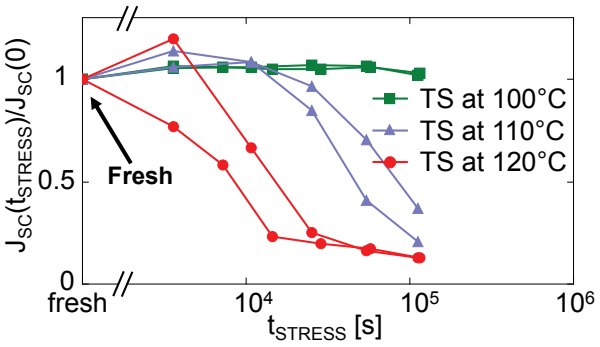

Fig. 2.2.7 Normalized short circuit current density during thermal storage at three different temperatures. TS at 100°C is represented by green squares, TS at 110°C by blue triangles while TS at 120°C by red filled circles. The same legend is used in Figs. 9 and 10.

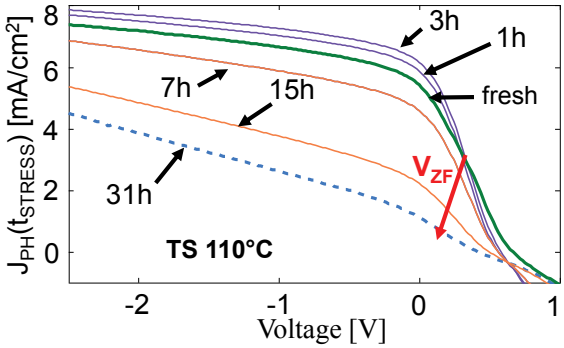

Fig. 2.2.8 Photo-generated current of a cell that underwent TS at 110°C. Bold green line is the fresh photocurrent, purple lines indicate the photocurrent during the first 3h of storage, orange and dashed blue lines describe the photocurrent during longer TS steps.

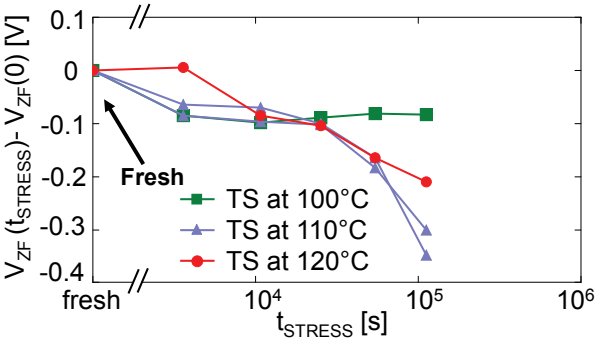

Fig. 2.2.9 Zero-field voltage variations during thermal storage. Values are normalized to V_{ZF} before applying TS.

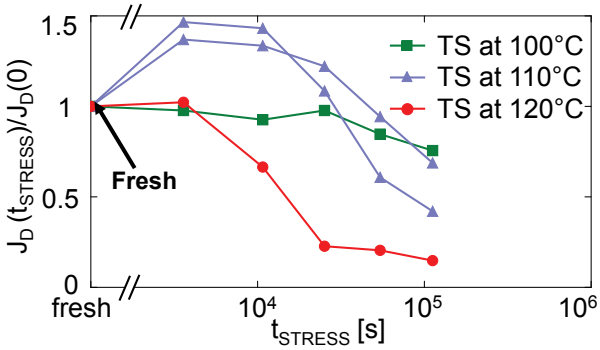

Fig. 2.2.10 Normalized diffusion current density at V_{ZF} during TS at different temperature.

Fig. 2.2.8 shows the typical behavior of the photocurrent of one of the TS performed at 110°C. In contrast to the CCS, during TS we observe that photocurrent may undergo a partial recovery together with the degradation process. In fact, during first stress steps (within 3h) we notice that the photocurrent is larger than the fresh device in reverse conditions or under a moderately forward bias, even though the zero-field voltage is always decreasing, as highlighted in Fig. 2.2.9. In Fig. 2.2.9 we see a reduction of V_{ZF} that is up to an order of magnitude bigger than the variation observed during CCS

and in the opposite direction. Besides, while at 100°C the decay seems to stabilize at least within 31h, at 110°C and 120°C V_{ZF} keeps decreasing even after 31 hours. Finally, Fig. 2.2.10 shows the diffusion current density J_D during TS as a function of the time of stress. During the 100-°C storage stress, J_D shows only moderate variation accordingly with the almost constant V_{ZF}. At 110°C J_D shows an initial increase and starts decreasing after 3 hours. The initial increase of J_D agrees with the reduction of V_{ZF} as was discussed earlier. In fact, the reduction of V_{ZF} is a signature of an increase of the residual barrier at the contacts, which increases the contribution of the diffusion current J_D. However, the reduction of J_D after 3 hours of thermal storage is apparently in contrast with the monotonic reduction of V_{ZF}. During the 120-°C stress the diffusion current is always decreasing, in contrast to the behavior of V_{ZF}.

To explain the differences between electrical stress and thermal storage a couple of considerations must be drawn. Firstly, during CCS the variation of V_{ZF} comes from an increase of effective doping due to P3HT oxidation. If we attempt to ascribe the V_{ZF} variation during thermal stress to the same phenomenon, this should result in a decrease up to five orders of magnitude in P3HT doping concentration, making the polymer undoped. Such variations have been observed in several works [76–80], but at temperatures as high as 150°C and in high vacuum chamber, which is not our case. Secondly, the reduction of both V_{ZF} and J_D during thermal stress, suggest that other mechanisms should be held responsible for the photocurrent reduction, apart from the lowering of the interface barriers.

In light of these considerations, we suggest that photocurrent reduction is due to some thermally induced morphological changes in the active layer. Noticeably, our stress temperatures are close to the glass transition point of the active layer, which is estimated to be 110°C [78,79]. This could explain why at 100°C thermal stress we observe only minor changes in the short circuit current and, in general, in all the cell performances. Instead, at higher temperature (110-120°C) some morphological rearrangements can take place, in particular phase separation, which reduces the separation rate of polaron pairs, and in turn the net free carrier generation [80,81]. In fact, it is well known that, in polymeric solar cells, charge generation requires that the excitons reach a donor-acceptor interface, within their diffusion length (which is in the range of 5-10nm). In the phase separation process the creation of large islands reduces the effective acceptor-donor interface area and thus, the number of possible sites where excitons may be efficiently dissociated. In this way, the probability that an exciton is generated in close proximity of an acceptor-donor complex is reduced.

2.2.3.3 Impedance Spectroscopy – IS

Fig. 2.2.11 and Fig. 2.2.12 show two representative examples of IS measurements performed at 0.5V forward bias under illumination during TS at 120°C and CCS at 150mA/cm^2 in light respectively. We notice the presence of two peaks of the imaginary part in both stresses, the first one at high frequency (MHz) and the second one at low frequency (10kHz). These peaks behave differently during TS and CCS. TS induces an increase in the intensity of both peaks and a shift of the peaks position to lower frequency. On the other hand, CCS slightly varies just the amplitude of the peak at low frequency while the peak at high frequency seems unchanged. These variations are underlined in the real part of IS, where we fitted impedance data (symbols) using the IS model (lines) suggested in ref. [43].

According to this and other models present in literature [45] the peak at low frequency is related to the active layer, and the peak at high frequency to the ZnO interface. Thus, the differences observed in peaks variations can be related to

different degradations induced by each stress on a specific layer of the cells. CCS, by forcing forward current into the cells, degrades the active layer much more than the ZnO interface. This results in a clear variation of the active layer peak and in almost constant amplitude of ZnO peak. On the other hand, TS degrades both the active layer and ZnO interface. The high level of degradation of the ZnO interface may be responsible for the observed reduction of V_{ZF} that is huge compared to what we observe during CCS.

ZnO degradation, in parallel to TS effects on the active layer could generate very high barriers at interfaces leading to the reduction of V_{ZF} observed in Fig. 2.2.9. Thus, IS confirms our interpretation on the effects of CCS and thermal storage.

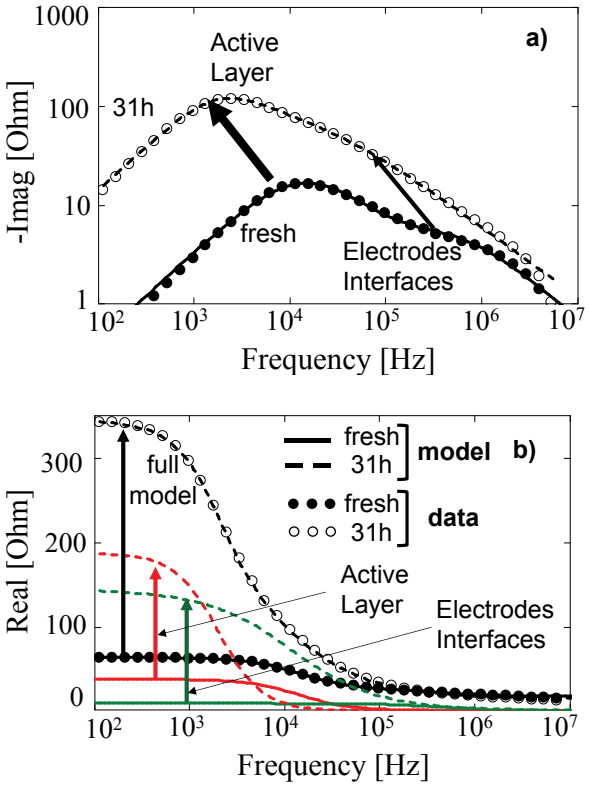

Fig. 2.2.11 Imaginary part (a) and real part (b) of the IS measured during TS at 120°C. Filled symbols represent the fresh device, empty symbols correspond to the last step of stress. Continuous and dashed lines describe the fitting model. Real part (b) contains also the fit of each part of the model that we applied. The active layer is described with red lines while the electrodes interfaces with green lines.

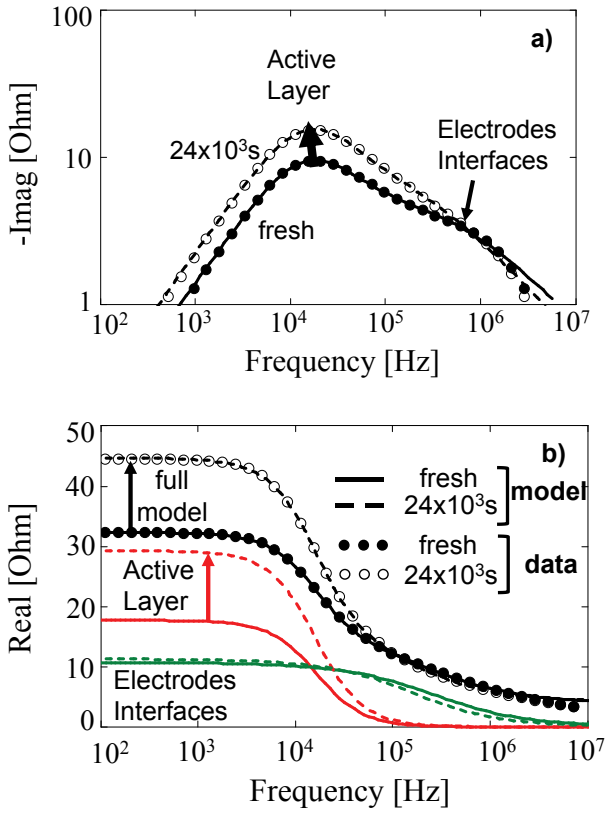

Fig. 2.2.12 Imaginary part (a) and real part (b) of the IS measured during CCS at 150mA/cm2 in light. Filled symbols represent the fresh device, empty symbols correspond to the last step of stress. Continuous and dashed lines describe the fitting model. Real part (b) contains also the fit of each part of the model that we applied. The active layer is described with red lines while the electrodes interfaces with green lines. During CCS the electrodes interfaces contribution to IS is almost unchanged, while the active layer contribution is responsible for the main variations.

2.2.4 Summary

We performed electrical stress at forward current and thermal storage on P3HT:PCBM solar cells. During electrical stress, we applied several levels of current both in dark and under illumination, and we tested three different temperatures for thermal storage. Applying a modified version of the Sokel-Hughes/Braun-Onsager model, we extracted the diffusion photocurrent contribution at the zero-field voltage and we analyzed the variations of these two parameters with stress time. Stresses generate both degradation and recovery on solar cells. During CCS we observe an increase of the V_{ZF} for all devices and we related this shift to the p-doping induced by oxidation process within P3HT.

Differently, TS induces a huge decrease of quasi-flat band voltage that we cannot relate only to the doping level of the P3HT. Moreover, the TS may induce a recovery of the diffusion current density depending on the time of storage and if the temperature of stress is above or below the glass transition point. A possible explanation for observed variations is that a phase change occurs within the cells that induce a rearrangement of the active layer morphology.

Finally, we proved that IS performed during stresses allow a better comprehension of interface degradation. Indeed, with IS we clearly observe that CCS and TS generate different damages on the active layer and the ZnO interface.

2.3 Application of photocurrent model on polymer solar cells under forward bias stress

Section 2.3 is an extracted of the corresponding published paper Ref. J8

2.3.1 Introduction

Among the several environmental conditions affecting organic solar cells reliability, light exposure is especially critical in flexible organic photovoltaic. In organic photovoltaic module, the architectonic application on curved surfaces is responsible for partially shadowing cells. Thus, illumination conditions might be not optimal and not uniform over the whole module, due to architectonic constrains. These conditions may force the shaded or partially shaded cells in the module to operate in forward or reverse bias, accordingly to the type of connections used in the module between the cells. These types of stress may negatively affect the reliability of the whole panel.

In this section, the forward bias stress emulates the situation of a partially shaded module with parallel-connected cells, when a cell is brought to forward bias due to the module connections. We analyzed the evolution of the physical parameters during accelerated electrical stress in forward bias condition. We estimated them by applying an existing photocurrent model and we investigated the parameters behavior during the stress.

2.3.2 Methods

We assembled the 1-cm^2 active area cells in roll-to-roll compatible process with a mini-roll coater [82]. The front electrode (Flextrode) is composed of an Ag grid, PEDOT:PSS and ZnO, and the back electrode consists of PEDOT:PSS and the Ag grid encloses the blend of P3HT:PCBM.

We applied forward bias accelerated stress at 70mA/cm^2, 100mA/cm^2, and 150mA/cm^2 constant currents (CCS) in dark and under illumination. We systematically paused the stress to monitor devices conditions by means of I-V measurements in both light and dark. We performed I-V with a voltage from -2.5V to 1V. The total stress time was 7h. An Agilent E5263A Parameter analyzer was used for both the I-V measurements and the stress. We illuminated the cells by using a white LED because the measurement noise floor generated by white LED is much lower, compared to a xenon solar simulator. Besides, we used white LEDs because of its very low content in UV wavelengths and low power dissipation. These properties of the LEDs allow a reduction of the degradations induced by the light source (UV and thermal effects) so that we could better isolate the sole effect of the CCS on the devices. We calibrated the LED intensity to reach a cell illumination level equivalent to that obtained by a solar simulator at 1 sun. We verified that the short circuit current under LED illumination and solar simulator illumination at 1 sun have the same values, as well as all other important figure of merits (fill-factor, efficiency, etc). Finally, we used a PVE300 spectral responsivity analyzer to perform External Quantum Efficiency (EQE) measurements.

2.3.3 Results and Discussions

2.3.3.1 Figures of merit degradation during CCS

The devices we build reach an average efficiency of 1.2-1.3% with an open voltage of 0.55V and an average short circuit current density of 5 mA/cm^2 [34]. Although the efficiency is lower than other polymeric organic solar cell devices reported in literature [83–86], we underline that we do not process these devices under controlled environment. Indeed, we use a semi-automatic mini-roll coater under environmental air. The usage of a glove-box and a spin-coater would probably increase such efficiency, allowing the reaching of higher performances. However, glove-box processing and devices spin-coating are not the real conditions applied during roll-to-roll mass production. Thus, both the uncontrolled environment and the not fully automatized process may lead to an efficiency reduction. On the other hand, such devices are closer to the cells built on real photovoltaic modules since they undergo the same processing [8].

Fig. 2.3.1 show the evolution of the short circuit current density (J_{SC}) and normalized efficiency (η) as a function of the stress time, respectively. In Fig. 2.3.1a we notice that, independent of the applied stress current, all the CCS induced a monotonic decrease of the J_{SC} and the rate of decay was increasing with the stress current. Noticeably, for the larger stress current value (150 mA/cm^2) under illumination (open red triangles), the decay rate seems to slow down during the last stress steps, likely due to an annealing process, which partially compensates the CCS-induced degradation. In fact, the cells temperature reached up to 90°C at 150 mA/cm^2 [23]. The self-heating induced by power dissipation during the stress, induced a partial recovery of the short circuit current density, at least for a stress as long as 25000 seconds.

The efficiency shows a behavior similar to the short circuit current. In Fig. 2.3.1b we plot the efficiency evolution normalized to the fresh value. Despite efficiency generally decreases with increasing stress time and current, there is a small recovery during the last stress steps for high stress current values (150 mA/cm^2), more accentuated under illumination, due to the additional temperature increase induced by the light exposure. This is due to the high temperature reached during the stress, which results in partial annealing of the damage generated in the first part of the stress.

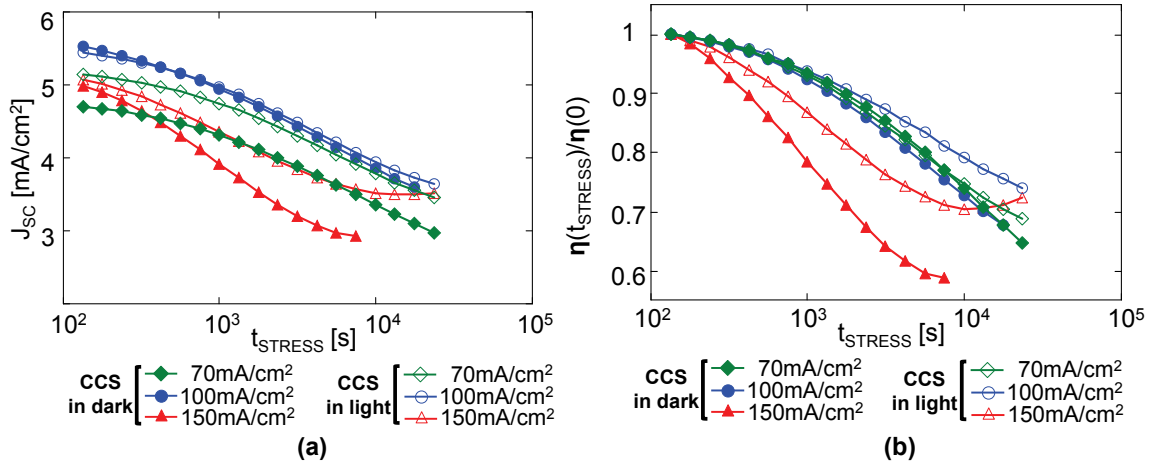

Fig. 2.3.1 Short circuit current density (a) and normalized efficiency (b) as a function of stress time, during CCS.

2.3.3.2 Photocurrent model description

To further investigate the mechanisms behind the degradation/recovery during CCS, we calculated the photocurrent as the difference of light and dark currents:

$$J_{PH} = J_{LIGHT} - J_{DARK} \qquad (1)$$

Where J_{PH} is the photocurrent, J_{LIGHT} is the current density measured under illumination and J_{DARK} the current measured in dark. In order to obtain an accurate value of the photocurrent we also corrected the experimental data to account for the parasitic series resistance. The series resistance value was calculated by means of impedance spectroscopy [19], and it was continuously monitored during the stress. In all the devices, the series resistance ranges between 10Ω and 15 Ω, and it is almost constant during the stress. Remarkably, the current measured in our cells may approach 8mA, which may produce a voltage drop as large as 0.12V in the non-active regions (contacts, zinc oxide layer, etc.) This means that for a given voltage, the actual voltage drop across the active layer might be significantly different when the I-V is measured in dark and light conditions. For this reason, we corrected the I-V curves before subtracting J_{DARK} to J_{LIGHT}. Fig. 2.3.2 shows the effect of the series resistance in both dark and light I-V and the extrapolated photocurrent.

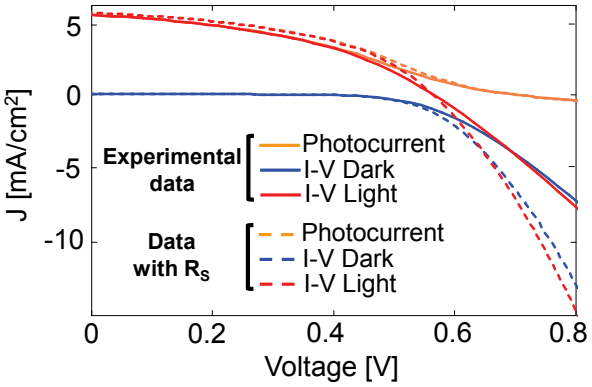

Fig. 2.3.2 Current density in dark/light and photocurrent, without (solid lines) and with (dashed lines) series resistance R_S. In this specific case R_S = 12Ω. The contribution of the series resistance is particularly relevant at high forward bias.

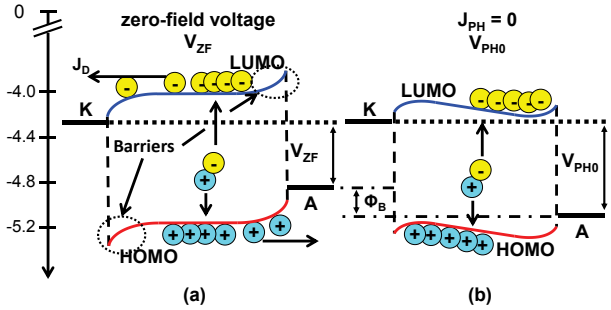

Fig. 2.3.3 (a) band bending at nearly zero-field voltage (V_{ZF}) and (b) at V_{PH0} where the photocurrent is zero. Φ_B represents the additional potential required to reach zero photocurrent.

After series resistance correction, in order to fit to the experimental data we adopted the model proposed in [41], which expresses the photocurrent as the superposition of two contributions:

$$J_{PH} = qGL\left[coth\left(\frac{V-V_{ZF}}{2V_T}\right) - \frac{2V_T}{V-V_{ZF}}\right] P\left(\frac{V-V_{ZF}}{L}\right) + J_D \qquad (2)$$

Equation (2) includes the Sokel-Hughes model for photoconductivity in insulators [46], the Braun-Onsager dissociation probability of polarons charge transfer states (P) [55] and a diffusion current contribution (J_D) firstly introduced by Ooi et al. [39,40] and then employed also by Limpinsel et al. [41]. In (2), G is the average generation rate of polaron pairs (assumed constant all over the active layer); q is the elementary charge; L is the thickness of the active layer; V_T is the thermal voltage; V is the actual voltage drop across the active layer; V_{ZF} is the voltage corresponding to

the nearly zero electric field within the active layer. The function P accounts for the separation probability of a bound polaron pair into two free polarons and it is electric field dependent. Finally, J_D is the current density contribution, which correspond to the current at $V=V_{ZF}$. V_{ZF} substitution to the built-in voltage and J_D current density account for the non-ideal contacts and the non-constant electric field in the close proximity of the electrodes. Indeed, the Sokel-Hughes model considers photoconductivity in insulator where there is no charge accumulation. Thus, Ooi and Limpinsel included J_D and V_{ZF} terms in their models to take account for bend bending due to charge accumulation at interfaces. We invite the reader to refer to reference [39–41] for further details.

Following the adopted model, Fig. 2.3.3 represents a qualitative band diagram that helps understanding the carrier dynamics within the active layer at different operating voltages. Contact interfaces bend due to non-ideal alignment between the blend and the electrodes Fermi levels. The band bending generates two barriers at the contact interfaces preventing electrons flow toward the anode and holes flow toward the cathode. In other words, we may figure the electrodes as partially selective contacts [40]. The higher the barrier, the stronger is the selectivity of the contact. Fig. 2.3.3a describes the situation that occurs when the external applied potential keeps the bulk of the active layer at a nearly zero-field condition. We refer to this applied bias as V_{ZF}. In other words, within the active layer there is a quasi-flat band condition. Then, dissociated charges (electrons/holes) flow to the electrodes by drift in the region close to the contacts and by diffusion in the bulk of the active layer [39,41]. However, since there are selective interfaces that generate barriers, they do not flow equally to anode and cathode but they mostly reach the electrode with lower potential barrier. Thus, the photocurrent generated at V_{ZF} is not zero, giving raise to J_D. The absolute value of J_D relates to both the amount of free carriers generated and the height of the barriers. Fig. 2.3.3b shows the band bending when the photocurrent is zero. We refer as V_{PH0} to the voltage at which the photocurrent is zero. In this case, the model predicts that the band bending within the active layer compensates the barriers height. Thus, by applying V_{PH0}, electrons and holes can equally flow to both cathode and anode, resulting in a zero photocurrent. Although a more sophisticated modeling could improve the accuracy of V_{PH0} and V_{ZF}, as a first approximation, we can figure that the additional potential (defined Φ_B in Fig. 2.3.3) required to move from the quasi flat band (Fig. 2.3.3a) to the zero-photocurrent condition (Fig. 2.3.3b) is correlated to the sum of the band bending at the two interfaces. We may estimate Φ_B as the difference between V_{PH0} and V_{ZF}.

2.3.3.3 Parameter extraction

By fitting the photocurrent with (2), we extrapolated the parameters: J_D, V_{ZF}, Φ_B, G, k_{REC} and k_{SEP} as a function of the stress time, with k_{REC} and k_{SEP} the polaron recombination and separation rates respectively affecting the separation probability P as described by the Braun-Onsager theory [55].

Fig. 2.3.4 shows an example of the fitting results on a cell that underwent CCS at 70mA/cm^2 under light. We observe that when (2) is applied to photocurrent, it gives a very good fit of experimental data in both forward and reverse bias voltages. In Fig. 2.3.4, the series resistance used to account for contacts interfaces and other drops is 12Ω·cm^2 (measured by impedance spectroscopy), and it is compatible with the series resistance measured by other research groups [43,45].

Fig. 2.3.5 and Fig. 2.3.6 show the evolution of J_D and Φ_B respectively. J_D keeps decreasing until last step of stress. We must correlate the decrease of J_D with the decreasing behavior of Φ_B, which is the difference between V_{PHO} and V_{ZF}. The higher is Φ_B the larger are the band bending – and in turn the sum of voltage drops – at the interfaces. The reduction of Φ_B is a clear signature that the voltage drop and the barrier height near the contact are reducing. In turn, this contributes to reduction of the intensity of the diffusion current.

Of course, such a reduction could originate also from the mobility reduction, which affects the diffusion constant by the Einstein relation. However, we extrapolated the evolution of the mobility from the dark current, assuming a Space Charge Limited conduction through the organic layer, and we verified that mobility remains practically unchanged during stress with a value of $\mu = 7.6 \cdot 10^{-3}$ $cm^2V^{-1}s^{-1}$. For this reason, we can neglect the effect of mobility in the diffusion current.

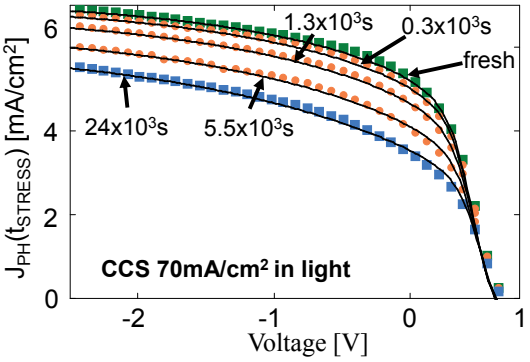

Fig. 2.3.4 Photocurrent experimental data (symbols) and fitting results of model (2) (lines) corrected with a series resistance of 12Ω·cm². The shown stress steps are from a CCS performed at 70mA/cm² in light.

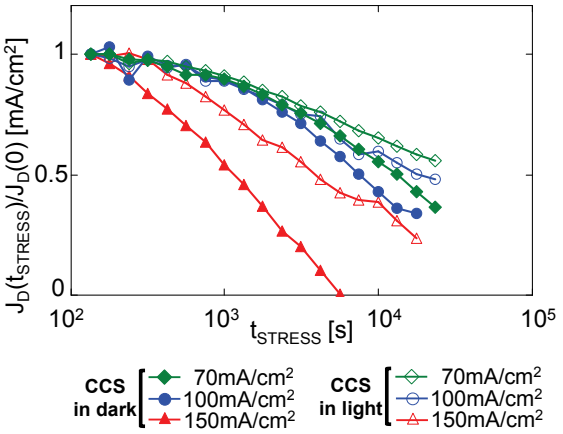

Fig. 2.3.5 Diffusion current J_D normalized to fresh value as a function of stress time.

Fig. 2.3.7 shows the correlation between the diffusion current J_D and the potential Φ_B. Each correlation curve is a straight line. All curves are enclosed into a well-defined band, confirming that higher Φ_B corresponds to higher J_D. Furthermore, as Φ_B decreases during the stress, there is a corresponding reduction of J_D. In particular during CCS at 150 mA/cm^2 in dark (filled red triangles), when Φ_B tends towards zero during last stress steps, J_D gets close to zero as well. In fact, the disappearing of the barrier generates a non-selective contact and, in turn, the diffusion current at nearly zero-field voltage (V_{ZF}) vanishes.

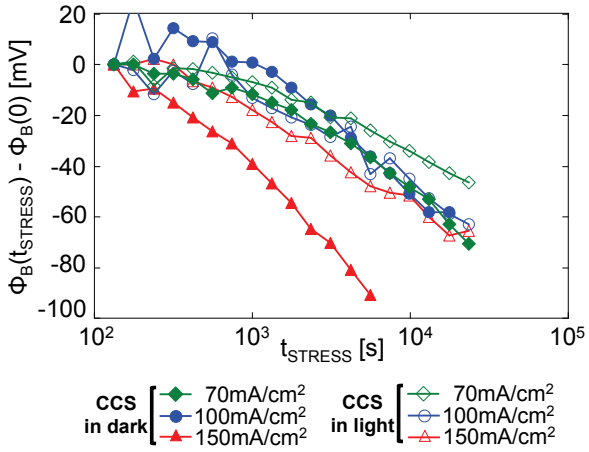

Fig. 2.3.6 Potential Φ_B as a function of the stress time.

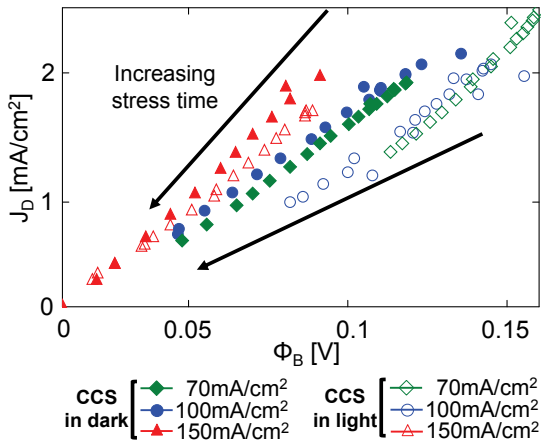

Fig. 2.3.7 Correlation graph between the diffusion current J_D and the voltage Φ_B with stress time.

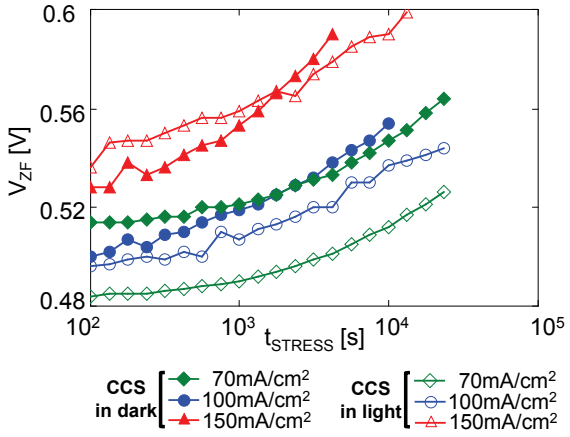

Fig. 2.3.8 Nearly zero-field voltage V_{ZF} as a function of the stress time.

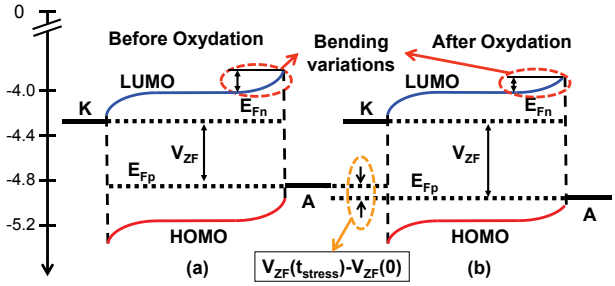

Fig. 2.3.9 Qualitative band banding at the nearly zero field voltage V_{ZF} on a fresh device (a) and after that the oxidation process increased the P3HT doping (b).

The decrease of Φ_B must be associated with the increase of V_{ZF} shown in Fig. 2.3.8. We related the variation of V_{ZF} during stress to the oxidation of P3HT [73,75]. In fact, it has been already observed in literature, that the exposure of P3HT to oxygen increases the p-type doping, shifting the P3HT Fermi level toward the HOMO band. In turn, this reduces the band bending in proximity of the anode, as qualitatively described by the sketch in Fig. 2.3.9. Among the causes for the increase in P3HT doping, oxygen and moisture embedded during the fabrication process can be the primary candidates. In addition, they may also permeate the encapsulation layers reaching the active layer during device operation [76,77]. The electrical stress may accelerate the oxidation process, increasing the effective doping and thus increasing the V_{ZF} value. In fact, the higher the CCS current the higher the oxidation rate is. This may come from both the increase of the applied voltage required to maintain the imposed forward current and the temperature increase due to self-heating that can thermally assist the chemical reactions. Incidentally, in [23] we measured that temperature may increase up to 90 °C during CCS at 150mA/cm^2 in dark.

The illumination during CCS produces only marginal changes, despite the additional device heating expected from the illumination. However, the presence of light during stress decreases the voltage required to set the CCS current. This, in turn, slightly decreases the power dissipation, partially compensating the additional heating induced by illumination.

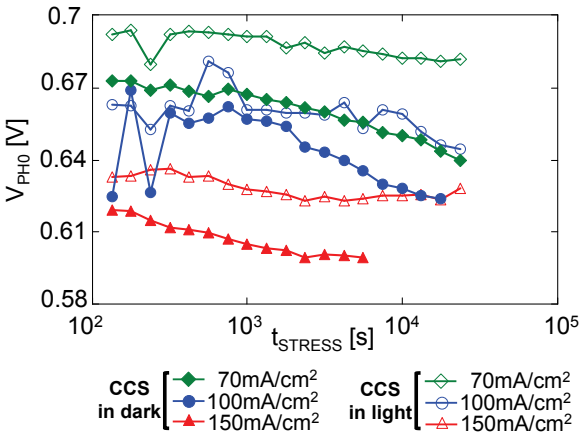

Fig. 2.3.10 Voltage V_{PH0} (corresponding to J_{PH} = 0 mA/cm²) as a function of the stress time.

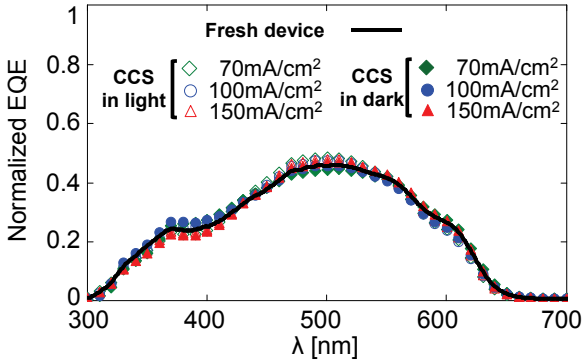

Fig. 2.3.11 Normalized External Quantum Efficiency (EQE) comparison between a fresh cell (black line) and cells that underwent CCS at 70, 100 and 150mA/cm² both in light and in dark (symbols).

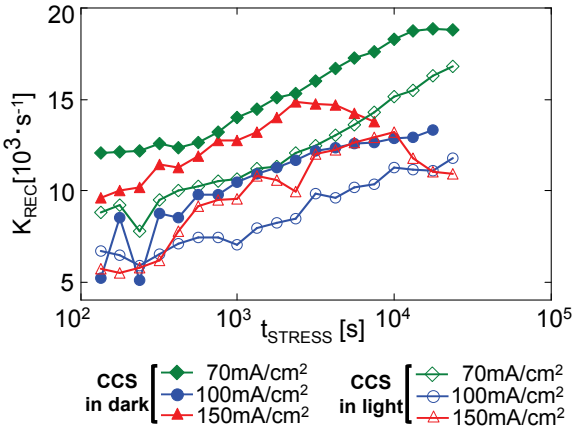

Fig. 2.3.12 Recombination rate of polaron charge transfer states with time of stress.

Fig. 2.3.10 shows the voltage corresponding to the zero of the photocurrent as a function of the stress time. $V_{PH0} = V_{ZF} + \Phi_B$ decreases with stress time due to the higher decrease of the potential Φ_B compared to the increase of V_{ZF}.

When comparing the evolution of J_{SC} in Fig. 2.3.1a and J_D in Fig. 2.3.5 during stress, we observe a very different behavior. For instance, during CCS at 150 mA/cm² under illumination J_D keeps always decreasing down to almost zero, while J_{SC} slowly decreases with a saturating behavior after 10000 seconds. This clearly indicates that the decay of the short circuit current density cannot originate only from J_D, but also the generation rate and dissociation probability play important roles. However, the generation rate of polaron pairs G extrapolated from photocurrent is constant with stress

time, independently on the CCS current or illumination conditions. We calculated that G = 1.08±0.07·10^{21} $cm^{-3}s^{-1}$. EQE measurements further confirms that G is constant. Fig. 2.3.11 shows the EQE as a function of radiation wavelength normalized on its area, for both fresh and stressed cells. No significant variations are observed, indicating that the absorption spectrum shape of the blend is constant during CCS. It is worth clarifying again and the reader should bear in mind that the absolute EQE for degraded sample is lower than for the fresh sample and here the normalized data is presented instead for better indication of no changes in the curve shape and thus in the absorption. This is a signature that no changes occur to the generation rate of bounded polaron pairs, confirming the idea that the stress does not affect G.

Since G is almost constant, the variation of the short circuit current must derive from the change of polaron recombination and/or separation rates. Following the Braun-Onsager theory, the separation rate is [55]:

$$k_{SEP} = k_{SEP0}\frac{J_1\left(2\sqrt{-2b}\right)}{2\sqrt{-2b}}$$
$$k_{SEP0} = \frac{3q\langle\mu\rangle}{4\pi a^3\varepsilon}e^{-\frac{\Delta E}{kT}} \quad b = \frac{q^3F}{8\pi\varepsilon k^2T^2} \tag{3}$$

Where J_1 is the first order Bessel function, q is the elementary charge, *a* is the average molecular distance, <μ> is the average mobility ($7.6\cdot10^{-3}cm^2V^{-1}s^{-1}$ in our case), ε is the electric permittivity, ΔE is the exciton binding energy, kT is the thermal energy potential, F is the electric field. k_{SEP0} represents the charge transfer exciton separation rate at zero electric field.

Because k_{SEP0} is primarily dependent on the mobility, we assumed k_{SEP0} almost constant. Its value obtained for all the CCSs at different currents is k_{SEP0} = 9.9±2.5·10^3 s^{-1} calculated with *a*=1 nm and ε=3ε$_0$. Instead, Fig. 2.3.12 shows the evolution of k_{REC}, i.e the polaron recombination rate, which increases by increasing stress time in most of the samples. In some cases, such as during the CCS at 150 mA/cm^2 under illumination, k_{REC} start decreasing after 10000 seconds, i.e., the same time when the short circuit current saturates to the minimum value and the efficiency starts experiencing a partial recovery. Tentatively, we may ascribe the decrease of the recombination rate with the annealing of some morphological defects responsible for the exciton quenching, due to the high temperature reached during stress.

Again, this confirms that the recombination rate severely affects the cells performances, and it is one of the dominant effects driving the variation of the short circuit current and the cell efficiency, as well.

2.3.4 Summary

We showed that the polaron recombination rate is one of the major reasons for the cell degradation during constant current stress in forward bias condition. Besides, our data and the model show that a correlation exists between the band bending at the interfaces and the photocurrent, and these bending contribute to cell performances together with the polaron recombination rate.

Even though the applied model is very simple and qualitative, it is still suitable for finding a relation between the cell degradation and the variation of some parameters, such as the exciton separation probability or the contact barrier heights. Of course, some limits still exist. For instance, it is possible to extract the cumulative effects of the barrier height at the contacts, but it is not possible to distinguish and separate the contribution of the single barrier. For sure, the development of a more quantitative and complete model is worthy for a more detailed and accurate analysis, for quantifying better the role of interface degradation and the mechanisms behind the photocurrent generation.

3 Perovskite Solar Cells

The word perovskite indicates a group of minerals having similar orthorhombic structure and properties such as piezoelectricity, magneto-resistance or superconductivity. $CaTiO_3$ was the first mineral called "perovskite" by Gustav Rose in 1840 and the name "perovskite" was assigned to honor the mineralogist Lev Aleksevich von Petrovski, Minister of the Internal Affairs under Nicolas I of Russia. Fig. 3.0.1 shows how $CaTiO_3$ perovskite appears as a mineral in nature. Afterward, the term perovskite indicated all those structures having the general formula ABX_3, where A and B are metallic cations of big and small radius respectively, while X is an anion.

Perovskite can be synthesized or natural, fully inorganic or hybrid organic-inorganic. However, for photovoltaic applications, the hybrid organic-inorganic $CH_3NH_3PbX_3$ (where X is Cl, Br, I or a combination of them) proved to be one of the most efficient perovskite materials for solar cells. Fig. 3.0.2 shows the structure assumed by methyl-ammonium lead-iodide in cubic shape. Organometal hybrid perovskite materials have gained huge visibility since the first application of halide perovskite as dye-sensitizer material in hybrid Dye-Sensitized Solar Cells (DSSCs) [87]. Encouraged by the promising optical and electrical properties of these materials, many researchers focused their efforts on improving the performances of solar cells based on organometal hybrid perovskites, called perovskite solar cells (PSCs). Their performance quickly raised from the initial 3.8% efficiency to the highest so far record of 22.1% [5] and efforts are continuously being invested to bring the efficiency close to its theoretical ~31% limit [88]. Furthermore, perovskites have gathered increasing interest on several fields because of the tunable properties [89–91] and the fact that these materials are suitable for low-cost roll-to-roll industrial processes [92–96] since they use inexpensive precursors and low processing temperatures whether compared to traditional inorganic semiconductors. Thus, besides photovoltaic devices, perovskites have been investigated also for other applications such as photo-detectors [97], thin film transistors (TFTs) [98], optically and electrically pumped LASER [99–104] and LEDs [105,106].

Despite PSCs have recently made important progresses in terms of device efficiency, the reported interesting figures still belong to devices electrically unstable, as noted in the NRL efficiency chart of Fig. 1.1.1[17]. These devices exhibit several weaknesses mostly related to their hybrid organic nature [19–21,25,107–111]. Moisture is one of the major issues [108,109] because interaction with water molecules generates an irreversible hydrolysis process that decomposes the perovskite layer. The moisture induced degradation has been documented with humidity levels as low as 55% [112–114] and it negatively affects the device performances, besides it is paired with a visible shift from dark black to yellow of the perovskite color [9,115]. Furthermore, the presence of a UV component in the illumination spectrum assists water hydrolysis by exploiting the TiO_2 as an efficient photo-catalyst [116], in a way similar to what observed in dye-sensitized solar cells (DSSC) [11]. Temperature affects PSCs and despite an initial annealing improves the device performances by increasing the film quality, the exposure of the cell to relatively high temperature for longer times could be detrimental [108]. Furthermore, perovskites exhibit a hysteretic behavior, emphasized by the adoption of planar configurations [117]. While in some applications long persistence phenomena are desirable [118], in photovoltaic devices the hysteresis is detrimental since it negatively impacts on the device maximum power point extraction, affecting the correct efficiency estimation [25,119]. Upon polarization and illumination, slow transients and hysteretic effects have been reported with a variety of dynamics, which differ in magnitude and time scale, depending both on the material processing and on the specific device architecture [120–122]. Several works [119,123–126] agreed on explaining such hysteretic phenomena by means of ions moving within the perovskite layer. However, other studies [127–131] concluded that the perovskite

behaves as a ferroelectric material to some extent. At the time of writing, it is well accepted that ionic motion is the dominant contribution to hysteresis within perovskite thin films [122,126,132] and several experimental evidences support a defect-assisted phenomenon [133–135]. Moreover, interface effects at the selective contact/perovskite interfaces have been identified and related to ionic and electronic defects [136–140]. Regarding the latter, it is usually reported that using fullerene related materials, as electron transport layer (ETL) [141–144] reduces the electrical instability since it passivizes the defects enhancing charge extraction.

In conclusion, further research and solutions are required to make perovskite-based devices ready to enter the market.

Fig. 3.0.1 Perovskite $CaTiO_3$ as usually found in nature.

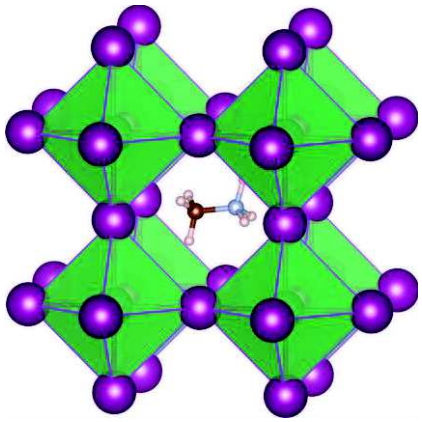

Fig. 3.0.2 Methyl-ammonium lead-iodide perovskite structure, CH_3NH_3 is the organic cation within the tetragonal PbI.

3.1 Suppression of ionic motions in perovskite thin film for optoelectronic applications

3.1.1 Introduction

Perovskite materials obtained with lead iodide nanocrystals (NCs) synthesized by laser ablation in benzene derivative, suggested that the ionic motion can be hindered also upon prolonged bias application [145]. New data on perovskite obtained from PbI_2 ablated in iodobenzene and in a non π-conjugated solvent like isopropyl alcohol are presented in the following section. In particular, the solvent decomposition processes, during laser ablation, produce a graphitic interface intimately bound to lead iodide nanocrystals, which have an active role in the perovskite thin film electrical behavior. Among the techniques used for the characterization of the synthesized materials, electron paramagnetic resonance experiments showed a completely different behavior of the perovskite obtained with PbI_2 synthesized under different solvents. Measurements in dark and light on lateral and vertical configuration allowed deducing a model for the electrical behavior of these materials. The results confirm the role of the graphitic component of the hybrid precursor in the suppression of the ionic motion, which can be connected with the transfer of charges and the passivation of the defect states of the perovskite.

3.1.2 Methods

All reagents used are from Sigma-Aldrich if not differently reported.

3.1.2.1 NC colloidal ink production

Lead iodide nanocrystals were produced by laser ablation in solution (LASiS). The second harmonic of a Nd:YAG laser (Quantel), at 532 nm, 9 ns and 10 Hz, was focused, with a fluence of 3 Jcm^{-2}, on the surface of a PbI_2 compressed powder tablet . The tablet was placed in a vial under iodo-benzene (IodoB) and isopropyl-alcohol (IPA) for obtaining PbI_2-IodoB-NC and PbI_2-IPA-NC, respectively. An optimized 2h synthesis produces 0.065 mg/mL of PbI_2-iodoB-NC and 0.39 mg/mL of PbI_2-IPA-NC in colloidal solutions. The method for the estimation of the colloidal concentration was already reported [145].

3.1.2.2 Thin film deposition

Nanocrystals thin films were produced by spray coating diluted isopropanol solutions on different substrates (Si, glass or FTO). C-PVK (perovskite obtained from PbI_2-IodoB-NC precursor) and PVK (perovskite obtained from PbI_2-IPA-NC precursor) samples were prepared following an optimized 2-step procedure. First, an approximately 200 nm thin film was prepared using the colloidal solutions. The colloidal solution of PbI_2-iodoB-NC in IPA was obtained by the centrifugation of the colloidal solution in iodo-benzene, the elimination of the surnatant and the dissolution of the nanocrystals in IPA. The prepared thin films were then immersed in a methyl-ammonium (MAI, DYESOL, Italy) anhydrous isopropanol solution (10 mg/mL) under gentle stirring for 2 minutes in order to obtain the conversion to perovskite. Then, the films were dipped into fresh anhydrous IPA twice and finally rinsed with dichloromethane. The solution processed 200 nm PbI_2 thin film, for obtaining SP-PVK, was prepared following literature [146].

3.1.2.3 C-PVK and PVK thin films

Two perovskite thin films were prepared on Au interdigitated chips by spray coating the two solutions of the precursors PbI_2-IodoB-NCs or PbI_2-IPA-NCs on the chip followed by a quick dip coating into a concentrated MAI IPA solution (30 s). A sequential dry step in clean anhydrous IPA and in chloromethane allowed obtaining C-PVK and PVK samples. Perovskite film thickness was measured to be about 250 nm with an optical profilometer.

3.1.2.4 X-Ray analysis

The X-ray diffraction spectra were recorded with a BRUKER D8 ADVANCE diffractometer with Bragg–Brentano geometry and equipped with a Cu Kα1 (λ = 1.544060 Å) anode at operating voltage of 40 kV and operating current of 40 mA. All the diffraction patterns were recorded at room temperature over an angular range (2θ) between 10° and 60°, at step size of 0.020°, and an acquisition time of 1 s. Step size was used as error source for experimental data.

3.1.2.5 HR-TEM and SEM analysis

The high resolution TEM images were acquired on a high resolution JEOL 2100F TEM, working at 200 kV. Samples for TEM were prepared with 2μL of solution, dispersed in isopropanol, deposited on a lacey carbon film TEM grid (Quantifoil) and left to dry for two hours before its introduction into the TEM. The measurements were performed on nanoparticles stuck to the carbon laterals to avoid the contrast of the amorphous carbon film. SEM images were acquired with a Zeiss SUPRA40 Field Emission SEM.

3.1.2.6 Raman and UV-Vis-NIR measurements

Raman spectra were recorded with an inVia Renishaw μRaman instrument. The laser line at 633 nm of a He-Ne laser was used for excitation. A 20x objective was used to focalize the laser beam. A Cary 5000 instrument of Agilent was used for recording the UV-Vis-NIR spectrum.

3.1.2.7 EPR analysis

EPR measurements were performed on a Bruker ELEXSYS E580 spectrometer at X-band (9-10 GHz). The sample temperature was controlled by a N_2 cooling systems. Illumination of the sample was performed either with a white light excitation by a Xe lamp (300W , LOT Quantum Design, λ=300-900nm, about 50mW/cm^2 on the sample) or with a narrow-bandwidth excitation using a monochromator (about 0.5mW/cm^2 and 10nm bandwidth). To achieve a higher light irradiance, light-induced EPR spectra have also been recorded by illuminating the samples with nanoseconds laser pulses (second harmonic of a Nd:YAG, 532nm, 5 ns/pulse, 5mJ/pulse cm^2). The C-PVK sample was obtained as follows: 66 μL of a 20 mM MAI IPA solution were added into a 3.5 mM PbI_2-IodoB-NCs in iodobenzene, obtaining a MAI 5 mM final concentration. After a gentle sonication for 10', the black dispersion was centrifuged and recovered in toluene for EPR analysis. For preparing PVK sample, the reaction occurred in IPA solution, simply adding an excess of 10x of MAI. Also in this case, after a gentle sonication for 10', the black dispersion was centrifuged and recovered in toluene for the EPR analysis. A reference sample with pyrolysis of the iodobenzene ("IodoB") was produced by direct ablation of the solvent for 20' at the same conditions of PbI_2-iodoB-NCs. The resulting black powder precipitate was centrifuged and re-dispersed in toluene for EPR analysis. The dispersion was then inserted into a quartz tubes for EPR measurements; removal of the solvent and of atmospheric oxygen was obtained by vacuum pumping (P<10-3 mmHg) followed by sealing under vacuum of the tubes.

3.1.2.8 Electrical characterization

1 Sun equivalent power light was used for illumination, using a white led. Two sample structures were realized for the experiments: a planar structure with inter-digitated gold fingers at 20 μm distance (ID); a Metal/insulator (or semiconductor)/Metal (MIM) vertical structure (about 200 nm) with asymmetric electrodes. The ID structure was realized on a silicon substrate, passivized by silicon dioxide, with gold fingers as electrodes. The MIM structure was an FTO/PVK/Carbon-Tape structure. A top copper foil was used above the carbon-tape to reduce series resistance of the contact. The electrical characterization was performed by means of current-voltage scans both in dark and under illumination. All the measurements were done inside a custom-made glove box filled with nitrogen to avoid air and moisture degradation of the samples. The voltage applied ranges from -10V to 10V with planar devices (ID) while from -3V to 3V on vertical structures (MIM). The scan rates (SR) used are 5V/s (fast scan) and 300 μV/s (DC steady state scan). We used the Agilent B1500 parameter analyzer to perform the characterization as we monitored both the electrodes and the gate (only in planar structures) during the measurements to keep under control any leakage occurring due to the setup or substrates. The different measurements have the following scan setting (if not otherwise stated): i) "No Bias": the device is in short circuit condition at 0V for 600 s (ID) or 100 s (MIM) before scanning forward/reverse. The resulting curve is the merge of the two scans. SR = 5V/s; ii) "Positive (Negative) Bias": the device is biased at the maximum forward (reverse) bias for 600 s (ID) or 100 s (MIM) before scanning from forward (reverse) to reverse (forward) and

backward. SR = 5V/s. iii) “Steady State”: the device is scanned from forward to reverse and backward after a pre-bias of 600 s (ID) or 100 s (MIM). The scan rate applied is SR = 300 μV/s, thus we assume the resulting measure being the real DC steady state of the device. Due to the very long time of the measurement (up to 36h), the forward and backward scan could not overlap each other mainly due to induced degradation in the device. We characterized the devices using “No Bias” and “Positive (Negative) Bias” both in dark and under illumination, while we measured the devices with the “Steady State” characterization only in dark to avoid an excessive degradation due to light exposure. A custom white LED provides the illumination that is constant for all the devices under test. The temperature was maintained constant in ID samples at 25 °C through a Peltier cell in contact with the bottom of the device.

3.1.2.9 KPM analysis

The samples with solutions of PbI_2-NCs suspended in different solvents (IPA and iodobenzene) drop-cast on silicon substrates have been characterized by atomic force microscopy (AFM) and Scanning Kelvin probe microscopy (SKPM). The measurements were done simultaneously for both channels in the same image area by means of an MFP-3D instrument (Asylum Research, CA, USA). A MESP probe (Bruker, CA, USA), with resonant frequency of 75 kHz and tip diameter of 70 nm after the 25 nm coating of CoCr providing the required electrical conductivity. The set elevation height for the second pass – during which the surface potential is measured – was 50 nm. Touching of the tip during the lowest part of its oscillation was prevented as proper feedback tuning cancelled out most oscillation during the second pass, and the height of the center (rest) position of the tip during the second pass was as high as the set point amplitude used during the first (topographic) pass, which we estimated to be 70 nm. The used tip was calibrated, preliminary to the measurements versus freshly exfoliated HOPG, which was assumed to hold the work function level of 4.65 eV. Thus, the apparent tip work function was in our case 4.93 eV.

3.1.3 Results and discussions

Lead iodide nanocrystals were produced by nanosecond pulsed laser ablation (laser ablation in solution, LASiS) [147] at 532 nm of a target of PbI_2 following the published recipe [145]. Briefly, a disk of 10 mm diameter and 2 mm tick of compressed powder of PbI_2 was placed at the bottom of a vial with 4 mL of iodo-benzene or isopropanol and nanosecond laser pulses (10 Hz) were focalized on the target (3 Jcm^{-2}) obtaining a colloidal solution of PbI_2-IodoB-NC or PbI_2-IPA-NC, respectively. Ablation time was optimized for obtaining stable colloidal inks with different concentrations (see 3.1.2 methods) without using any stabilizing molecule. UV-Vis-NIR spectra, X-ray and FE-SEM characterizations of the NC are provided in Fig. 3.1.1. The UV-Vis-NIR spectra reported in Fig. 3.1.1a show, for both samples, low scattering in the NIR region, suggesting small dimensions of the crystals. The optical edge for PbI_2 can be seen at 515 nm (2.4 eV), in agreement with literature [148]. The lower optical density at the absorption edge of PbI_2-iodoB-NC with respect to PbI_2-IPA-NC derives from the different production yield in the two solvents. Fig. 3.1.1b shows the XRD analysis of thin films obtained by spraying the colloidal inks on silicon and, for comparison, a typical solution-processed PbI_2 thin film. The peak at 12.6°, related to the (110) plane of PbI_2 is present in all samples. By fitting this peak with a Lorentzian curve, we can estimate the minimum crystallite size for the samples exploiting the conventional Scherrer equation [149], obtaining for PbI_2-IPA-NC 15 nm, for PbI_2-IPA-NC 19 nm, and for solution-processed PbI_2 22 nm.

An experimental confirmation is provided by SEM images. In particular, the FE-SEM images of drop casted colloidal solutions in Fig. 3.1.1c-d present a size distribution in the range of 10-100 nm for laser ablated samples. With these NC one can produce highly packed thin film morphologies, (see Fig. 3.1.2), in which a 200 nm thick film, obtained by spray-coating the colloidal solution of PbI_2-IodoB-NC, is reported. Low-atomic weight material is present around the nanoparticles, (see Fig. 3.1.2b), which likely corresponds to carbon compounds as evidenced by an EDX analysis (see Tab. 3.1-A) for both PbI_2-IPA-NC and PbI_2-IPA-NC samples.

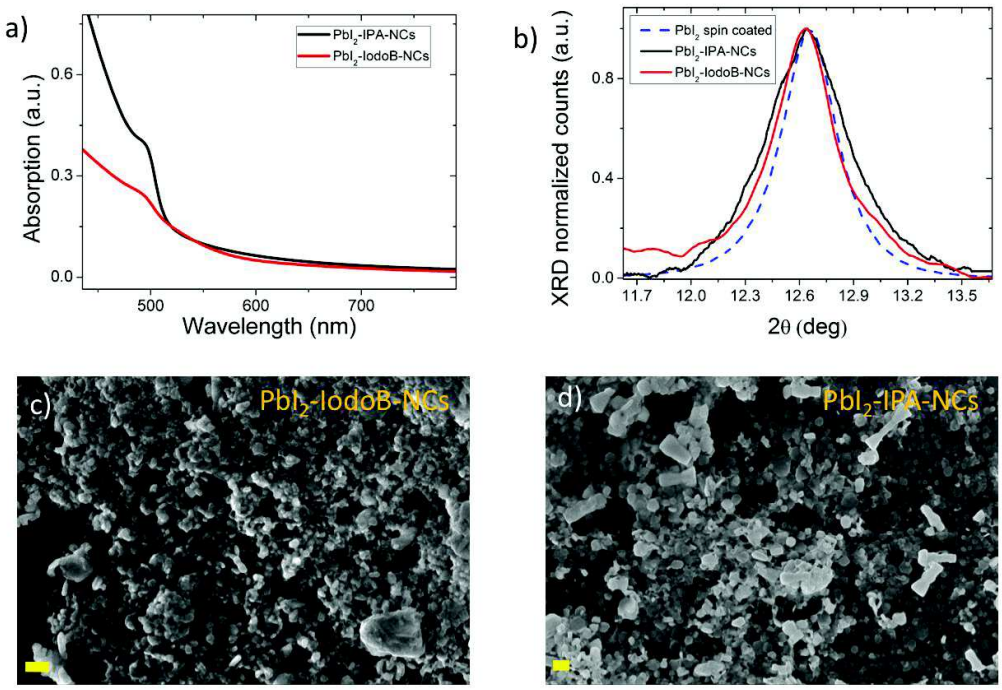

Fig. 3.1.1 a) UV-Vis spectra of PbI_2-IPA-NCs and PbI_2-IodoB-NCs solutions; b) XRD pattern showing (110) plane of PbI_2 for different samples; c) and d) show SEM images of drop casted PbI_2-IodoB-NC and PbI_2-IPA-NC, respectively (scale bar 100 nm).

a) PbI_2-IPA-NCs						
Element	Line Type	Apparent Concentration	k Ratio	**Wt%**	Wt% Sigma	**Atomic %**
C	K series	0.19	0.00192	**5.19**	0.28	**31.58**
O	K series	0.40	0.00134	**3.00**	0.18	**13.69**
Si	K series	0.53	0.00417	**5.49**	0.14	**14.30**
I	L series	2.87	0.02872	**44.53**	0.61	**25.67**
Pb	M series	2.73	0.02545	**41.80**	0.62	**14.76**
Total:				**100.00**		**100.00**
b) for PbI_2-IodoB-NCs						
Element	Line Type	Apparent Concentration	k Ratio	**Wt%**	Wt% Sigma	**Atomic %**
C	K series	0.23	0.00227	**6.53**	0.36	**33.80**
O	K series	0.44	0.00147	**3.30**	0.23	**12.81**
Si	K series	0.89	0.00705	**9.43**	0.22	**20.87**
I	L series	2.76	0.02756	**43.79**	0.72	**21.44**
Pb	M series	2.34	0.02180	**36.95**	0.75	**11.08**
Total:				**100.00**		**100.00**

Tab. 3.1-A a) EDX report for PbI_2-IPA-NCs. b) EDX report for PbI_2-IodoB-NCs. EDX data confirm the nominal stoichiometry of the PbI_2 for both cases and shows a carbon content of about 30% in atomic percentage, which is above a possible environmental contamination.

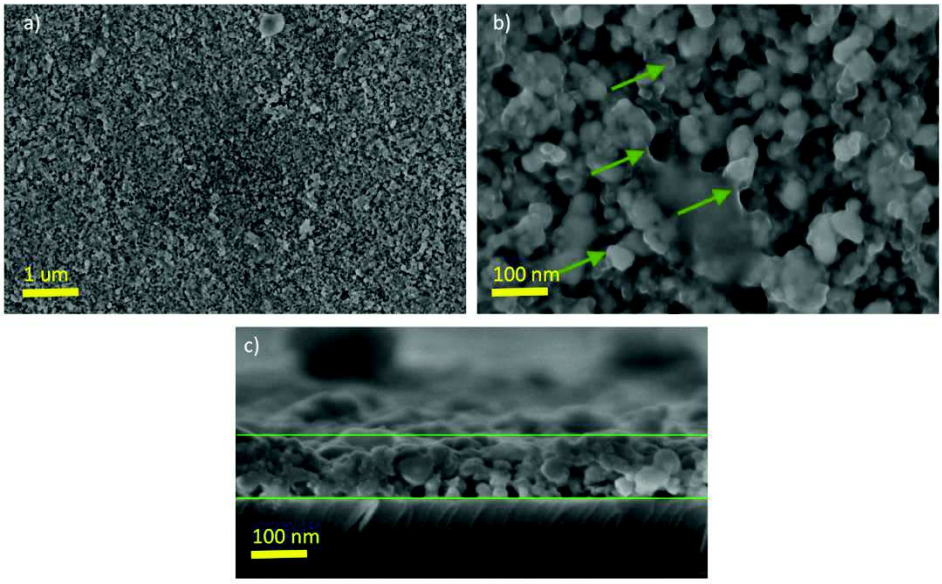

Fig. 3.1.2 SEM analysis of PbI_2-IodoB-NCs-based thin film. a) and b) top view image at different magnifications, c) cross section image. Green arrows highlight light areas where low weight-material is well-contrasted with respect to the darker neighboring particles.

In order to provide a detailed description of the microscopic composition of these particles, Raman and TEM analyses were performed (Fig. 3.1.3). Raman spectra (Fig. 3.1.3a) show narrow bands, suggesting crystalline material. The D-band at 1340 cm^{-1} and G-band at 1600 cm^{-1} show the presence of graphitic like structures [150]. Moreover, the Raman peaks at 1530 cm^{-1} can be assigned to little graphene domains like graphene nanoribbons (GNRs) [151].

The Raman spectra show that in the sample are also present saturated hydrocarbon chains because of the presence of typical peaks at 2900 cm^{-1} for the -CH_2/-CH_3 stretching, at 1450 cm^{-1} for -CH_3/-CH_2 bending and at 1300 cm^{-1} for -CH_2 twist. By performing laser ablation of the IodiB solvent only, the precipitate (blue dash curve) shows the spectrum characteristic of amorphous carbon (IodoB-NC), namely very large bands around 1600 and 1340 cm^{-1} and no bands in the

3000 cm^{-1} spectral region. One deduces that the presence of PbI_2 in the plume (during the ablation) catalyzes the formation of nanocarbon crystalline structures and saturated hydrocarbon chains.

One also observes, in Fig. 3.1.3a, that the content of graphitic structures is large for PbI_2-iodoB-NC, whereas much less graphitic material is present for PbI_2-IPA-NC. In order to confirm this observation, HR-TEM images were recorded.

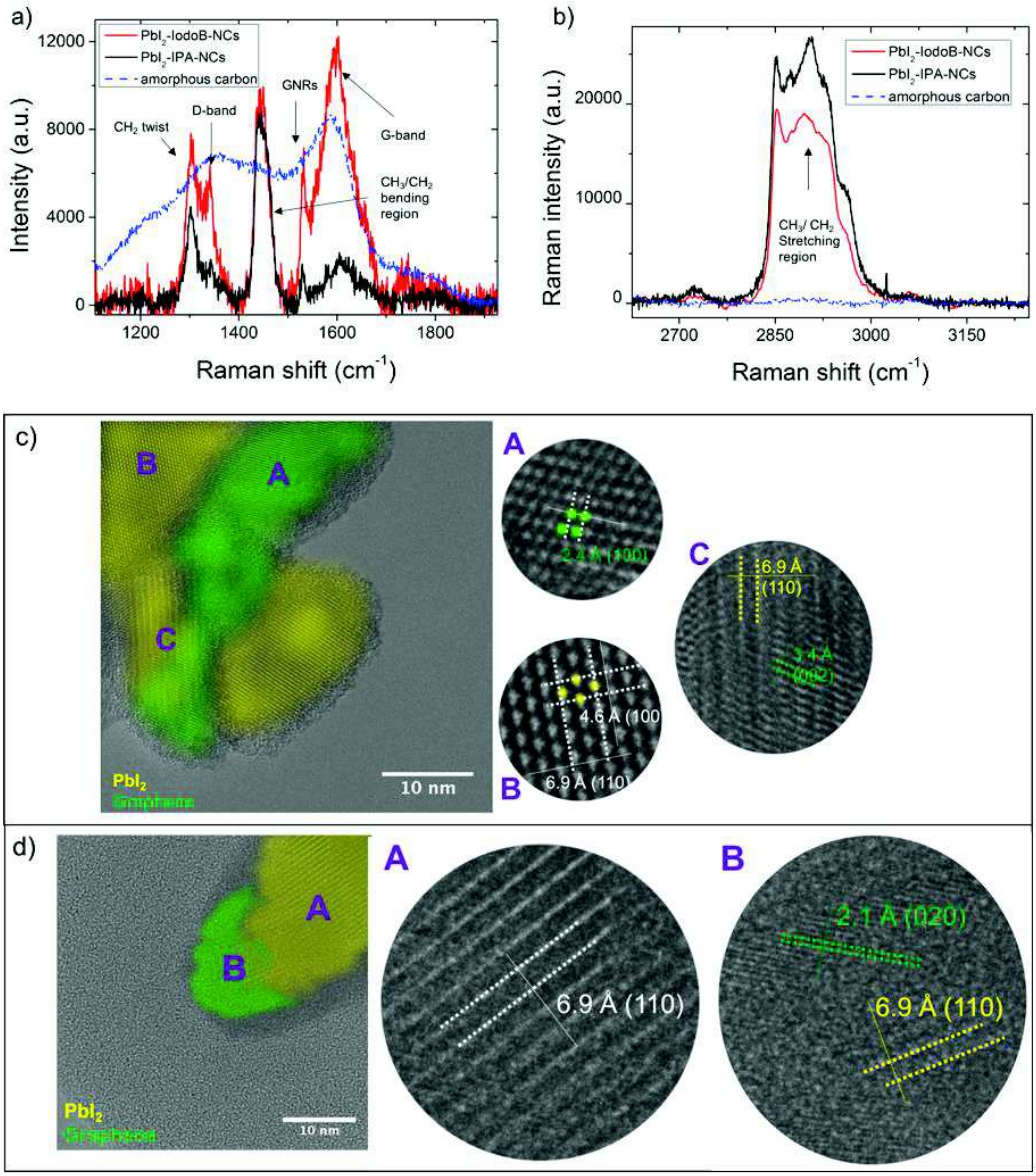

Fig. 3.1.3 Raman and TEM characterization of the produced NC. a)-b) Raman spectra excited at 633 nm of PbI_2-iodoB-NC (red line), of PbI_2-IPA-NC (black line) and of amorphous carbon (blue dashed line); HR-TEM characterization of c) PbI_2-iodoB-NC and d) PbI_2-IPA-NC, respectively. The zoomed areas correspond to different regions highlighting crystalline lattices for PbI_2 (in yellow) and graphene (in green).

In Fig. 3.1.3c-d HR-TEM images of the NC are presented. The image in Fig. 3.1.3c confirms that PbI_2-iodoB-NC is a hybrid material. Different areas of a nanocrystal are highlighted in the image. Green areas (A) are consistent with graphitic materials (here the rhombohedral packing is highlighted with (100) and (002) planes of a typical AB stacking [152]), whereas yellow areas can be recognized as a lead iodide crystal (B) since 4.6 Å and 6.9 Å are consistent with the lattice constant of a unstrained rhombohedral lead iodide [153]. The hybrid nature of the material is also well displayed in area "C" in which a dislocation is found along the (110) plane of PbI_2 revealing the intimate contact of the lead iodide

phase with the graphitic one (for instance (002) plane of graphene is shown). In addition, there are amorphous areas (light grey areas) surrounding particles, which can be correlated to the presence of the saturated hydrocarbon chains found in the Raman spectra. Although TEM imaging cannot give a tridimensional picture of the surface, the presence of unstrained PbI_2 suggests that the graphitic material is at the interface between lead iodide nanocrystals. TEM images of PbI_2-IPA-NC show much less graphitic material, as already expected from the Raman measurements. Fig. 3.1.3d shows, however, that some graphitic material is present ((020) plane of AA' stacking [152] for graphene (zoom B)), together with PbI_2 (zoom A). Amorphous areas are evident also in this case (dark grey areas) and can be related to the presence of the saturated hydrocarbon chains observed in the Raman spectrum.

More insight into the electronic interaction of the carbon materials present on PbI_2-IodoB-NC, PbI_2-IPA-NC and on the derived perovskite nanomaterials, was obtained by performing Electron Paramagnetic Resonance (EPR) spectroscopy. EPR is a high-sensitive technique able to get information on the presence of unpaired electrons, and it is useful to validate hole/electron transfer mechanisms in semiconductors [154]. The EPR signals are related to the amount and nature of the paramagnetic species present in the sample. As reported in Fig. 3.1.4a-B, an EPR signal is observed in dark for PbI_2-IodoB-NC. On the contrary, no EPR signals can be detected for PbI_2-IPA-NC (Fig. 3.1.4a-A). The comparison shows that the EPR spectrum cannot be due to the presence of Pb. The observed EPR signal shows a slightly asymmetric line-shape and a resonance field, which corresponds to a g-factor (a parameter proportional to the magnetic moment of the unpaired electron) of g=2.0030.

The deconvolution of the EPR line can be satisfactorily achieved using two Lorentzian line-shapes as shown in Fig. 3.1.4b (fitting parameters reported in Tab. 3.1-B), suggesting the presence of at least two paramagnetic species with very close resonant fields (g-factors), but with different line-widths. The EPR spectrum of the amorphous carbon, obtained by ablation of pure iodobenzene (IodoB, Fig. 3.1.4c)**,** is significantly different from the spectrum of PbI_2-IodoB-NC. The main difference is in the relative contribution of the broad line, which amounts to 80% for iodoB-NC and only 50% for PbI_2-iodoB-NC (Tab. 3.1-B).

Sample	Lorentzian component	Center (G, ± 0.3)	g-factor * (±0.0002)	Linewidth (G, ± 0.2)	Relative Weight (± 5%)
PbI_2-IodoB-NC	Broad line	3427.7	2.0039	6.5	50%
	Narrow line	3429.2	2.0030	2.8	50%
IodoB	Broad line	3427.9	2.0038	15.5	80%
	Narrow line	3429.2	2.0030	4.1	20%

Tab. 3.1-B Best-fit parameters for the Lorentzian deconvolution of the EPR spectra in Fig. 3.1.6.

**The g factor is calculated by the resonance relation: $= \frac{\mu_B B_{res}}{h\nu}$, where B_{res} is the center of the resonance line, μ_B is the Bohr magneton, h is the Planck constant and ν is the microwave frequency of the spectrometer.*

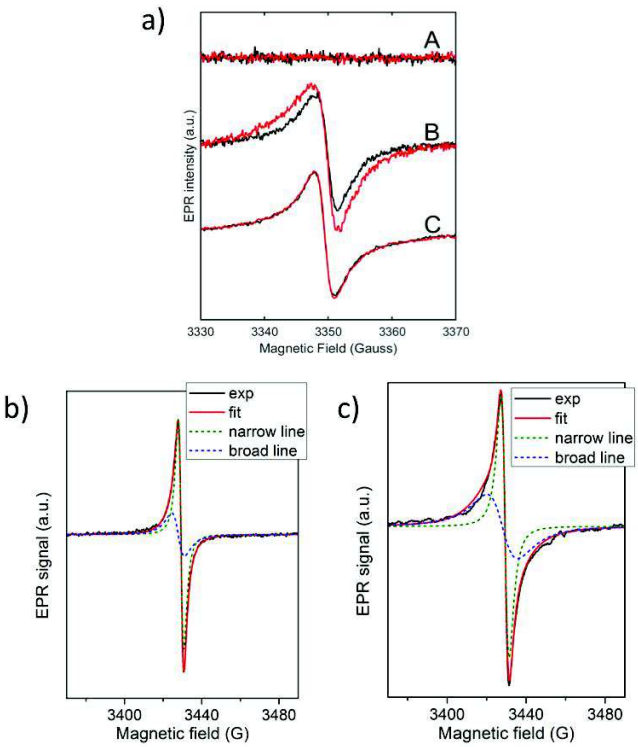

Fig. 3.1.4 a) EPR spectra in dark (black lines) and in light (red lines) for: A) PbI_2-IPA-NC, B) PbI_2-IodoB-NC, C) IodoB; Deconvolution with two Lorentzian lines (in first derivative mode) of the experimental EPR spectra of the b) PbI_2-IodoB-NC and c) IodoB samples. Black lines: experimental EPR spectra. Red Lines: best fit of the experimental spectra, obtained as sum of two Lorentzian peaks. The best fit parameters of the Lorentzian components are reported in Tab. 3.1-B.

The two Lorentzian contributions to the EPR spectra of PbI_2-IodoB-NC show g-factors and linewidths analogous to those previously attributed to different types of paramagnetic species found in nanographite samples [155,156]. This agrees with the presence of graphitic-like structures in carbon materials produced by laser ablation [147], which often include paramagnetic species and defects that can be detected by EPR [157]. The absence of any EPR signal in PbI_2-IPA-NC is explained by the very low fraction of graphitic phases in this material.

The different intensities of the two components of the EPR line of PbI_2-IodoB-NC, compared to that of iodoB sample (the amorphous carbon), suggests the presence of a charge transfer interaction in PbI_2-IodoB-NC between the graphitic carbon and the PbI_2 nanocrystals also in dark, since the EPR line-shapes depends on the nature of the spins. Although further studies are needed for species assignment, their variation can be used as a proof of the interaction between the materials. This interaction is expected to produce more effect under illumination. Fig. 3.1.4 reports the EPR spectra under illumination (red lines). It is possible to observe an increase of the EPR signal of PbI_2-IodoB-NC irradiated with visible white light. This not occurs for the IodoB sample, confirming the presence of a charge transfer between the graphite and the PbI_2 nanocrystals. Furthermore, no EPR signal is observed, also under illumination, for PbI_2-IPA-NC. These results demonstrate that the graphitic phase of the hybrid materials, present in PbI_2-iodoB-NC and almost absent in PbI_2-IPA-NC, is able to exchange spins (i.e. charges, such as electron or holes) with PbI_2 nanocrystals.

Photo-generated EPR spectra of PbI_2-IodoB-NC with different excitation wavelengths (from 450 up to 850nm) are reported in Fig. 3.1.5, where only the differences between the light-on and the dark spectra are shown**.** One can observe that the light-induced EPR signal can be detected up to the excitation wavelength of 850 nm, therefore at photon energies well below the PbI_2 absorption edge at 525 nm. This shows that also a direct excitation of the graphitic material, which absorbs in this spectral region, induces a spin (charge) transfer to the PbI_2. This is a further confirmation of the active contact between the graphitic part and the lead iodide core of the hybrid nanocrystals.

PbI_2-IodoB-NC and PbI_2-IPA-NC were converted to perovskite (in the following we will use C-PVK for the perovskite from PbI_2-IodoB-NC and PVK for that obtained from PbI_2-IPA-NC), by using a MAI solution (see 3.1.2 methods). The same EPR behavior of the precursors was observed also for C-PVK and PVK, namely, EPR signals were observed only in C-PVK **(**Fig. 3.1.6**)** and under illumination only C-PVK shows an increase of EPR intensity. One should recall that the presence of a charge transfer between the graphitic carbon and the perovskite nanocrystals was also suggested by calculations [158]. The absence of EPR signals for PVK also after illumination shows that the graphitic phase present in this material is not sufficient to produce an EPR signal, as it was also observed in the precursor PbI_2-IPA-NC.

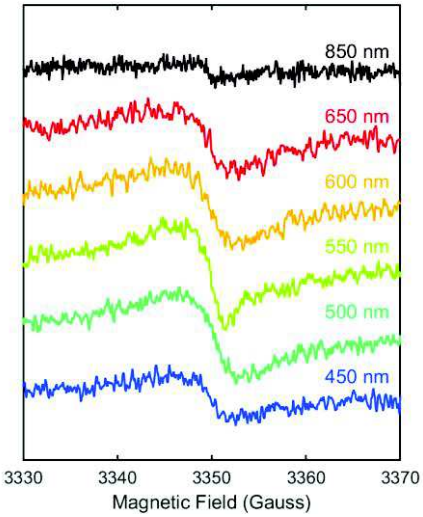

Fig. 3.1.5 Light-induced EPR spectra excited at different wavelength (difference between light on and dark signals) for PbI_2-IodoB-NCs.

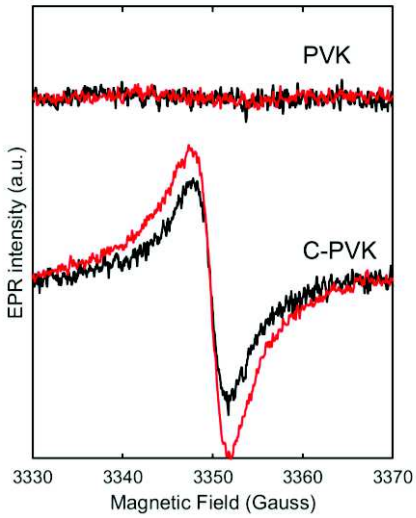

Fig. 3.1.6 EPR spectra in dark (black lines) and under illumination (red lines) of the two perovskite PVK (obtained from PbI_2-IPA-NC) and C-PVK (obtained from PbI_2-IodoB-NC). The spectra are almost coincident with those recorded on the precursor, indicating that the conversion to perovskite does not affect the nature and number of paramagnetic defects in the carbon NC.

The existence, in dark, of a charge exchange mechanism involving the graphitic material can be further supported by the analysis of the work function of the prepared materials with Scanning Kelvin Probe Microscopy (SKPM). Atomic Force Microscopy (AFM) and SKPM measurements (see Fig. 3.1.7) for PbI_2-IPA-NC and PbI_2-IodoB-NC show that only for the latter a substantial KPM signal contrast between grain boundaries and bulk particles can be seen. This shows the presence of a different material at grain boundaries, which the Raman, TEM and EPR characterizations suggest being the graphitic material. A SKPM line profile (see Fig. 3.1.7) shows a difference in work functions of PbI_2 and graphitic materials of about 25 mV, confirming literature values for bulk PbI_2 (4.6 eV) [148,159] and graphitic species (4.3-4.9 eV) [160,161]. These measurements support the conclusion that an exchange mechanism of charges between the two phases present in PbI_2-iodoB-NC is possible also in dark and that, therefore, this is also possible for C-PVK.

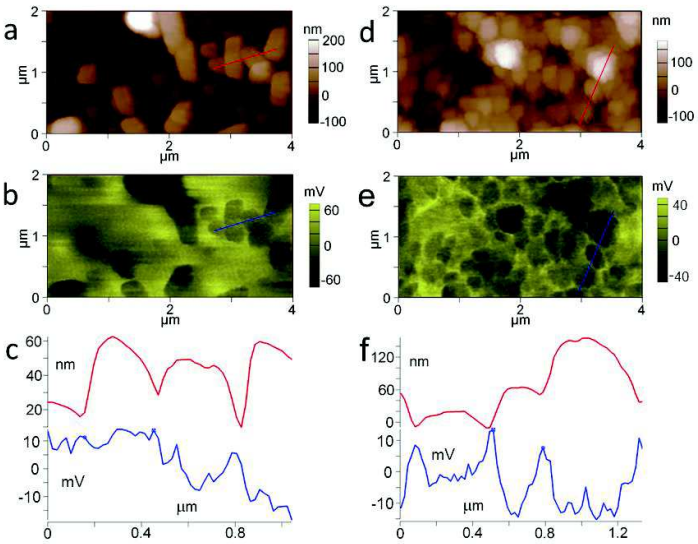

Fig. 3.1.7 SPM characterizations of NCs. AFM and KPM images related to PbI_2-IPA-NCs (a-b) and related to PbI_2-IodoB-NCs (d-e); Line profiles (red curve, AFM; blue line, KPM) for c) PbI_2-IPA-NCs and f) PbI_2-IodoB-NCs.

Perovskite thin films, obtained from PbI_2-NC colloidal inks, were realized by spray coating (see 3.1.2 methods) obtaining PVK and C-PVK thin films on different substrates. FE-SEM images and XRD patterns for both films show a good uniformity of the thick films (up to one micron), and the usual tetragonal lattice for both samples (see Fig. 3.1.8 and Fig. 3.1.9). The parameters of the crystallographic cell, deduced from the XRD pattern, show that C-PVK and PVK do not present any stress due for example to inclusion of carbon materials inside the crystals, confirming the SKPM data that this material is present only on grain borders.

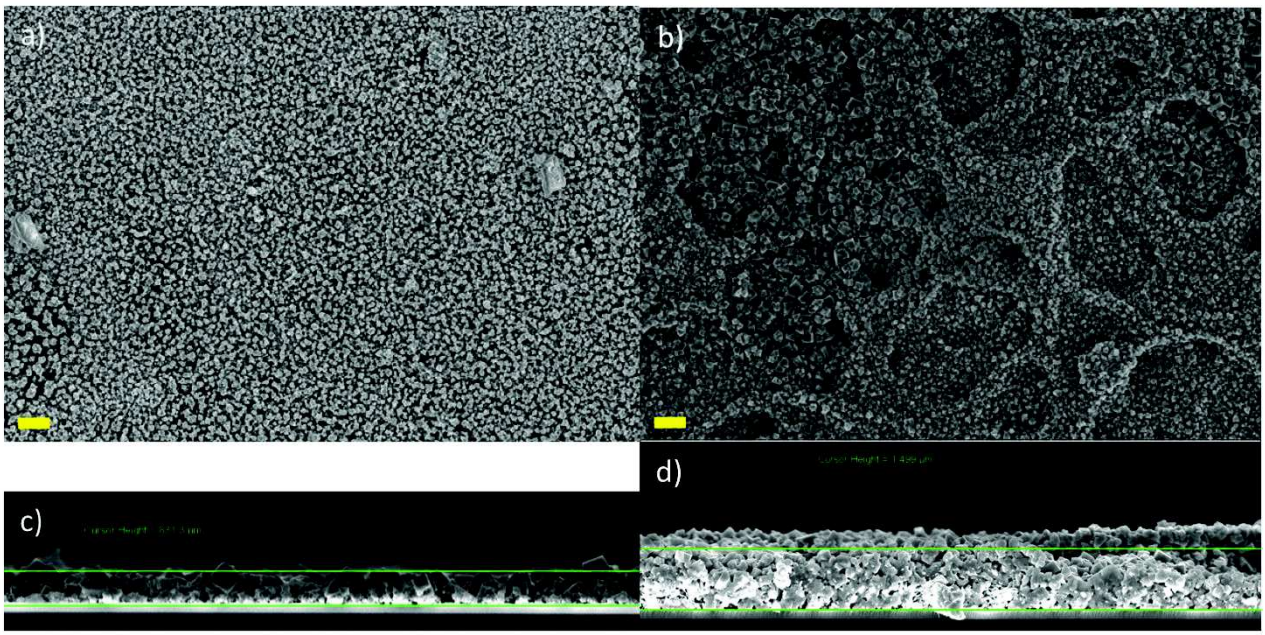

Fig. 3.1.8 SEM images of C-PVK and PVK thin films samples on Si substrate for I-V measurements. C-PVK top view a) and cross section images c); PVK top view b) and cross section d). Scale bar is 1 um. C-PVK surface (a) is more uniform than PVK (b), revealing crystals up to 300 nm in size. EDX data confirm stoichiometry of converted perovskite. Cross section images c-d highlights good uniformity in film thickness.

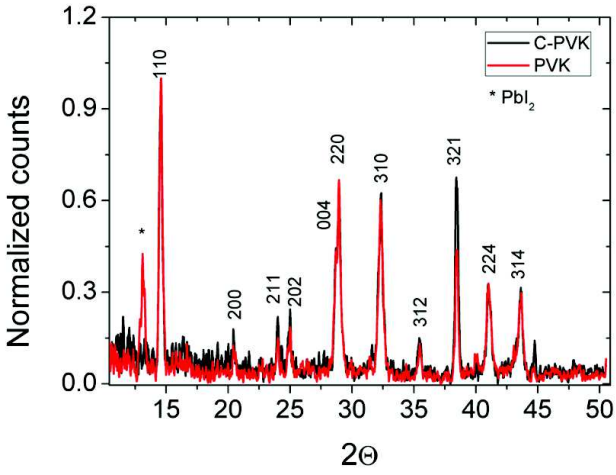

Fig. 3.1.9 XRD patterns for C-PVK and PVK thin films. Reflections assignment confirm tetragonal perovskite for both samples (Space group I4/mcm (Z =4)). PbI_2 presence in PVK sample (see the peak with the star at about 12.6° related to (110) plane) is due to incomplete conversion. XRD analysis using Scherrer equation suggests the existence of nanocrystallites of 30 nm size for both samples.

In order to get information on the ionic motion in perovskite solar cells, we perform electrical measurements both in vertical and in lateral architectures. In this second configuration a larger number of interfaces, where ions can accumulate, are present because the distance between electrodes are of the order of tens of μm and not of hundreds of nm as in the first case. The lateral configuration was therefore used for enhancing the contribution of grain boundaries.

I-V measurements were performed in dark and light on a lateral structure with interdigitated gold fingers (ID), where C-PVK or PVK thin films were deposited by spraying the colloidal inks, as described in the 3.1.2 methods sections.

In Fig. 3.1.10 are reported the I-V measurements in dark. The data are compared with the measurements obtained with a thin film of the usual solution-processed perovskite (SP-PVK) obtained in a traditional synthesis [146], namely, in solution and without the PbI_2 obtained by LASiS.

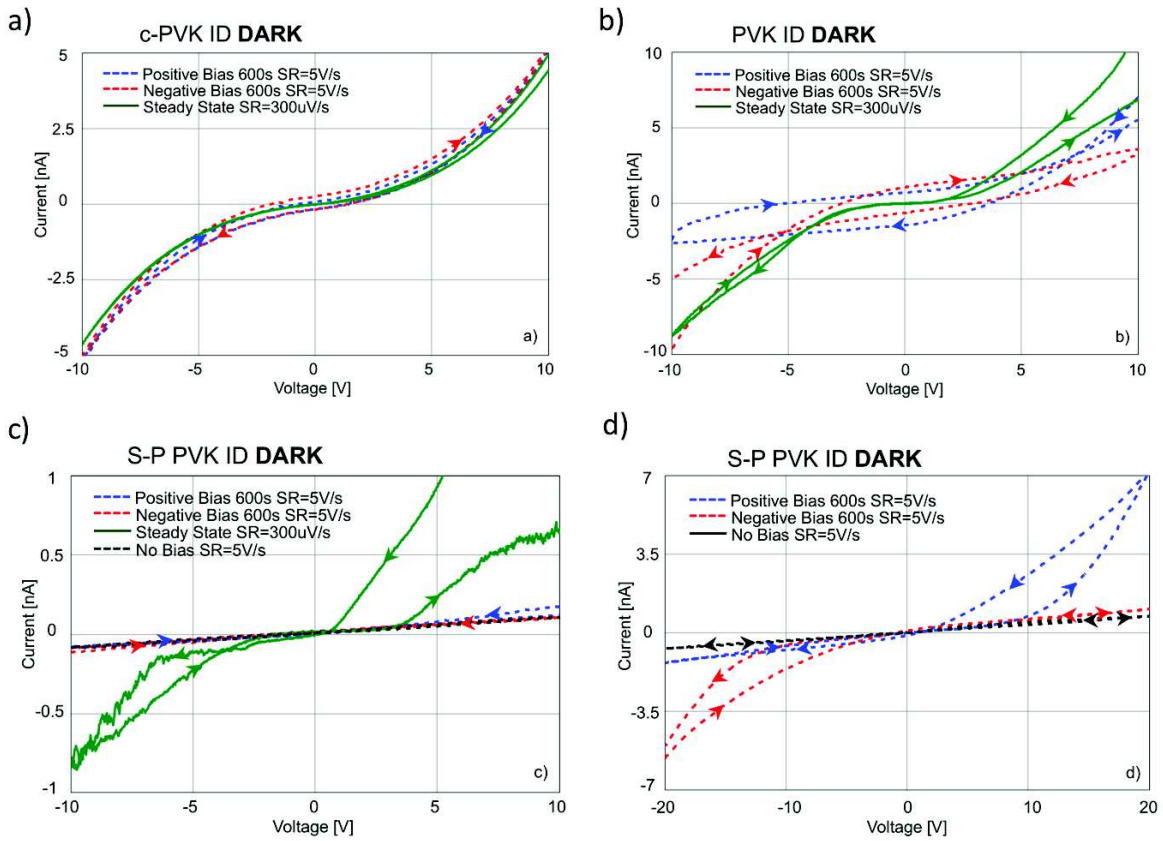

Fig. 3.1.10 I-V characterization in dark conditions. a) C-PVK, b) PVK, c) and d) SP-PVK without and with steady state curves, respectively. c) and d) differ for the voltage range applied.

The spraying coated C-PVK film (Fig. 3.1.10a) shows a symmetric behavior, whereas the PVK film (Fig. 3.1.10b) shows some asymmetric currents, namely when a reverse (forward) bias is applied before the voltage scan, the forward (reverse) current is lower than reverse (forward) current. The behavior of PVK film is the typical "rectifier" behavior of perovskite based devices, which was suggested by the Huang et al. [162] and De Bastiani et al. [124] to be the consequence of a p-n junction formation at one of the two gold electrodes. The same but enhanced behavior can be observed in the traditional solution-processed perovskite film (SP-PVK) (Fig. 3.1.10d). Considering the steady-state curve (Fig. 3.1.10c, green curve), SP-PVK shows larger instability towards voltage scan when compared to C-PVK or PVK samples. It is noteworthy to underline that steady-state curves are obtained by a continuous bias of the sample at 300 μV/s for more than one day, which is a voltage-stress for the materials usually not considered in the literature.

The observed 'rectifier' behavior can be rationalized with the scheme reported in Fig. 3.1.11, also according to previous suggestions [124,162].

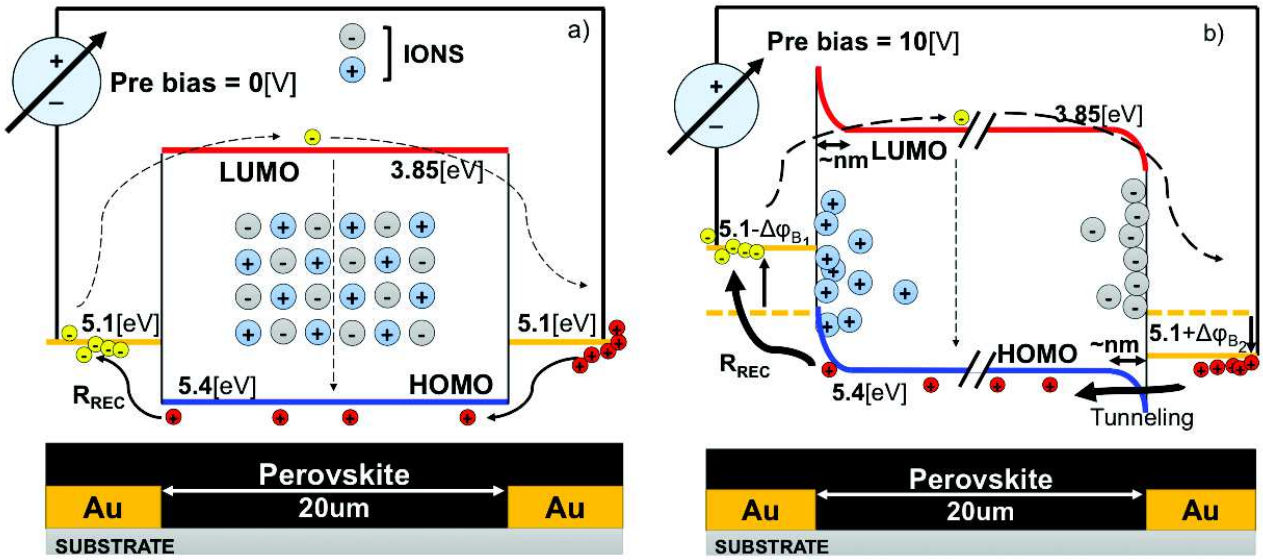

Fig. 3.1.11 The band diagram represents the device at flat-bands and after different applied pre-bias voltages: a) the pre-bias is 0 V; b) pre-biasing 10 V until steady state.

Upon the application of an electric field (Fig. 3.1.11b), ions within the perovskite thin film can migrate to the electrodes. Simulating the ions drift/diffusion with 10^{18} ions/cm^3 concentration [163], one finds that a band bending occurs at the interfaces within a region width of approximately 10-30 nanometers. This band bending can be approximated with a dipole that forms at the interfaces, which changes the valence and conduction band alignment with the electrodes. As a result, a diode like behavior is observed in the I-V scan. Using a very slow scan rate, the behavior can be interpreted as a DC steady state characterization. This justifies the green continuous curve in Fig. 3.1.10b where an abrupt increase in the slope above/below 2.5V/-2.5V is observed and suggests that above/below these thresholds, the dipole shift is so relevant that the electrode/perovskite interfaces behave like an ohmic contact, thus changing the slope of the curve. This is also supported by the linear behavior above/below 2.5V/-2.5 and within low electric field (Emax = 5kV/cm corresponding to 10 V for ID with 20 μm distance between gold fingers).

In Fig. 3.1.10a the symmetrical current voltage curve observed for C-PVK, in accordance with [145] and the above interpretation, shows that for C-PVK negligible or no dipoles are formed at the perovskite/electrode interfaces, also when the device is pre-biased. This can be interpreted, therefore, with a hindered motion of ions in C-PVK. One observes that C-PVK resistance to degradation, during measurements, is higher compared to PVK and particularly to SP-PVK, since the forward and backward steady state scans overlap almost perfectly although the measurement takes up 36 h to complete. I-V measurements were also obtained with a MIM structure (see Fig. 3.1.12). In these cases, the clear "rectifier" behavior found with ID samples is almost not observed for all materials (C-PVK, PVK and SP-PVK). The difference with the ID measurements can be understood with the different distance between electrodes, which is two orders of magnitude larger for ID samples (20 μm for ID and 200 nm for MIM). In the case of ID sample the larger number of grain interfaces, where the ionic motion occur, between electrodes, amplifies the rectifier behavior of the samples. I-V curves for ID structure under light show very similar behavior for all the samples (Fig. 3.1.13). This suggests that under illumination photo-generated carriers dominate the conduction, whereas injected carriers are negligible with respect to the whole charge flow.

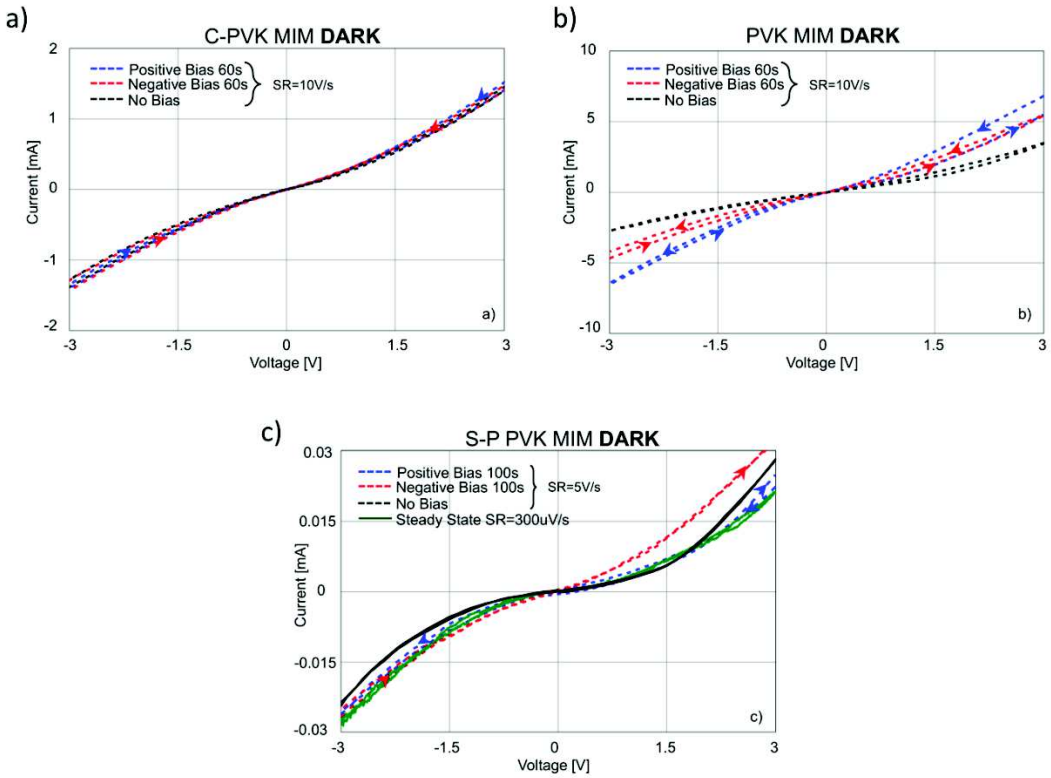

Fig. 3.1.12 I-V characterization of MIM samples in dark conditions. a) C-PVK, b) PVK, c) solution-processed thin films, respectively.

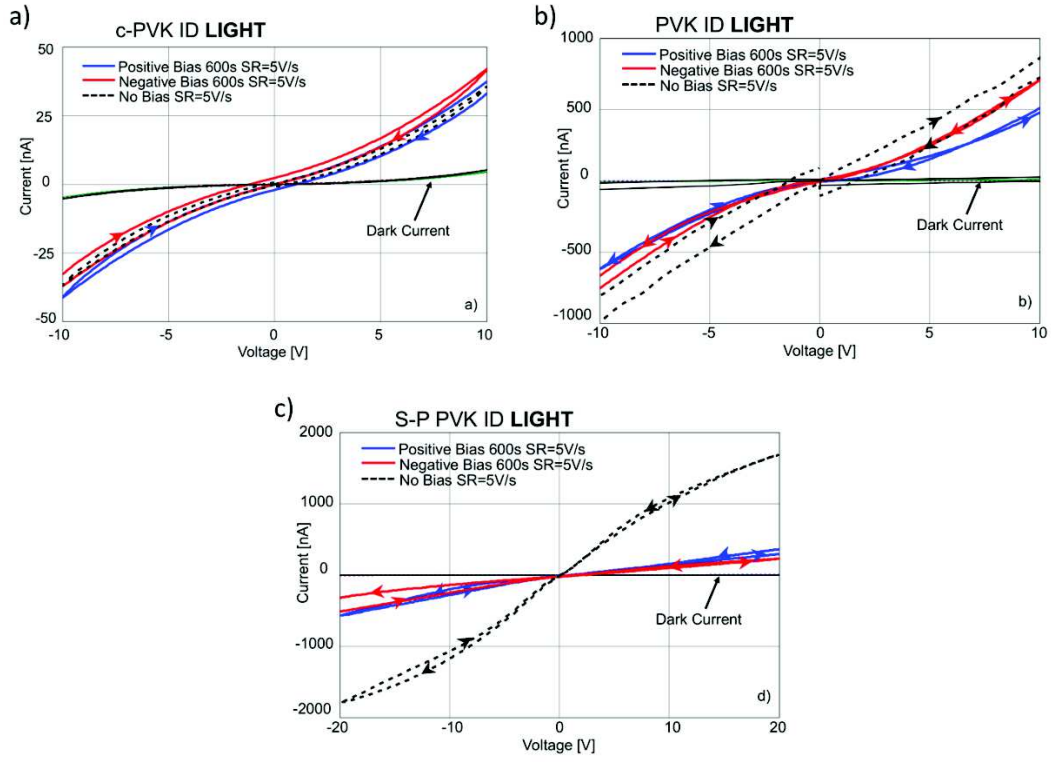

Fig. 3.1.13 I-V characterization of ID samples in light conditions. a) C-PVK, b) PVK, c) S-P PVK, respectively

The comparison of the results for C-PVK and the other materials shows that the role of the graphitic materials produced by the laser ablation of PbI_2 can be considered the origin of their different electrical behavior. Since the electrical measurements can be interpreted with a hindered ionic motion in C-PVK, one can model this behavior considering the interaction of the graphitic material present on the nanocrystal grain boundaries. Ionic motion in perovskite materials is made possible by the presence of different defects related to vacancies (V), interstitial atoms (I) and anti-sites (A) of iodine, methyl-ammonium (MA) and Pb. Several calculations have shown that these defects can be present within the electronic gap of perovskite [133,164–167] and according to calculations some defects can operate as electron/hole acceptors like I_{Iodine} or I_{MA} [166,167].

The hindered ionic motion present in C-PVK can be interpreted considering that the defects, although present, are less available in this material. Since the EPR and SKPM measurements show that the graphitic material is active in a charge transfer interaction, one can deduce that the transfer of electron/hole to the perovskite makes the defect states less available to the ionic motion, which can be considered a passivation of defect states present in the energy gap region of the perovskite [168]. The sketch reported in Fig. 3.1.14 would like to recall such an interpretation with defect states present in the electronic gap of the perovskite and the exchange of electrons/holes with the graphitic material.

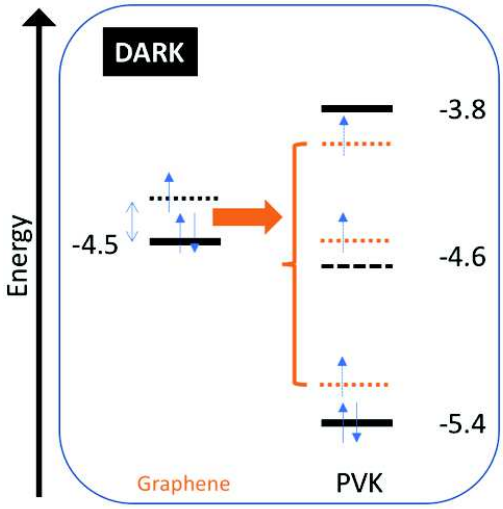

Fig. 3.1.14 Proposed mechanisms of C-PVK behavior under dark conditions.

The presence of a graphitic shell around the perovskite nanoparticles has positive effects on both stability and lowered hysteresis of the standalone material. However, despite hindering the ionic motion within the active layer, the semi-conductive graphitic materials might increase the non-radiative recombination rates of the injected/photo-generated charges or even create conductive paths between the electron and hole transport layers, thus causing a higher shunt in the resulting solar cell or lowering the efficiency of LEDs. Therefore, further research is necessary to assess the effects of these graphitic materials and testing them in fully structured devices is mandatory to evaluate the impact of the graphitic shell on both devices performance and endurance.

3.1.4 Summary

The laser ablation synthesis in organic solvent of PbI_2 nanocrystals made possible to obtain different types of perovskite materials depending on the solvent used as a bath for the target. A hybrid graphite-lead iodide precursor was obtained with a strong interaction among materials, since the graphite was obtained with the decomposition of the solvent on the surfaces of the nanocrystals. Among the characterization techniques, the EPR one allowed to evidence the presence of a charge exchange between the nanocrystals and graphene-like patches at the grain boundaries making less available the defect states of perovskite material to the ionic motion. The electrical characterizations confirm that thin film graphite-lead iodide based perovskite has a less hysteretic behavior than the reference spin-coated thin film perovskite. These results shed light on the key role of defect sites on the mechanism of ionic motion, providing a path for the synthesis of stable materials. However, further research is necessary to assess the effects of the graphitic shell in fully assembled devices.

3.2 Understanding lead iodide perovskite hysteresis and degradation causes by extensive electrical characterization

Section 3.2 is an extracted of the corresponding published paper Ref. J16

3.2.1 Introduction

A promising alternative to the usage of polymers to hinder ionic motion is the perovskite processed from solution-ablated precursors developed by Lamberti et al., which proved outstanding resistance and low hysteresis [145,169]. Indeed, while standard solution processed perovskite could not survive extensive electrical characterization and showed irreversible degradation in a few hours, laser-ablated derived perovskite proved higher tolerance and resistance both to electric field and environmental exposure.

We exploit the endurance of methyl-ammonium lead iodide (MAPI) derived from laser-ablated precursors to investigate the hysteretic phenomena of MAPI perovskite, i.e. one of the most commonly used material in high performance PSCs. Since MAPI from laser-ablated precursors endures prolonged electric field application, it allows for extensive electrical characterizations, permitting measurements that were impossible on standard solution processed MAPI. Thus, we could investigate whether the hysteresis is mostly due to ions and/or ferroelectric properties of the perovskite material (PVK) by using extremely low scan rates. Besides, having MAPI derived from laser ablated precursors a slower degradation dynamic, we could detect the effects of the hysteresis on the material. We proved that different mechanisms contribute to the hysteresis observed in PSCs and that ion migration is responsible for both long term transitory effects and permanent structural changes in the PVK layer, altering the electrical properties of the studied devices. Since the studied material is similar to the standard MAPI, we believe that our results can be extended to solution-processed perovskite both on planar and vertical structures, despite being more challenging to study the phenomena on those devices.

Finally, we modeled the perovskite bands bending explaining the mechanisms behind current injection/extraction into/from the hybrid-organic semiconductor, which is of the utmost importance in the understanding of the band alignment for photovoltaics applications.

3.2.2 Methods

3.2.2.1 Setup and devices structure

Performing the characterization in inert atmosphere and at controlled temperature is mandatory in order to limit degradation to electric field induced effects. Fig. 3.2.1 describes the developed setup (Fig. 3.2.1a) and the devices structure (Fig. 3.2.1b). We run all the electrical characterizations in nitrogen at 25°C, if not otherwise stated, by using custom developed hardware and instrumentation. An additional external aluminum black box encloses the nitrogen box in order to prevent external light and EMI radiation interferences; both boxes are grounded. The temperature controller is peltier-based and allows setting the sample temperature from 80°C to -20°C.

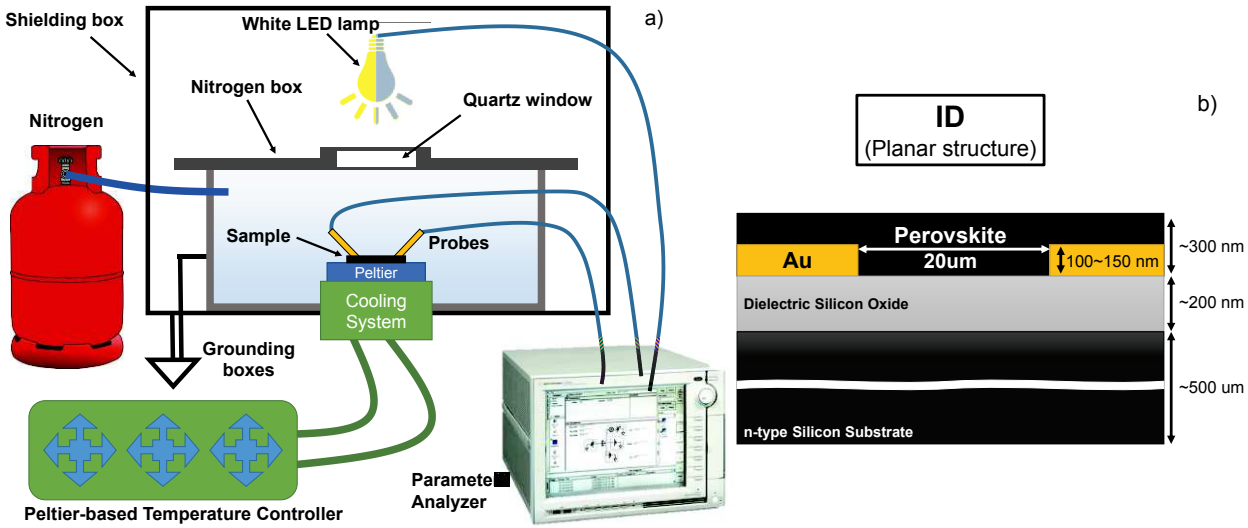

Fig. 3.2.1 Setup developed to run the electrical measurements a). The nitrogen and temperature-controlled systems are used in order to prevent the device degradation during the characterization. The shielding box prevents external light and EMI interferences while measuring the device. Representation b) of the planar structure used.

We fabricated planar interdigitated devices (IDs), using 10x10mm^2 crystalline silicon substrates (FBK, Fondazione Bruno Kessler) covered by silicon oxide and patterned with interdigitated golden electrodes (work-function Φ_{Au} = -5.1eV). IDs have a 20um PVK active layer between golden electrodes; Fig. 3.2.1b gives more details on the geometries of the substrate. Furthermore, we coated a 10x10mm^2 FTO/glass substrate (TEC 7, 2mm thickness, Sigma-Aldrich) for optical characterizations.

3.2.2.2 Devices preparation

The IDs and FTO/glass devices were obtained depositing the precursor ink into the respective substrates by spray coating. Spray coating was performed by using a home-made system based on Professional Dual Action Airbrush Set / Kit with gravity feed (ExquizonEU) operating with nitrogen flow of 3 bar (20°C). The substrate was positioned vertically, 2cm far from the nozzle tip and kept at 50°C during the deposition. 1ml of precursor ink was sprayed in air under extractor hood (20% humidity). The spray-coating process was controlled by means of stepper motors with horizontal and vertical steps equal to 10mm and 200µm respectively, for 3 cycles. The width of the spray-coated layer was about 1/3 of the substrate dimension. After PbI_2 film deposition, the sample was converted to PVK dipping the substrate in 10mg/ml methylammonium iodide (MAI) anhydrous isopropyl alcohol (IPA) solution for 3 minutes, then rinsed in fresh anhydrous IPA and finally in anhydrous dichloromethane. Converted perovskite films thickness is about 1µm as measured by

scanning electron microscopy (SEM) cross section. More details on the processing of laser ablated (LASiS) materials are available in ref. [169].

3.2.2.3 Optical characterizations

We run ultraviolet photoelectron spectroscopy (UPS) analysis on MAPI PVK sample to estimate the work function of the materials under investigation. We used a Kratos Axis UltraDLD spectrometer. The UPS measurements were taken using a He I (21.22 eV) discharge lamp, on an area of 55μm in diameter, at pass energy of 10 eV and with a dwell time of 100ms. The work function (i.e. the position of the Fermi level with respect to vacuum level) was measured from the threshold energy for the emission of secondary electrons during He I excitation. A −9.0 V bias is applied to the sample in order to precisely determine the low kinetic energy cut-off, as discussed in ref [170].

We collected Raman measurements by means of a custom setup equipped with an Ar+/ Kr+ gas laser (Coherent, Innova 70) tuned for emission at 514.5 nm. The laser is focused on the sample through an Olympus BX 41 microscope with a 20x objective (Olympus, LMPlan FLN 20×, NA = 0.40). The Raman scattering diffused by the sample is coupled into the slit of a three-stage subtractive spectrograph (Jobin Yvon S3000) and detected by a liquid nitrogen-cooled CCD (Jobin Yvon, Symphony, 1024 × 256 pixels, front illuminated). The laser spot diameter is about 2 μm. The laser power used during the measurements is 250 μW for PbI_2 powder, MAI powder and PVK on SiO_2, 25 μW for PVK on Au. The integration time is 10s (and 30 averaged acquisitions) for PbI_2 and 20s (and 100 averages) for MAI powders, 20s (and 30 averaged acquisitions) for PVK on SiO_2 and 20s (and 60 averaged acquisitions) for PVK on Au. All measurements were carried out in standard conditions.

We recorded X-ray diffraction spectra (XDR) with a BRUKER D8 ADVANCE diffractometer with Bragg–Brentano geometry and equipped with a Cu Kα1 (λ = 1.544060 Å) anode at operating voltage of 40 kV and operating current of 40 mA. All the diffraction patterns were measured at room temperature over an angular range (2θ) between 6° and 60°, at step size of 0.020°, and an acquisition time of 1 second. Step size was used as error source for experimental data.

3.2.2.4 Electrical characterization

An Agilent B1500 parameters analyzer is used for the electrical characterization of the samples and control of the white led lamp used as light source. High-resolution source measurement units (SMU) are used to measure electrodes current, while a high-power SMU unit drives the light source. We run light measurements under a white LED biased to give a light power density of approximately 50mW/cm^2.

Current voltage scans (I-V) are with a scan rate of 5V/s and 300μV/s for fast scan and steady-state scan, respectively. Using two scan rates that differ orders of magnitude allows distinguishing temporary phenomena from permanent ones and thus distinguishing the phenomena behind the hysteresis. Tab. 3.2-A summarizes the timings, scan directions, voltage ranges and illumination used for characterizing the samples.

We define a scan as positive when we measure a forward scan from 0V to 5V immediately followed by a backward scan from 5V to 0V. On the other hand, we define as negative a scan going in the opposite direction, thus we first measure from 0V to -5V and then from -5V to 0V.

	SR [V/s]	**Scans Direction** & **Voltage Range** [V]	**Light - LED** (50mW/cm^2)
I-V Fast	5	Negative: 0 → -5; -5 → 0 Positive: 0 → +5; +5 → 0	OFF - ON
I-V Steady-State	300E-6		OFF

Tab. 3.2-A Specifications on the characterization timings, direction, voltage ranges and illumination used.

We repeated positive and negative scans several times with the different scan rates in order to monitor any appreciable differences in the devices behavior related to the characterization itself and prolonged applied electric field. Fig. 3.2.2 shows the complete electrical characterization including seven cycles of measurements. Starting and ending cycles (#1 and #7) are equivalent; these measurements purpose is to compare the devices at the beginning and at the end of the complete characterization. The check cycles (#2, #3 and #4) comprehend only steady-state scans in order monitor and test the devices resistance to measurement-induced degradation. The full cycle (#5) measures fast scans both in light and in dark after a steady-state I-V in positive and negative directions. Finally, the storage cycle (#6) is intended to let the device rest such that relaxation phenomena could be detected with the ending cycle of measurements.

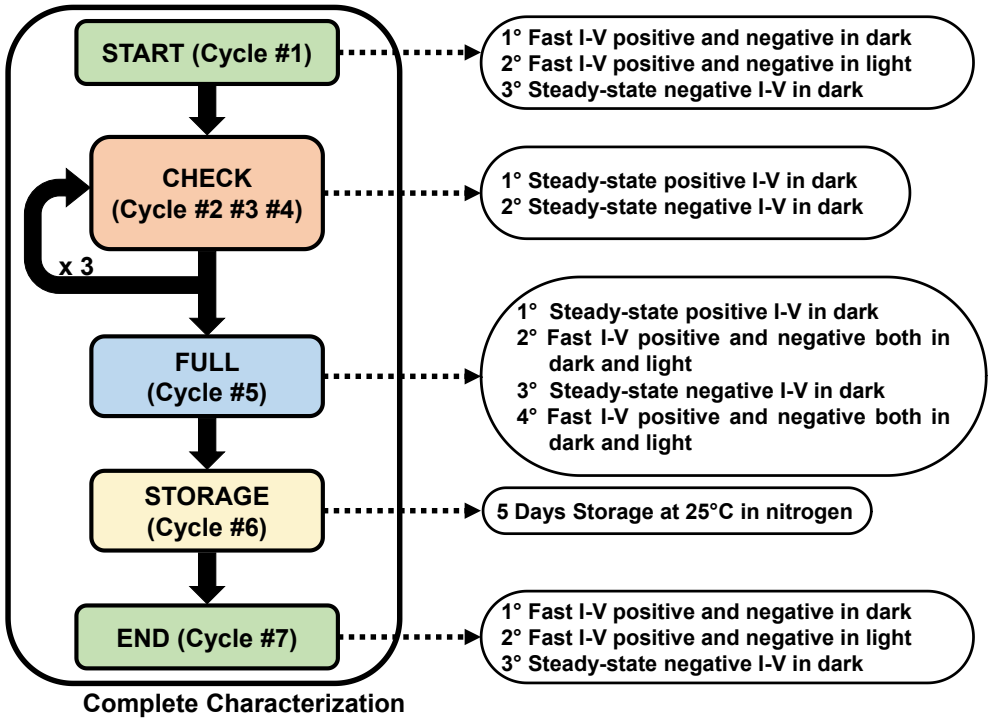

Fig. 3.2.2 Specifications on the measurements type and order used during the complete characterization.

3.2.3 Results and Discussions

In [145,169] some of us showed that the analyzed MAPI perovskite exhibits a rectifying current-voltage behavior in dark, as a consequence of keeping the devices pre-biased at positive or negative voltages before the I-V scan is measured. On the other hand, such phenomenon does not occur when the device is measured after storage or is kept pre-biased at 0V for a long time before the current-voltage scan. According to [169], we suggested that this behavior is correlated to the presence of ions that drift-diffuse through the grain boundaries of the perovskite layer. The rectifying behavior is temporary and it vanishes once the device is kept in storage (or biased at 0V) since ions move back and uniformly re-distribute within the perovskite layer.

The fact that the analyzed material shows higher resistance to electric field induced degradation when compared to standard solution processed perovskite allows for stressful characterizations to be run, therefore expanding the knowledge of the causes and effects behind hysteresis in perovskites. We cycled several scans both at fast and very low scan rates. Using several scan cycles and orders of magnitude different scan rates allow investigating temporary/permanent phenomena and testing the robustness of the perovskite to the applied electric field. In particular, the 0.3mV/s current-voltage scans are intended to capture the steady-state curves of the device, thus revealing the real state of the device once all transient behaviors terminate. Optical characterizations are designed in order to support and validate the observed electrical data, in addition to provide further information for the model dynamics.

3.2.3.1 Current-voltage scans

Fig. 3.2.3 summarizes the typical current-voltage scans on IDs both in dark (Fig. 3.2.3a) and light (Fig. 3.2.3b) conditions. In Fig. 3.2.3a, both the fast scan and steady-state curves show hysteresis, despite the very low scan rate used in steady-state measurements. We exclude that ferroelectric domains polarized by the electric field might be responsible for the observed behavior and whether they exist, we suggest they are negligible. Indeed, the different response to variable scan rates and the transient nature of the current voltage curves eliminate the ferroelectric hypothesis, as we will better explain in the following paragraphs. On the other hand, the data at very low scan rate could suggest that in addition to some ionic species (usually iodine ion I^-) associated to perovskite hysteresis, there are others moving within the perovskite at a much slower pace. The photo-generation properties of the device are clearly evaluable in Fig. 3.2.3b, where the comparison of light and dark curves show that the currents differ by more than two orders of magnitude. Furthermore, by comparing Fig. 3.2.3a and Fig. 3.2.3b we notice that we can easily approximate the curves by a linear fit under illumination, while in dark the conduction is non-linear. These different conductions indicate that photo-generated charge dominate the injected charge in light, at least at the selected illumination and voltage.

Ion drift-diffusion within organic-inorganic semiconductors has been widely studied [171–174] and the rectifying phenomenon in PVK materials was already explained in several works as the consequence of ion drift-diffusion through the active layer, in particular on planar films [123,124].

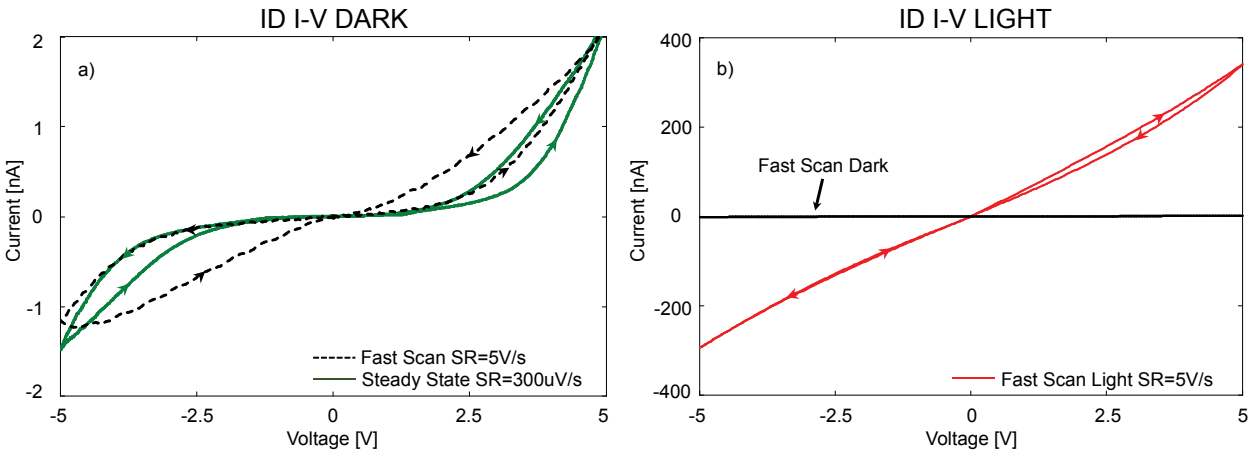

Fig. 3.2.3 I-V scans at different scan rates on an ID in dark a) and in light b), where we added the dark current for comparison.

However, no one to the best of our knowledge has ever recorded current-voltage scans with such a low scan rate that is a good approximation of the steady-state condition. Fig. 3.2.4 focuses on the detail of the steady-state curve around 0V captured both on cycle #1 (Fig. 3.2.4a) on a fresh device (i.e. not measured neither stressed before), and in cycle #2 (Fig. 3.2.4b). The insets in Fig. 3.2.4 represent the absolute value of the currents in logarithmic scale to emphasize the zero-current crossing voltage for each scan. Comparing the scans at different cycles, we notice that the steady-state scan on cycle #1 from 0V to -5V on a fresh device has the zero-current crossing voltage at 0V, while the backward scan from -5V to 0V crosses around -0.25V. Then, in cycle #2, during the positive scan at 0V the current is above zero, while the backward scan crosses zero-current at 0.24V.

The same repeats during the following cycles from #3 to #5, similarly to what observed by Huang et al. in their work [123]. Only with cycle #7 we recorded an I-V in steady-state that starts with zero-currents at zero at 0V. This occurred after cycle #6, leaving for 5 days in storage conditions and unbiased the device. Thus, the residual voltage is a recoverable phenomenon that disappears after storage.

We think that the reset of the device, occurring after the storage at controlled temperature, is due to the slow diffusion of ions occurring within the PVK. The storage allows the ions accumulated at the interface with the electrodes to diffuse back to their initial isotropic distribution, eliminating the residual zero-current crossing voltage (V_{DIP}) measured during the steady-state scans. If V_{DIP} was due to ferroelectric domains switching during the scan, the domains should not reset unless there is a change in the PVK temperature, applied electric fields or even longer relaxation times. Furthermore, ferroelectric domains should switch and produce the V_{DIP} voltage even with fast scans, which is not the case. Thus, we consider negligible the effects of ferroelectric domains contributing to the observed hysteresis. In agreement with Beilsten-Edmands et al. [121], we associate this behavior to heavy ions (Pb^{2+} and/or MA^{+}) moving within the PVK layer.

Finally, comparing Fig. 3.2.4a and Fig. 3.2.4b we notice the presence of flexes around ±1.25V (red dotted circles) when scanning from 0V to ±5V in Fig. 3.2.4b, while there is no flex in Fig. 3.2.4a. Similar to V_{DIP}, these flexes are recoverable effects due to the ionic migration. The flexes disappear if we leave the device in storage conditions long enough and their weight on the current-voltage curves lower with continuous steady-state measurements. The storage allows a reset of the ion distribution, while the continuous measurements induce a degradation of the interfaces, as explained in the following sections, which weakens the formation of these flexes.

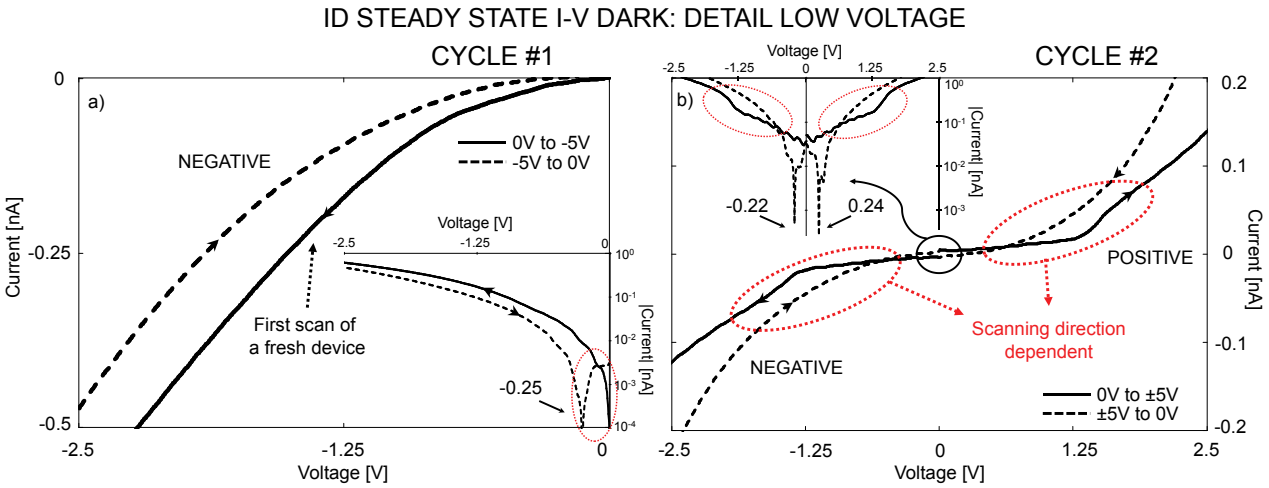

Fig. 3.2.4 I-V steady-state scan detail at low voltages. The zero-current crossing voltage depends on the scanning direction. From 5V to 0V a positive voltage (0.24V) remains at zero-crossing current, while from -5V to 0V a negative voltage (-0.22V). Red dotted circles envelop the current flexes that are scanning direction dependent. If the device scanned is fresh and unbiased a) the current flex is not present and the scan starts from 0A (red dashed circle) otherwise b) there are flexes and V_{DIP}.

3.2.3.2 Morphological and optical analysis

The top and lateral view of the scanning electron microscopy (SEM) are shown in Fig. 3.2.5a and Fig. 3.2.5b respectively. Fig. 3.2.5c shows the Tauc plot [175], Fig. 3.2.5d the UPS, whereas Fig. 3.2.5e the XDR. The SEM image of Fig. 3.2.5a shows the typical cubic shape for tetragonal perovskite lattice with an average size of 200nm. The lateral view on Si substrate shows a compact thick film of approximately 1.3um (Fig. 3.2.5b). No PbI_2 spherical particles are visible in SEM images; furthermore, the low-intensity peak at 12.6° in XDR pattern (Fig. 3.2.5e) related to PbI_2 phase is much lower than the high-intensity peak of (100) plane MAPI perovskite at 14.1° [145,169] confirming an almost complete conversion during MAI-solution immersion step. Because the average grain size of the spray-coated thin film is 200nm, in an ID device there is at least a hundred grains involved with the charge transport from an electrode to the other. According to Huang et al. [122], ions migrate within the PVK layer from grain to grain, preferring the paths across defective grain boundaries. In fact, Huang hints that the activation energy for ions hopping at the grain boundaries is smaller than on a single crystal. The migration stops when the drift-diffusion process is balanced and, when a bias is applied, ions accumulate close to the electrodes creating a charge accumulation at the gold fingers. The same occurs in a vertical metal-semiconductor-metal structure [169]; however, the migration related phenomena cannot be easily detected using electrical measurements in a vertical device, since the PVK thickness approaches the grain size. In fact, in these devices, the conduction from electrode to electrode involves just a few crystals and the number of defective interfaces is lowered. Thus, despite the structure used in solar cells is vertical, it is important to investigate these phenomena on planar devices, in order to exacerbate the ion effects and fully understand the PVK-based devices working principle.

The optical characterization of sprayed PVK on glass substrate allows estimating the perovskite band gap (1.52eV) that we can approximate from the Tauc plot provided in Fig. 3.2.5c. This value is in agreement with solution-processed tetragonal perovskite materials as reported in [176]. From UPS characterization, we extrapolated the HOMO band level and the Fermi level of the material. In Fig. 3.2.5d the UPS spectrum of a PVK sample sprayed on Au electrode is shown: the HOMO level is approximately 0.9eV lower than the -4.53eV estimated Fermi level. Using the extrapolated data, the calculated HOMO band ends at -5.43eV while the LUMO energy level starts at -3.91eV.

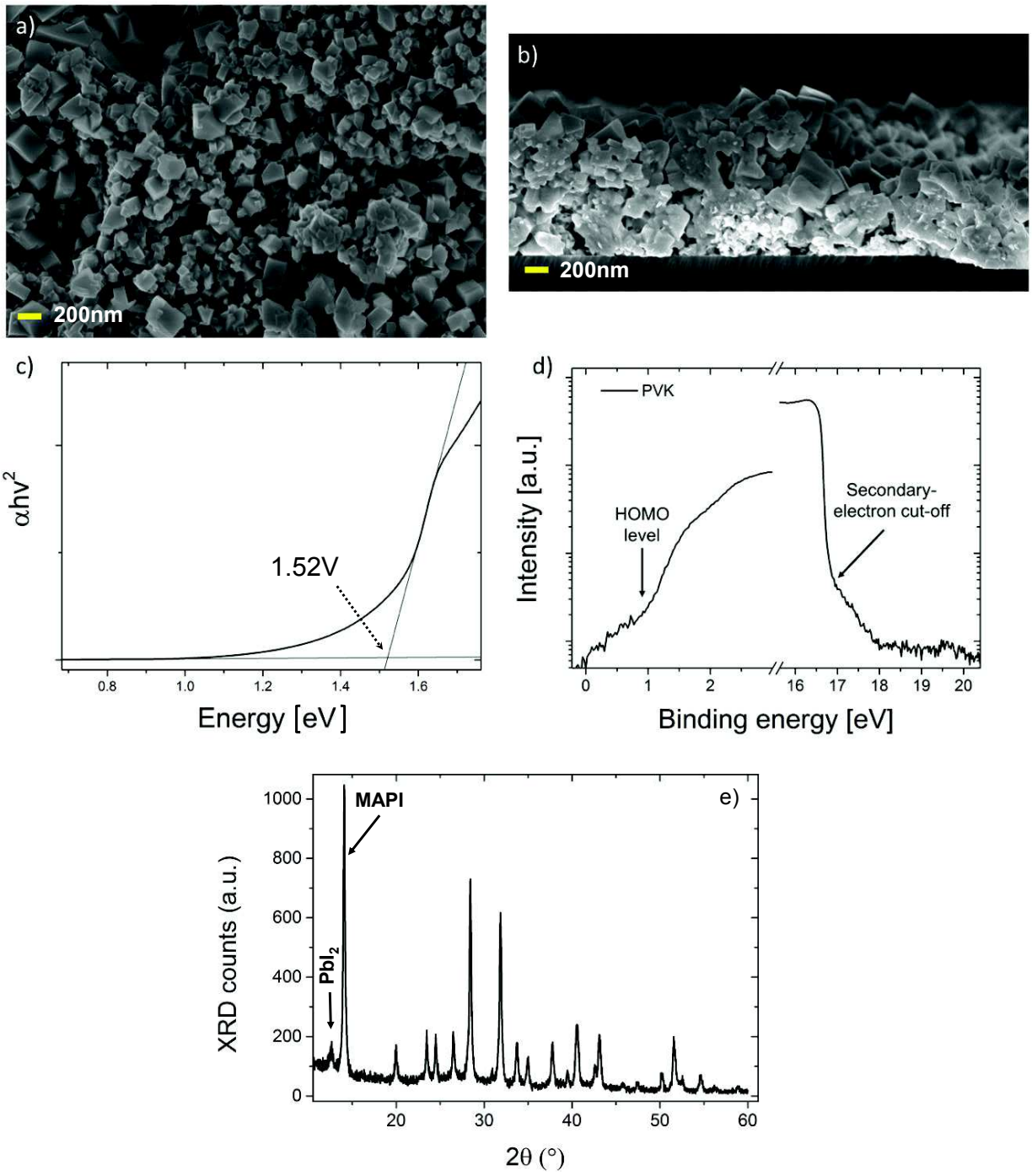

Fig. 3.2.5 Morphological and optical characterization of PVK film. a) Top view SEM image and b) lateral view SEM image. c) is the Tauc plot for PVK sample. The linear regression on the Tauc plot allows the estimation of the direct band gap as 1.52 eV. d) is the UPS spectrum of PVK sample highlighting HOMO level with respect to the Fermi level (4.53eV) and higher binding energies region for work functions estimation. e) is the XDR pattern of a MAPI sample; the low-intensity peak at 12.6° is related to PbI2 while the high-intensity peak at 14.1° is related to (100) plane MAPI perovskite, confirming the almost complete conversion into perovskite after MAI processing.

According to these values, the Fermi level is pinned toward the LUMO band and thus the material is n-doped, in contrast with values obtained from solution-processed perovskites reported in literature [177]. However, these results are in agreement with the concept of doping PVK by including in the film structure graphene/graphite materials with reported work function of 4.4-4.6eV [160,161]. The introduction of these doping materials is likely due to the laser ablation process and explains the overall Fermi level shifts toward the LUMO band [169].

3.2.3.3 Ion migration induced perovskite degradation

In addition to give rise to reversible hysteretic behaviors such as the VDIP and the flexes, the ion migration is also responsible for the material degradation. Indeed, the high ion concentration in close proximity of the electrodes, upon application of bias, generates a huge electric field that damages the perovskite lattice.

Effects on I-V curve

Fig. 3.2.6 compares both steady-state dark (Fig. 3.2.6a) and fast light (Fig. 3.2.6b) I-V scans during cycle #1-2 and #5. Despite the inert atmosphere and the controlled temperature, the application of a prolonged electric field in dark during such an extended characterization can induce some permanent degradation observable both in dark and light curves. In Fig. 3.2.6a we see how the current decreases with time of measurement, as during cycle #5 the injected current is lower than during cycle #2 and #1. The current decrease is permanent and the current does not recover after storage. Except the fast scans and the first steady-state scan from 0V to -5V during cycle #1, in all the curves we detect the V_{DIP} voltage related to the device history, which is recoverable. Besides, we observe that with increasing cycles of characterization, the current flexes occurring when scanning from 0V to ±5V tends to vanish and disappear. We suggest that this effect and the current reduction are related to electric field induced degradation mechanisms.

In particular, the application of an electric field for a long time (as is the case for the steady-state I-V scans) allows ions to migrate and accumulate. The migration stops when drift-diffusion is balanced. However, this migration leads to a high concentration of ions in close proximity of the electrodes. We suggest that such a high concentration of ions is the source of the PVK degradation close to the contact, since it generates a high electric field. The high density of ions has a negative effect on the PVK, inducing a high level of stress on the MAPI lattice. Therefore, a lattice-degraded layer starts surrounding the gold electrodes limiting the injected current (Fig. 3.2.6a) and the extracted photo-charge as we observe in Fig. 3.2.6b. Indeed, the extracted photo-generated current is lower in cycle #5 than in fresh devices, but this difference is not comparable with the variations in the injected dark current during the respective cycles. Moreover, the extracted photo-current from a fresh device can be approximated by a linear fit, while the photo-current measured on the same device in cycle #5 is considerably different.

Finally, in Fig. 3.2.6b (inset) we continue to observe the presence of a V_{DIP} voltage. V_{DIP} is approximately -0.28V (dashed blue line with empty circles) when the previous measurement was a negative steady-state scan and 0.25V (orange dashed line with empty triangles) in case of a positive steady-state scan. On the contrary, the fast scan in light on a fresh device or after storage crosses the zero-current at 0V.

Although the planar structures of the IDs exacerbated this phenomenon, the presence of V_{DIP} is in accordance with well-observed long time open circuit voltage decay occurring in PVK solar cells [20] and with pre-polarization affecting solar cell performance [178].

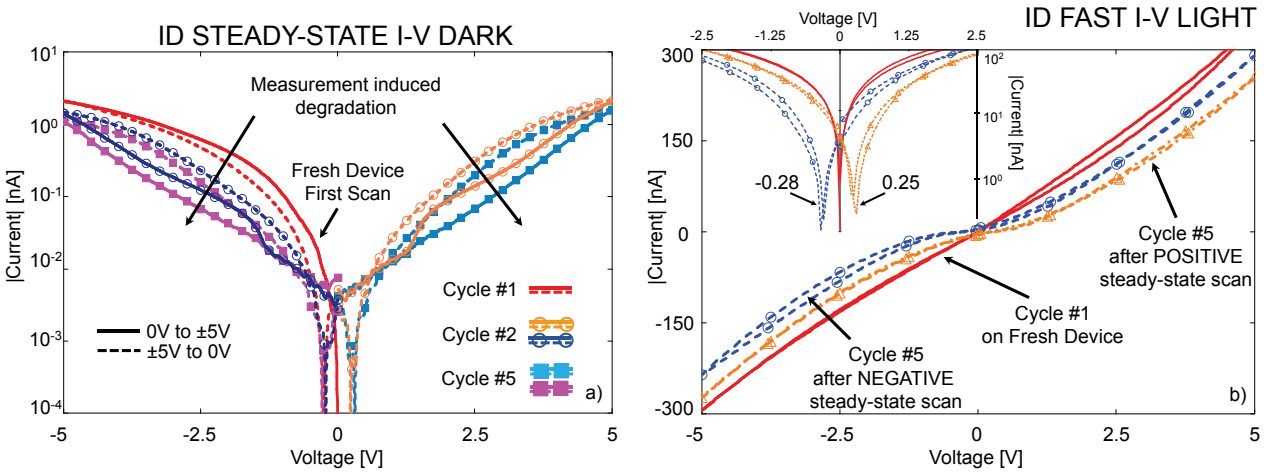

Fig. 3.2.6 a) Steady-state scans of an ID sample in dark during several cycles. Continuous lines stand for scans from 0V to ±5V, while dashed lines for scans from ±5V to 0V. Circles indicate the positive and negative scans during cycle #2 measurements after the first scan of the fresh device (red lines) while the filled squares curves indicate the steady-state I-V during cycle #5. b) Fast I-V curves in light of the same sample as in a) at different measurement steps. Red continuous line is the fresh device; blue dashed line with circles is after the cycle #5 negative steady-state scan; orange dot-dashed line is after the cycle #5 positive steady-state scan. The inset in b) underlines the presence of a residual built-in voltage in the curves when measuring in light after steady-state scans.

Electric field effects on the PVK lattice

In order to verify our hypothesis on the existence of a degraded layer surrounding the electrodes, we recorded Raman spectra in different regions and on different IDs samples as shown in Fig. 3.2.7. The blue curve represents a sample measured on gold fingers after cycle #7 electrical characterization, whereas the red curve represents a fresh device measured on Au and stored unbiased for the same amount of time. The Raman spectrum of MAPI at standard conditions does not show any significant peaks and such is the fresh perovskite sample (red curve) [179,180]. On the other hand, several peaks appear for the fully characterized device measured on gold electrodes. The appearance of such peaks is compatible with the presence of crystalline lead iodide [181]. Specifically, the peak at 94 cm^{-1} is due to Pb-I stretching [182] as well as the peak at 110 cm^{-1} is related to longitudinal modes (with the second order present at 215 cm^{-1}) vibrations [183]. Furthermore, the blue line peak at 110 cm^{-1} can be ascribed both to PbI_2 and MAI [179], since it probably represents the overlapping of the reference signals measured as powder compound (dashed curves). Additionally, we measured the Raman spectrum between the electrodes, where the perovskite is grown on the SiO_2. Spectra collected between the electrodes (green curve in Fig. 3.2.7) both on a fully characterized and on a fresh device do not show the presence of perovskite precursors. Thus, we assume that the destructive effects of ion migration seen on both IV measurements and Raman spectra were due to the high ion concentration and electric field close to the contacts [184].

The conclusion is straightforward: the prolonged biasing during the steady-state measurement causes ionic migration that progressively and irreversibly degrades the perovskite lattice close to the electrodes, by leaving a lead iodide-based thin film with MAI, following an accepted mechanism already reported in literature [185].

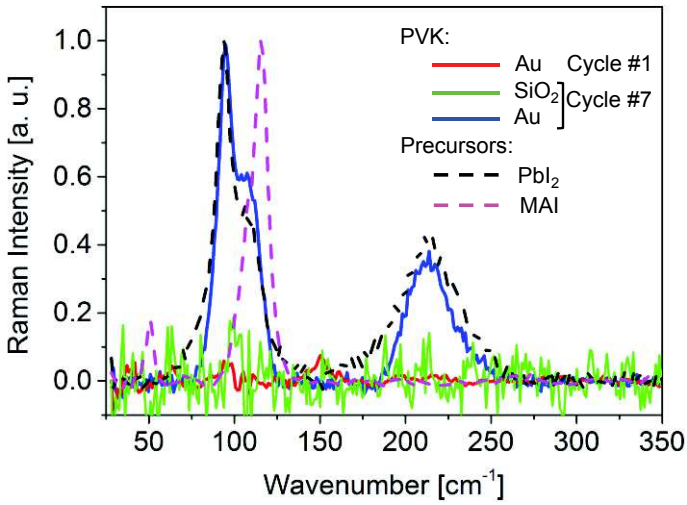

Fig. 3.2.7 Raman characterization of PVK sprayed on ID substrates on a fresh device and after the cycle #7. We added PbI_2 and MAI powders Raman spectra as a reference.

3.2.3.4 Qualitative model

In order to simplify the understanding of the phenomena generated by the electric field to the readers, we present a qualitative model that explains the effects of ion migration within the PVK layer. Fig. 3.2.8 shows the qualitative band bending of the device in dark under different applied biases. Fig. 3.2.8a represents the fresh device unbiased. Here, ions (light blue and gray spheres) occupy their initial position in the lattice and are distributed uniformly within the layer, thus the bands are flat. Fig. 3.2.8b shows the device biased in steady-state condition (5V in the example). Dipoles are generated at the interfaces with gold electrodes due to charge accumulation. These dipoles are few nm thick (10~50nm) [186] and they enhance holes/electrons injection via tunneling (since we are using gold as electrodes - 5.1eV - hole injection is more likely). Thus, the creation of such dipoles produces an effect similar to the functionalization usually adopted in organic devices to promote charge injection [187–189].

Once the dipoles width is in the nanometers order, the charges easily cross the potential barrier by tunneling. Therefore, the dipole potential barriers are not impeding but promoting the charge injection, since the dipole heights are equivalent to shifts of the electrode work functions (called $\Delta\varphi_{B1}$ and $\Delta\varphi_{B2}$ in Fig. 3.2.8) toward the HOMO/LUMO. If these equivalent electrode work functions align with the HOMO/LUMO band, we obtain an approximately ohmic contact. The effects of these dipoles are clearly visible in Fig. 3.2.3a, where we identify two different current-voltage regimes: |voltages| < 3V is injection limited; |voltages| > 3V is ohmic.

In Fig. 3.2.8c we depict a transient condition, where we represented the temporary bands bending occurring when applying a negative voltage (-2.5V) after that the device was kept at positive bias (5V) until steady-state.

In this transient condition, ions drift-diffusion is unbalanced. The dipoles are formed at the interfaces with the electrodes, but the equivalent work functions are shifted in the opposite direction if compared with the expected shifts at steady-state. During this transient condition, the injection barrier is higher compared to the cases shown in Fig. 3.2.8a and Fig. 3.2.8b and there is no tunneling of electrons/holes, resulting in a lower overall current.

The transient condition described in Fig. 3.2.8c might explain the flexes in the currents observed in Fig. 3.2.6a. Here, the first steady-state scan from 0V to -5V (red line) shows a higher current than the backward scan (from -5V to 0V in red dashed line), since the new-forming dipole is favorable to current injection, as in Fig. 3.2.8b. On the other hand, during the following measurement cycles the situation reverses, resembling the one in Fig. 3.2.8c. Thus, the currents measured from 0V to ±5V during cycles from #2 to #5 are lower than the backward currents from ±5V to 0V.

All these observations point to the fact that despite using such a low scan rate as 0.3mV/s, the resulting scans do not represent the final steady-state condition of the device, since the transitory phenomena persist. Probably heavy ions (Pb^{2+} and/or MA^{+}) are responsible for the hysteresis despite the low scan rate.

Moreover, the very long ion transient response may be behind the recoverable current flexes underlined in Fig. 3.2.4b. Indeed, the current injected into the PVK film is very low, until the dipoles, generated during the previous scan in the opposite direction, vanish. This occurs around ±1.25V in Fig. 3.2.4b. The current starts rising once the new-generated dipoles help the alignment of electrodes work function and PVK bands, enhancing the injection.

Finally, Fig. 3.2.8d shows what happens after the PVK film is biased for a prolonged time. The ions accumulated at the interfaces with the gold electrodes are responsible for a permanent damage of the PVK film, which converts back to the original precursors (PbI_2 and MAI detected by Raman in Fig. 3.2.7), leaving a degraded layer around the gold

electrodes that limits the current injection. Indeed, due to the HOMO/LUMO of these degraded layers, a higher injection barrier exists between the undamaged PVK layer and the gold electrodes that reduces the hole/electron injection and tunneling. The presence of these degraded layers explains the lowering of the dark current and the different shape and decrease of the light current with increasing measurement time, shown in Fig. 3.2.6a and Fig. 3.2.6b respectively. On perovskite solar cells, the generation of these degraded layers is responsible of an increase in the series resistance of the solar cell and an increased internal recombination, thus affective both fill factor and efficiency.

The fact that the PVK layer between the electrodes is undamaged is coherent with the presence of dipoles at the contacts. The dipoles at the interfaces compensate most of the externally applied voltage. Therefore, the electric field in the bulk PVK is much lower than close to the electrodes, as in Fig. 3.2.8b, with a consequent lower stress on the lattice.

Moreover, the layers might be behind the vanishing of the current flexes around ±1.25V observed in Fig. 3.2.6a. Indeed, the degraded layers are now interfering with the current injection into the PVK film, therefore they change the effects of dipoles, in particular on the tunneling probability of holes/electrons.

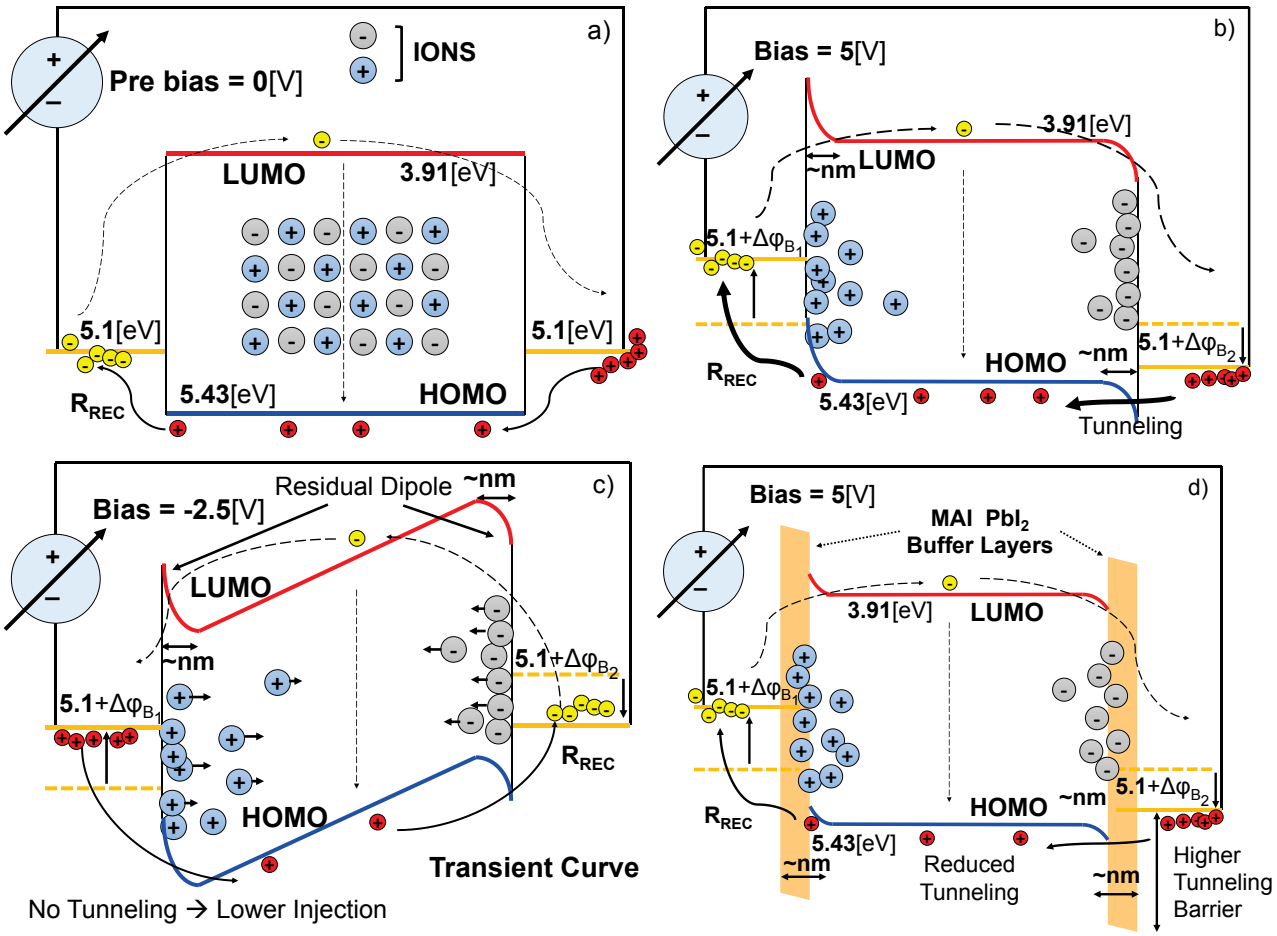

Fig. 3.2.8 Qualitative model representation of the band diagram without (a) and with (b) biasing the ID sample at steady-state conditions. c) is the qualitative band banding during a transient measurement, here the tunneling is reduced due to the persistence of a dipole generated during the positive steady-state scan. d) represents the situation occurring under biasing after prolonged exposure to high electric field in close proximity to the contacts, the tunneling current is reduced due to higher barriers generated by degraded PVK.

3.2.4 Summary

We studied methyl-ammonium lead-iodide perovskite material. MAPI is synthetized starting from spray-coated PbI_2 precursor obtained by laser ablation technique and is more robust against ion migration and electric field induced degradation, although being very similar to the standard spin-coated MAPI. The aim of our investigation was recognizing all the possible phenomena at the base of the electrical hysteresis characterizing perovskite devices. In particular, we aimed to distinguish between temporary and permanent phenomena generated during the current-voltage scans. We used electrical characterization at different scan rates and optical measurements to reach our goal.

The results of our measurements are straightforward: no or negligible ferroelectric phenomenon exists in the PVK and ion migration in the PVK has several effects, both positive and negative.

The ions move following the drift-diffusion law and the migration occurs mainly in the MAPI grain boundaries. Under the effect of applied bias, ions accumulate at the interfaces with the electrodes, generating dipoles. The dipoles change the band alignment of the semiconductor with the electrode work functions and thus they change the current injection dynamics, in particular changing the current injected by tunneling effect.

However, due to the high electric field at the interfaces generated by the ions accumulated, a degradation mechanism occurs that converts back to the initial precursors (MAI and PbI_2) the PVK layer. Therefore, insulating degraded layers generate around the electrodes, limiting the current injected in dark and extracted in light. The presence of these layers was detected both in the current-voltage scans and in the optical measurements.

In order to explain the dynamics observed in the devices during the current-voltage scans, we presented a qualitative model describing the bands bending under different conditions. Our model takes account for all the phenomena observed in the electrical and optical characterizations.

Although we made all these observations and models to explain the characterization of a planar structure (IDs), the same phenomena occur in case of vertical structures, which are used in perovskite solar cells. However, these phenomena are less evident in vertical structures, due to the different thickness of the active layer and the different number of grains and boundaries involved in the charge/ion transport.

Remarkably, the damage induced by the dipoles is a relevant problem on vertical as well as on planar structures. Despite the positive improved band alignment that dipoles might induce, the high electric field generated is destructive. Thus, we give a wiser view of the ion migration effects, providing a further demonstration that ionic motion must be suppressed in order to optimize functionality and reliability of PVK materials, extending perovskite solar cells lifetime.

3.3 Effects of thermal stress on hybrid perovskite solar cells with different encapsulation techniques

Section 3.3 is an extracted of the corresponding published paper Ref. J12

3.3.1 Introduction

The high variability of the environmental conditions during PSCs lifetime has several effects on the reliability and stability of the devices. Several encapsulation techniques are available to prevent degradation phenomena, which are boosted by harsh environmental conditions such as high moisture, ultraviolet radiation and extreme temperature variation. In this regard, we analyzed the effects of storage in air and accelerated thermal stress on PSCs encapsulated with two different type of sealing techniques to investigate the contribution of temperature, moisture and humidity on PSCs degradation. We used traditional DC techniques in parallel with transient techniques and fast cycle-voltammetry for a better understanding of cells degradation phenomena.

3.3.2 Methods

We manufactured the cells at the CHOSE laboratory in Rome. The single cell active area is 1.05-cm^2 and it is grown on an Fluorine-doped Tin Oxide (FTO)/glass substrate [94]. The perovskite solution-processed thin-film is deposited by spin coating over a mesoporous titania layer to enable the crystal growth of the $CH_3NH_3PbI_3$ structure. Spiro-OMeTAD is used as hole transport layer (HTL) and Au as anode contact. To study the intrinsic stability of the perovskite solar cell, we used two different glass-to-glass sealing techniques: with (ES-PSC) edge sealing and without (GS-PSC)[113]. Fig. 3.3.1 shows the differences between encapsulation strategies. We sealed both devices (a) and (b) by using a glass-to-glass sealing technique applying a light-curable glue. After that, to protect further the device from moisture and oxygen percolation through the sealing, we used only on ES-PSC an UV-curable glue on the edges of the encapsulation glass (white sealing material on the device (b) in Fig. 3.3.1). We subjected some of the samples to thermal stress applying different temperatures of 40°C, 60°C, 80°C and 100°C, while others were stored in dark in ambient air condition. During the stresses, we kept the devices in the dark without bias.

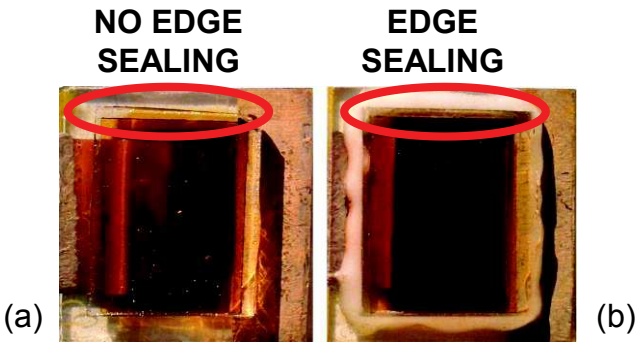

Fig. 3.3.1 Pictures of the samples (a) without edge sealing (GS-PSC) and (b) with edge sealing (ES-PSC).

We periodically stopped the stress to monitor devices degradation by means of transient measurements, fast cycle-voltammetry and slow current-voltage (I-V) both in light and in dark. The last measurement was performed after 400-h storage in the dark for all the devices in order to observe possible recovery phenomena. The transient measurements include the open circuit voltage decay (OCVD) and the applied bias voltage decay (ABVD). The OCVD is a well-known technique, particularly used in DSSCs [117] to determine the charge lifetime and tentatively extended to PSCs [190] in order to appreciate both the charge kinetics and the depolarization timings. The time resolution for the OCVD transient measurements is about 100ms with filling time of 180s and sampling time as long as 500s. Because of the long depolarization timing of the studied devices, we focused only on slow kinetics (~ms to ~s), avoiding the analysis of very fast transient decay (~μs) [178]. On the other hand, the ABVD polarizes the device with an external bias in dark conditions until it reaches the equilibrium. Then, the open circuit voltage transient is measured, with the same timings of the second phase of OCVD. We performed the ABVD by applying an external voltage equal to the measured V_{OC} under 1-Sun illumination. Using the same potential as the voltage generated by the cell under illumination, we replicated similar polarization conditions as during the OCVD. Thus, the voltage decay obtained by OCVD and ABVD are comparable. The cycle-voltammetry measurement consists of a series of fast scan performed sequentially without disconnecting the device, while the stabilized I-V measurements is a single very slow scan, backward and forward. The stabilized current-voltage scan is very slow to allow the device current to stabilize after a constant voltage is applied. This is necessary to obtain an I-V curve without hysteretic phenomena, typical of PSCs. On the contrary, we perform the cycle-voltammetry in order to detect the hysteretic phenomena. Cycle-voltammetry and stabilized I-V are taken from -1.5V in reverse condition to 1V in forward polarization, with ramp-rate (RR) 3V/s and 0.003V/s respectively, both in dark and under illumination. We used a white LED as light source.

3.3.3 Results

In Fig. 3.3.2 we show a comparison of the efficiency η, normalized to its pre-stress value. GS-PSC η is represented with dashed lines while ES-PSC with continuous lines. The average efficiency of all the samples before stress was 10.5%. We notice that for both sealing techniques, the devices efficiency decreases with increasing stress time and only in unstressed cells, we observe no efficiency losses after the 400h-storage step. For both devices, the performance degradation increases with the stress temperature. We distinguish 3 groups of temperatures, each one with a different decay rate. In Group I, we find cells subjected to stress at 40°C or stored at ambient temperature. In Group II, we find cells stressed at 60°C. In Group III there are cells stressed at 80°C and 100°C. Furthermore, we notice that efficiency in ES-PSC devices is generally higher than in GS-PSC when devices are stored or stressed at low temperatures (40°C and 60°C). However, this phenomenon is reversed with GS-PSC, since the latter cells maintained a higher efficiency than ES-PSC at the highest stress temperature (100°C). On the other hand, at an intermediate temperature of 80°C the cells perform similarly during the stress. Fig. 3.3.3 shows the normalized short-circuit current (I_{SC}) measured during the stress. I_{SC} features a similar trend to the efficiency, but with a slower decay rate. However, I_{SC} is almost unchanged (within the 5-10%) with respect to the initial value at storage conditions and low temperature stresses (40°C and 60°C during the first 15h) compared to η.

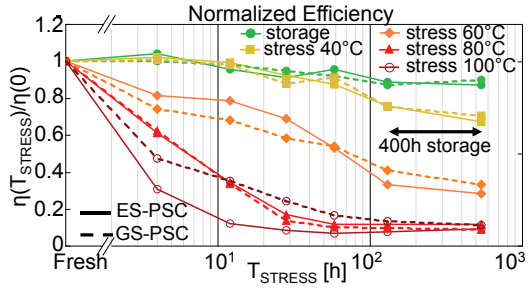

Fig. 3.3.2 Cells efficiency normalized to the fresh value on GS-PSC (dashed lines) and ES-PSC (continuous lines) measured during different thermal stresses and during storage.

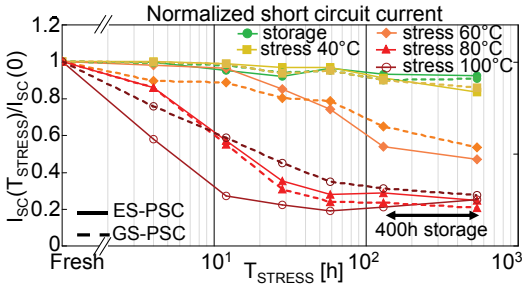

Fig. 3.3.3 Cells I_{SC} normalized to the fresh value on GS-PSC (dashed lines) and ES-PSC (lines) measured during different thermal stresses and during storage.

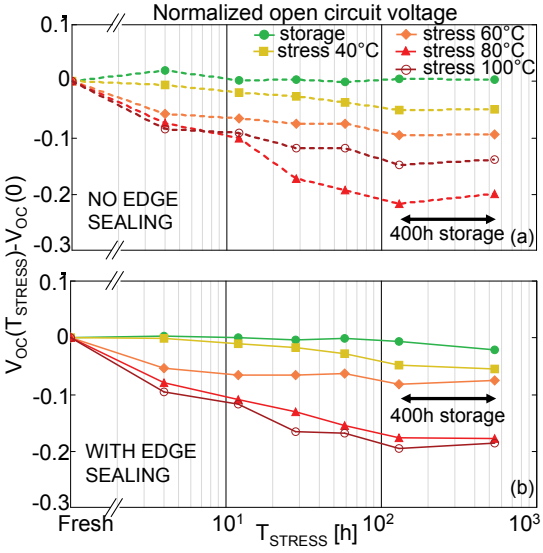

Fig. 3.3.4 V_{OC} (normalized to the fresh value) measured on (a) GS-PSCs and (b) ES-PSCs during the experiment.

Fig. 3.3.4 summarizes the open-circuit voltage for GS-PSC (a) and ES-PSC (b) devices respectively during the whole experiment. In both device types, the thermal stress decreases the open circuit voltage by 0.2V in the worst case. The storage in dark does not affect V_{OC} at least within 538h. In contrast, during the stresses, V_{OC} reduces, even at low stress temperatures. Furthermore, we observe that in GS-PSC, at 100°C, the V_{OC} decay rate reduces when compared with the stress performed at 80°C. On the other hand, this does not occur in ES-PSC, where the decays are similar at 80°C and 100°C. Using the efficiency, the short-circuit current and the open circuit voltage, we calculated the fill factor (FF), which is shown in Fig. 3.3.5 as function of the stress time and temperature. The FF shows s a progressive degradation with increasing stress time and temperature, in a similar way to the efficiency. Remarkably, at the highest stress temperature (100°C) GS-PSC cells degrade with a lower decay rate compared to ES-PSC ones, while during other stresses both cells exhibit a similar behavior.

For a better understanding of the hysteresis phenomenon in perovskite solar cells, Fig. 3.3.7 reports an example of cycle-voltammetry both in dark (a) and under illumination (b). The cycle-voltammetry performed in dark shows some hysteresis only at forward bias due to the charge injected and trapped inside the solar cell. On the other hand, the same measurement under illumination gives a hysteretic behavior at all the measured voltages due to photo-generated carriers.

Fig. 3.3.6 shows the area of the hysteresis normalized to its pre-stress value, calculated during a stabilized cycle under illumination of the cycle-voltammetry for both stressed and stored cells. We notice that the hysteresis decreases in both stored and stressed devices. Noticeably, the hysteresis variation during storage and stresses at low temperatures (40°C and 60°C) is within 15%. On the other hand, increasing the stress temperature highly affects the hysteresis, reducing up to 75% its area. Fig. 3.3.8 shows an example of the OCVD measurement used to characterize the devices.

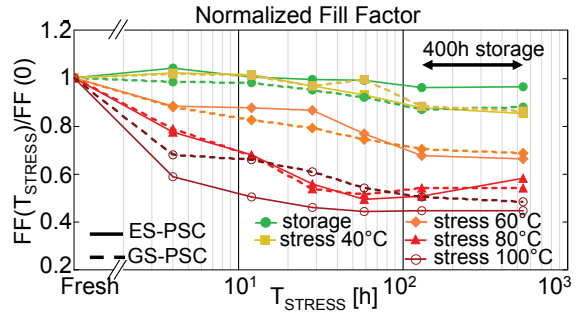

Fig. 3.3.5 FF normalized to the fresh value measured on GS-PSCs (dashed lines) and ES-PSCs (continuous lines) during the experiment.

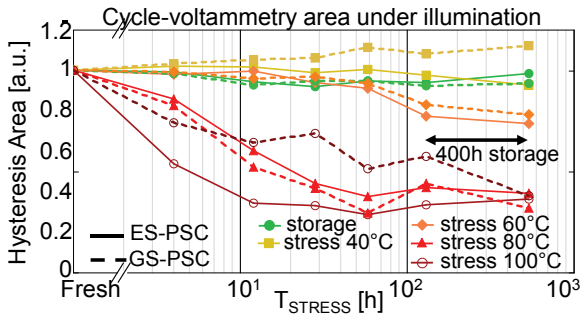

Fig. 3.3.6 Hysteresis area calculated from cycle-voltammetry during the experiment on GS-PSC (dashed line) and ES-PSC (continuous line).

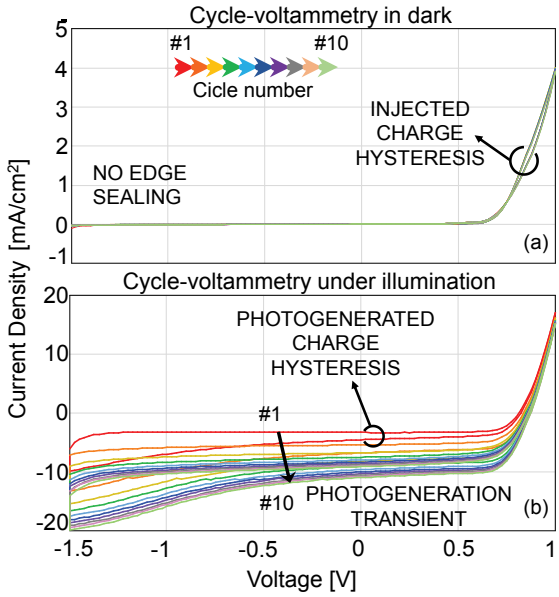

Fig. 3.3.7 Example of cycle-voltammetry on a type GS-PSC both in dark (a) and under illumination (b).

Our focus during the stresses is on depolarization kinetics related to the ion migration generating the slow decay occurring on the timescale of seconds. Analyzing the initial voltage of OCVD (within the first few ms) we detect charges lifetime and recombination rate variations related to fast phenomena in the device (~µs). Nevertheless, it is not possible to correctly estimate the decay constants. We observed in almost all the stressed devices that with increasing stress time and temperature both the fast and slow decay accelerates, reducing the initial voltage detected with the first OCVD sample and the time required reaching the equilibrium. Finally, Fig. 3.3.9 shows as an example a comparison of an ABVD and an OCVD taken on a device polarized at equivalent bias conditions. The two measures overlap, leading to the same curve and this behavior is independent on the device and stress conditions. For this reason, we decided to use OCVD as the reference measurement to analyze voltage decay kinetics at open circuit conditions.

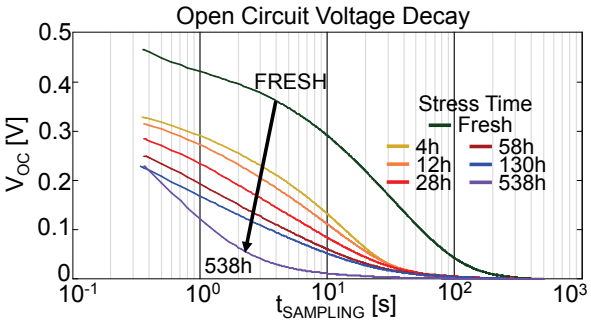

Fig. 3.3.8 OCVD measurement performed on one of the ES-PSC stressed at 100°C.

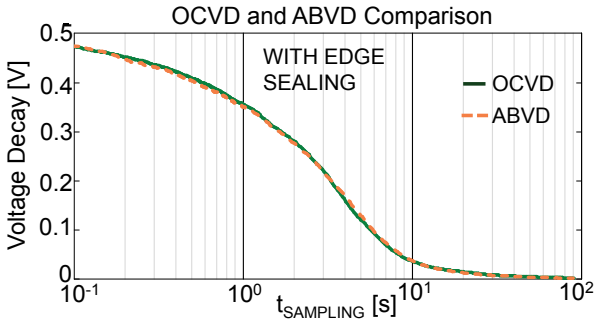

Fig. 3.3.9 ABVD and OCVD performed on an ES-PSC polarized at the same bias conditions.

3.3.4 Discussions

Both ES-PSC and GS-PSC efficiency degrade with increasing stress time and temperature. We suggest that three processes are related to performance decays: the oxidation of the TiO_2, the undoping of the Spiro-OMeTAD and the wetting of the perovskite in particular close to the edges. Specifically, we consider the HTL degradation to be one of the main reason behind the performances loss, due to the dissociation of doping elements (TBP and Li-TFSI) from the Spiro-OMeTAD and to its crystallization. Indeed, comparing Figs. 2 and 3, we notice that a huge efficiency decay occurs after the first stress step (70% loss at 100°C ES-PSC), while this does not replicate in the I_{SC} evolution (about 40% loss during the same stress). The extracted I_{SC} is related to the perovskite layer performances; I_{SC} losses are lower compared to efficiency decay, when the devices are stressed at low temperatures or for short times. This phenomenon is the signature of an appreciable increase of the series resistance and thus a decrease of the fill factor (Fig. 3.3.5) and efficiency (Fig. 3.3.2). It has already been proven how Spiro-OMeTAD degrades with high temperature [108,113] and our experiments are in agreement with those results, showing that one major problem behind efficiency decay is related to charge transport and extraction rather than to perovskite degradation (clearly observable by I_{SC} analysis).

Both ES-PSC and GS-PSC degrade during the experiment; however, there are some differences in the degradation curves. Storing or stressing Group I affect similarly the devices, both ES-PSC and GS-PSC. The efficiency decay is at most 10% within 58h. Only after 100h 40-°C stress, the temperature induces a faster decay compared to stored devices, mainly due to FF and V_{OC} variations rather than I_{SC} decay. Because these cells are stable when stored in dark [113], we ascribe part of the efficiency drop during the experiment to the measurement process itself, that requires a long time due to very slow stabilization kinetics of perovskite solar cells. Thus, we estimated that 10% of the devices efficiency loss within 130h experiment is due to the measurements, at all stress temperatures. Observing the cells of Group II, we notice that the edge sealing helps maintain a higher efficiency within 28h of stress with respect to GS-PSC. However, by increasing the stress time, the decay rate enhances in ES-PSC compared to GS-PSC. Similarly, Group III shows an inversion in the trend, with GS-PSC performing better than or equally to ES-PSC during the stress. In particular, with the highest stress temperature (100°C), the additional sealing becomes counterproductive. The absence of sealing helps in keeping high performances when the cells are stressed at 100°C. This indicates that the additional glue on the edges works as a protective layer at low temperatures and short times but may be detrimental at high temperature and long exposure.

We tentatively relate this unexpected behavior to two possible reasons. 1) The edge-sealing glue solvent may evaporate and percolate trough the sealing damaging the device. This process is almost negligible during storage or low stress temperature, but becomes relevant with longer exposure or increasing temperature. 2) The additional sealing changes the oxygen interaction with the perovskite and the Spiro-OMeTAD layers, modifying the oxygen percolation through the encapsulation. Indeed, as already shown in the literature [109,191], oxygen plays an important role in perovskite solar cells, both in the realization process and efficiency degradation. High temperatures may induce different phenomena in the perovskite layer possibly related to the percentage of oxygen present in the device. Changing such concentration with the additional edge sealing may lead to different mechanisms within the device, partially responsible for the degradation rate reduction. However, further studies are required to establish the reasons behind the observed differences.

Visual inspection of the perovskite layer close to the edges (e.g. Fig. 3.3.1) shows that edge sealing reduces the moisture percolation through the encapsulation: dark and smooth on ES-PSCs, more jagged and yellowish on GS-PSCs.

This indicates that while in ES-PSCs the edge sealing prevents the moisture from damaging the perovskite, in GS-PSCs a degradation occurs on the edges. Despite these differences, both sealing techniques help maintaining the cells performances, when they are stored for long time in dark without previous stresses.

Both ES-PSC and GS-PSC show a monotone V_{OC} decay with stress time (see Fig. 3.3.4). On the other hand, devices stored in dark undergo minimal variations of the open circuit voltage. This phenomenon leads to a continuous increase of the internal recombination rate with increasing stress time and temperature. The observation is in agreement with results obtained comparing FF, I_{SC} and η. After the first stress step, where the degradation of the transport layers (Spiro-OMeTAD in particular) is the main responsible for the performance reduction, we suggest that processes occurring within the perovskite layer compete equally with HTL degradation to efficiency losses. The irreversible decomposition of perovskite cations may diminish the internal polarization [119] that helps charge splitting, thus lowering the free carriers and the open circuit voltage measured.

The fast cycle-voltammetry and OCVD further confirm the increasing cation degradation hypothesis. According to the literature [119], the hysteresis detected by the fast current-voltage scan diminishes with both trapping or ion migration reduction. In addition, OCVD points to a reduction of the time scale of the slow kinetic. This kinetic is related to the time that ion migration takes to reach equilibrium. Analyzing the correlation of OCVD and cycle-voltammetry, we tentatively conclude that the variation of mobile ionic species migrating within the device [119] is one of the major contribution increasing the charge recombination rate in the perovskite.

Analyzing ES-PSC and GS-PSC cycle-voltammetry hysteresis with stress time (Fig. 3.3.7) and comparing the two sealing techniques, we notice no appreciable differences, unless the stress temperature is 100°C. During the stress at the highest temperature, the area enclosed by the fast current-voltage scan follows a much slower decrease in GS-PSC compared to ES-PSC. Attempting an explanation to such a phenomenon, we suggest that the same processes that reduce the I_{SC} and V_{OC} decay rate at high temperature are also responsible for the slower hysteresis area decrease. These processes relate to the perovskite layer degradation with high stress temperature. Some sort of annealing occurs within the perovskite layer with high stress temperature; annealing that competes with degradation processes. However, further investigations are required to fully understand such phenomenon.

From all of these considerations, we can state that edge sealing improves cell lifetime and durability, except at the highest stress temperature of 100°C. Improving perovskite resistance to moisture and oxygen percolation, edge sealing reduces contribution of the processes concurring to the solar cell degradation at moderate stress temperature. On the other hand, at high stress temperature (above 80°C) we observe an inversion in the degradation trend, with GS-PSC keeping higher performances compared to ES-PSC, at least within 130h of thermal stress. Finally, we observed that storing unstressed devices in dark does not affect performances.

3.3.5 Summary

We performed storage and thermal stresses on solid state solar cells based on organometal perovskites using Spiro-OMeTAD as hole transport material and encapsulated using two different sealing techniques. Both stresses and simple storage induced degradation on the samples, lowering efficiency, short-circuit current, open-circuit voltage and fill factor. Storing devices in dark leads only to small performances loss mainly due to the measurement process itself, while thermal stress generated increasing damages to the device.

Edge sealing results to be a better approach to reduce moisture percolation and oxidation mechanisms at least at stress temperatures below 80°C, resulting into an increased lifetime. On the other hand, at high stress temperatures the additional sealing becomes counterproductive and accelerates the performances decay. However, further investigation is necessary in order to fully understand the kinetics and dynamics occurring within perovskite solar cells exposed to thermal stresses. In conclusion, by coupling thermal stress and electrical measurements, we detected and distinguished at least two possible sources of degradation that can give insights into the understanding of losses mechanisms of perovskite solar cells.

4 Lifetime of organic and hybrid solar cells

The novel PV technologies, such as polymer photovoltaic (OPV), perovskite PV (PVSK) and dye sensitized solar cells (DSSC) represent a low-cost and eco-sustainable alternative to conventional solar cells and may therefore revolutionize the PV market in the near future.

In order to prove that OPV can become competitive in the photovoltaic market, it is of the outmost importance to demonstrate that OPV is competitive in terms of cost, efficiency and reliability [192]. Although it has already been proven that OPV scalability can be easily extended [193–197], with low resource claims and at low cost, significant research is still required to improve efficiency and stability [19,21,23]. Improving OPV efficiency to 5% with 5 years lifetime would bring the cost of electricity generated by this technology on a level that would challenge the fossil fuels [194]. Although today's lab scale OPV reach 10-12% and recent studies proved that overcoming the 5% efficiency limit is possible on large modules [198–200], the optimization of lifetime is still lacking behind [201,202].

In order to improve and demonstrate the lifetime and stability of OPVs it is necessary to set standards for testing the stability. Due to the structural and material differences between OPV and inorganic technology the existing standards for inorganics technology are not applicable for OPVs [192]. Thus, a fair comparison of the stresses performed in different laboratories with different custom setup is usually hard to reach for such technologies [203]. Indeed, not only the different stress procedure but also the large variability of devices structure and polymers/materials result in several different ageing mechanisms. Modeling the ageing behavior of organic solar cells using mathematical approach is therefore rather difficult.

In this chapter, we present a possible approach to evaluate and estimate the lifetime of novel PV technologies.

4.1 A novel algorithm for lifetime extrapolation, prediction and estimation of emerging PV technologies

Section 4.1 is an extracted of the corresponding published paper Ref. J13

4.1.1 Introduction

In 2011 at the International Summit on OPV Stability (ISOS) the first step toward standardization of lifetime testing was done [29], and guidelines were established for stability testing of organic solar cells, that each laboratory could refer to [204]. The guidelines were aimed to give a tool for performing harmonized and comparable lifetime data. In the guidelines, both indoor and outdoor tests with different illumination and moisture-controlled conditions were included. ISOS helped eliminating the challenges related to diversity of equipment and test conditions used among different laboratories.

Nevertheless, the lifetime data obtained from such ISOS tests could still vary a lot in shape and behavior, depending on the device structure and the applied materials. Therefore, two parameters were suggested for the definition of the lifetime: T_{80} - the time when the sample degrades to 80% of its initial value E_0, and T_{S80} – the time when the sample degrades to 80% from the performance value E_S at a random T_S point chosen by the experimenter (normally used to describe the more stabilized second phase of ageing) [205]. Since however the random choice of T_S value may introduce some incomparability among different laboratories, as a complementary to ISOS guidelines a new method for calculating lifetime was suggested in a study published in 2015 [206]. It was proposed that T_{80} is calculated as the 80% of the maximum reached performance, while T_S is chosen such that the energy produced in the window between T_S and T_{S80} is the maximal within the lifetime of the sample. An additional condition for reliable choice of T_{S80} is that the efficiency at T_S should not be lower than the 50% of the maximum efficiency that the cell has reached through the course if its lifetime.

We introduce an algorithm that allows an easier extrapolation of the defined T_{S80} and T_{80} using the set of rules described above [206] and enables the prediction of the lifetime in the case when the experimental data is incomplete (T_{80} or T_{S80} have not been reached). With the automatic determination of the lifetime values the algorithms also reduces the human error factor leading to the harmonization of the lifetime determination process. While the discussion and the described experiments in this section are based on the OPV technologies, the presented thoughts and tools are equally applicable for the other emerging PV.

The presented algorithm is the first version and therefore contains certain drawbacks. However, the overall performance of the algorithm is not impaired and therefore, we choose to present it together with highlighting all the drawbacks and offering optimization steps for any new versions to be developed.

4.1.2 Methods

In the following we recall the lifetime marker definition given in earlier study [206] and we describe the main sources generating noise in data, the algorithm structure and the software environment adopted for implementing it.

4.1.2.1 Lifetime Marker

Short summary of the definition of lifetime markers given in [206] is discussed here and summarized in Tab. 4.1-A, while for more details the reader is referred to the earlier publication. Fig. 4.1.1a shows typical examples of ageing curves for OPV reprinted from the earlier publication [206], that often evolve with a linear or exponential behavior. Curve 1 represents one of the most common decay shapes (the so called "hockey stick") with initial rapid ageing followed by stabilized phase, while curves 2-5 describe other often-recorded behaviors for OPVs. The published study offers a set of rules for approaching each curve type in order to determine the lifetime. In particular, if the curves shows initial increase, then the starting point for ageing is shifted to the maximum value and named E'_0 and the T_{80} initial lifetime parameter is calculated from the new point T'_0 (see curve 3 in Fig. 4.1.1a). Meanwhile T_S is chosen such, that the energy produced in the period T_S-T_{S80} (the grey area marked with II in Fig. 4.1.1b) is the maximal. Boundary conditions to the latter rule is that E_S value at T_S must not be less than half of maximum value E_0 (or E'_0). The procedure for the identification of such time windows is explained in detail in ref. [206] and also summarized in Tab. 4.1-A. Furthermore, one can eventually choose the single best parameter between T_{80} and T_{S80} to describe the lifetime of the cells depending on whether the largest amount of energy is produced in the first phase of ageing T_0-T_{80} or the second T_S-T_{S80} (grey area I or II in Fig. 4.1.1b respectively).

Due to such a variety of curves, it is rather challenging to develop a model that would simulate the diverse behaviors of organic PV. Nevertheless, in the following sections, a method is presented that with a limited but sufficient accuracy defines lifetime parameters for different ageing curves.

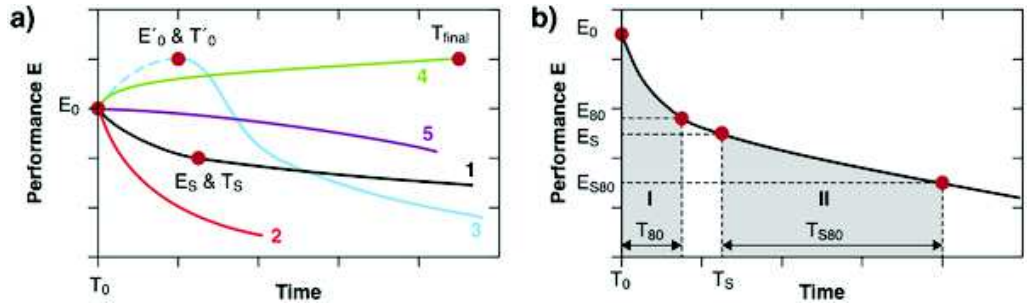

Fig. 4.1.1 a) Examples of various shapes of aging curves taken from real data. b) Example of identifying the best pair describing the stability of the sample. Reproduced with permission from [206].

Parameters	Method
Determination of starting point E_0 & T_0 E_0 – initial performance T_0 – initial time	T_0 & E_0 pair is either chosen at the first measurement point, or if the curve has an initial increase followed by a reduction (such as the curve 3 in Fig. 4.1.1a) then T_0 & E_0 is set at the maximum point.
Determination of stabilized section E_S & T_S E_S – performance at the start of stabilized section T_S – starting time of stabilized section	If after a certain point the aging curve enters into a more stable phase (commonly observed during solar cell aging), then a second pair of starting values T_S & E_S is identified, typically chosen at a point from where the aging rate almost doesn't change anymore, as shown on curve 1 in Fig. 4.1.1a.
Determination of T_{80} and T_{S80} T_{80} – time when performance reaches 80% of E_0 T_{S80} – time when performance reaches 80% of E_S	T_{80} (or if applicable T_{S80}) is determined by subtracting T_0 (or T_S) from the time when 80% of E_0 (or E_S) is reached. Fig. 4.1.1b highlights the areas determined by T_{80} and T_{S80}.
Lifetime marker [E_0;T_{80}] or [E_S;T_{S80}]	The largest area among I and II in Fig. 4.1.1b (part of the curve where the cell produces the largest amount of energy) will determine the pair that will describe the lifetime.
Exceptions	Exceptions are made in the following cases: • If E_S is less than half of E_0, in which case the sample is considered to have degraded before stabilization (see curve 2 in Fig. 4.1.1a), then [E_0; T_{80}] is chosen by default to represent the lifetime. • [a]If the measurements has been stopped prior to reaching the 80% threshold then "T_{Final} - T_0" or "T_{Final} - T_S", where T_{Final} is the point of last measurement (see curve 4 in Fig. 4.1.1a), is chosen instead to represent the minimum possible lifetime.

Tab. 4.1-A The list of steps for determining the lifetime marker. Reproduced with permission from [206].

[a] This kind of exception can will be easily avoided by applying the algorithm

4.1.2.2 Noise Sources and Data Variation

While determination of lifetime markers, described in the previous section, may be somewhat trivial for smooth curves such as the ones presented in Fig. 4.1.1a), it is well know that often the curves contain certain noise in forms of spikes or temporal deviation of the ageing from its course and this can significantly complicate the process of lifetime determination. Common examples of such noises are depicted in Fig. 4.1.2, where the data was acquired from cells exposed to indoor light soaking using automated measuring setup. Fig. 4.1.2 shows three common forms of outliers:

Spikes, which are often a result of electrical interferences in the data acquisition setup and are typically very short and random;

Longer period break down, typically resulting from an unexpected break down of the light source;

Change in conditions, where the data unnaturally deviates from its ageing course typically due to a change in the test conditions, such as increase of room temperature.

All these noises can also happen due to weak contacts in the test sample itself. While developing an algorithm for determining lifetime data, it is of high importance to filter out such data deviations to avoid erroneous lifetime predictions. Therefore, as will be discussed in the following sections, a significant part of the algorithm is devoted to filtering out any possible noises in the curve before extracting the lifetime values. However, one has to keep in mind that the acquired data has to be sensible enough, such that the ageing course is easily identifiable despite the noises or else even the best filtering algorithm will not be able to distinguish between real data and outliers.

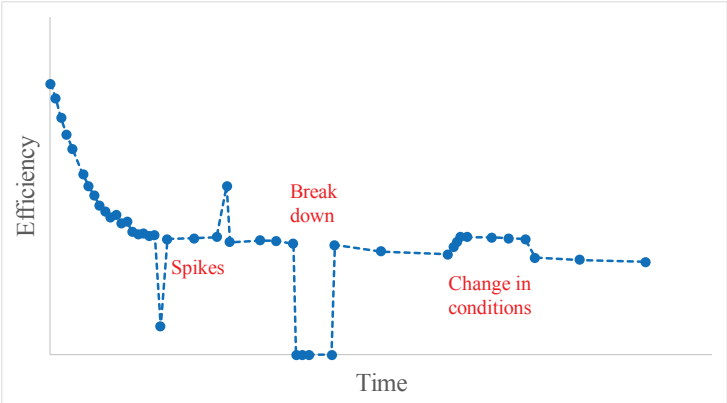

Fig. 4.1.2 A typical aging curve of a measured OPV device with common measurement or device failures. The failures are expressed in forms of spikes, longer period break downs or step like deviation from the course of ageing commonly due to change in conditions of testing (such as temperature elevation in the setup).

4.1.2.3 Algorithm Structure

The algorithm is generally based on the idea of filtering the outliers from the measured lifetime data and applying the best suitable fitting function to the curve in order to accurately determine the lifetime.

Algorithm Tools

MatLab® software was utilized for developing the algorithm. In particular, we adopted certain functions that allowed quickly developing the algorithm in a working program. Among the most important ones, we cite the functions:

"*Hampel*": this function calculates the moving average (μ) and standard deviation (σ) over n values within a vector of length m, where $n \leq m$. During the moving averaging processing, if the value in the central element in the n sub-vector differs by more than $k\sigma$ from μ, where σ is the standard deviation and k is a user defined constant, the filter clamps the outlier to the average μ [207].

"*Fit*": given a specific function, generates the best fit on curve/surface by tuning the function parameters in order to minimize the square mean root error. The functions we used in order to predict the lifetime behavior of the cells were: "*poly1*" a polynomial of the first order (a straight line), "*exp1*" a single exponential and "*exp2*" double exponential.

We adopt the "*Hampel*" function because in our opinion it is the simplest method based on statistical analysis that allows outlier detection. Despite alternatives [208] exist, the method implemented by the "*Hampel*" function has the advantage of detecting and removing outliers minimizing computational duty, complexity and end-user interaction.

The reason we chose the three simple functions described above was because all the ageing curves could be fitted with one of them, while the attempt of using more complex (higher order) functions led to unrealistic scenarios during data extrapolation. In addition, most of the physical and chemical ageing mechanisms typically resemble the aforementioned simple functions.

Web Interface

In order to upload data into an algorithm for processing and acquire the results a webpage was developed, which is hosted at plasticphotovoltaics.org. It allows the users with access credentials to upload the acquired data into an online form, by copying their data in the available tables. Once uploaded the data will asynchronously be processed by a dedicated calculation server using the algorithm and the results will be emailed to the user. The data is also stored in a database sorted according to additional information provided by the user (such as date, sample type, user name etc.), so that comparisons of multiple datasets are possible at any stage. The asynchronous nature of the process makes sure any number of users can submit data at any given time; the server then carries out the calculation sequentially. The advantage of the online platform is that it enables data uploading and processing from everywhere at any time.

Algorithm

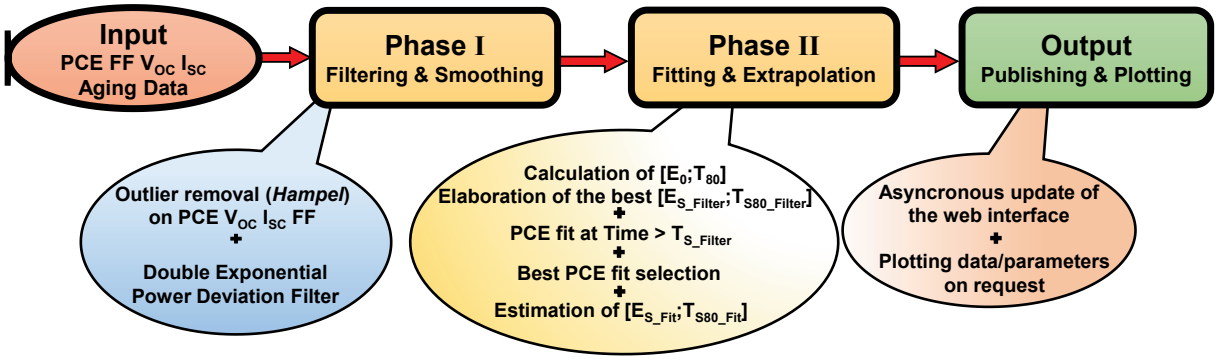

Scheme 4.1.1 Data processing flow diagrams representing the different phases of the algorithm. Each sub-section is magnified in order to describe the main processes executed within it.

Scheme 4.1.1 represents the flow diagram of the algorithm. The algorithm elaborates the data in two consecutive phases, followed by the output of the estimated lifetime parameters. The algorithm requires an input of the ageing data for all four photovoltaic parameters PCE, fill factor (FF), open circuit voltage (V_{OC}) and Short Circuit Current (I_{SC}) for data filtering purposes. The list below outlines the set of the steps that algorithm processes for determining the lifetime from an ageing curve.

Phase I – cleaning and filtering the measured data by removing outliers

Columns of PCE, FF, V_{OC} and I_{SC} versus time are inserted in an online platform (described in Section 4.1.2.3) that transfers the data into a server where algorithm processes the data

Algorithm first checks and eliminates data rows where FF is above 100% or is negative (typically, data points that result in spikes due to some electrical noises in the measuring setup)

Hampel outlier removal function is then applied on PCE, FF, V_{OC} and I_{SC} in order to remove the spikes that are far from the local average [209]. *Hampel* calculates the local average μ and the standard deviation σ for a defined number of adjacent data points called number of samples.

Hampel then clamps to the local average value all the outliers that deviate by more than $k\sigma$ as described in previous section, where k is defined by the user. The filtering process is repeated 3 times using 7 samples with k value changing from 2 in the first run to 0.2 in the second and to 0.1 in the third run for the V_{OC}, I_{SC} and FF. For PCE the k values are 3, 2 and 1 correspondingly with 7 samples during the first two runs and 3 samples during the last one. The choice of the number of iterations and the parameters represents a trade-off between noise rejection and data reliability. Fig. 4.1.3 shows some examples of the different cases. Curve 1 represents the real data after the FF check. Exceeding the number of samples and too restrictive standard deviation clamping values may lead to the creation of unrealistic curves (Curve 2). On the other hand, choosing a suitable number of samples for the moving average but an excessively wide clamping value may not effectively filter the noise in the data (Curve 3). Tab. 4.1-B summarizes the number of samples and k values used to obtain filtered Curves in Fig. 4.1.3. Finally, in Curve 4 the algorithm reaches a good noise rejection by applying several iterations and changing the filter parameters according to values described above. While the chosen parameters work well for a large range of data with reasonable frequency of measurements, the parameters may have to be adjusted

upon drastic change in the frequency of the measurements. With fast decay performances or too low frequency of measurements, it is necessary to choose wider clamping factors to avoid an excessively smoothing of the data. Further versions of the algorithm should involve automatic detection of the frequency and number of data points and self-correction of the set parameters.

Algorithm then performs a further check on the data validity by exploiting the V_{OC} and I_{SC} values. A double exponential fitting function is applied to the product V_{OC}*I_{SC} in order to detect any larger amount of outlier data, such as in the case when the light source is turned off for long period during the tests. The algorithm identifies and eliminates any such data points that deviate from the fitted curve by a certain deviation factor defined by the user. In this case, the applied deviation factor was in the range of 0.5. Currently, the limitation of the algorithm is that only double exponential function can be utilized in this step. However, the analyzed data sets show that the double exponential function is a good choice. Indeed, using two exponentials we can easily fit both double and single exponential as well as linear decays, as it is the case in Fig. 4.1.4. Nonetheless, further versions of the algorithm should involve adding the possibility of choosing different fitting function depending on the curve shape.

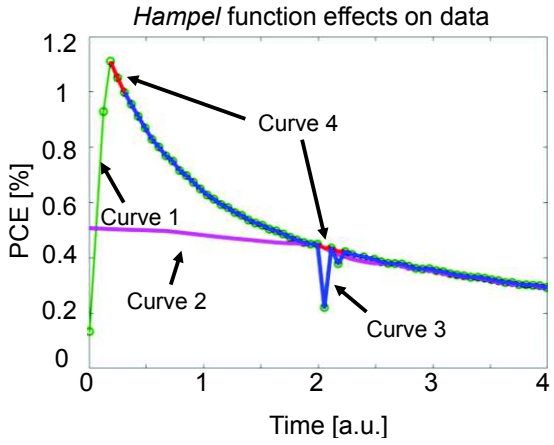

Fig. 4.1.3 Examples of the Hampel outlier remover effects. Curve 1 represents the real data after the FF check. Curve 2 shows an excessive use of samples for the moving average and exaggerated strictly constrains on the maximum deviation from the average for the clamping settings. Curve 3 describes the case of an application where the filtering is not good enough to remove the spiky points. Curve 4 shows a proper filtering obtained by correctly tuning the Hampel filter parameters.

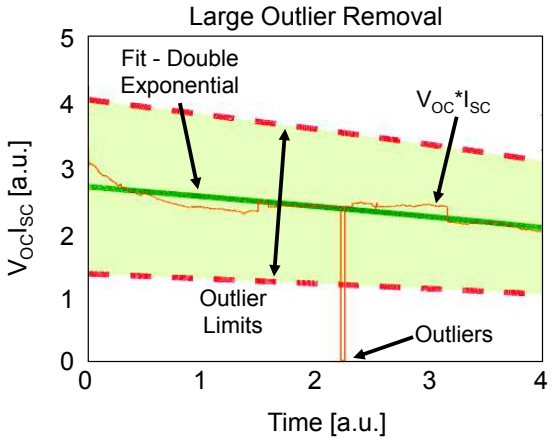

Fig. 4.1.4 Example of the large outlier cluster removal filter application. The Filter removes data falling outside the green valid zone enclosed by the outlier limits (red dotted line). This example proofs that the double exponential can successfully fit linear as well as single and double exponential decays.

Curve	Iteration 1		Iteration 2		Iteration 3	
	# Samples	***k***	**# Samples**	***k***	**# Samples**	***k***
2	61	0.03	61	0.02	21	0.01
3	21	3	21	3	21	3
4	7	3	7	2	3	1

Tab. 4.1-B Number of samples and values of k used during the Hampel iterations on PCE data to obtain filtered curves showed in Fig. 4.1.3.

Phase II – determination of lifetime markers

After Phase I, the algorithm forwards filtered data to Phase II, which carries the following steps:

Each individual data point on the PCE curve is chosen as a starting point and T_{80} value is determined at the point when the curve intersects the 20% degradation mark from the chosen starting point. The step is carried out for all the points on the curve until the 20% degraded value is beyond the final measured value T_{Final}.

For all the determined T_{80} values, the corresponding energy produced by the solar cell sample is calculated, which is the area under the ageing curve defined by the corresponding T_0-T_{80} time range (see for example the grey areas in Fig. 4.1.1b). The chosen starting point, for which the corresponding energy is the maximum, is defined as the T_{S_Filter} stabilizing point.

The algorithm then defines:

E_0 (PCE at the starting point or at the maximum PCE value if the curve initially increases before starting to decline)

T_{80} lifetime calculated for E_0 value

E_{S_Filter} (PCE at T_{S_Filter} point)

T_{S80_Filter} stabilized lifetime calculated for E_{S_Filter} value

Then the algorithm takes the data in the range T_{S_Filter}-T_{Final} and applies the fit function, described in Section 4.1.2.3 and determines the best fitting function based on the minimal square mean root error. The importance of applying fitting functions to the data is to double check the accuracy of filtering. The reason the function is applied only to the section of the curve starting from T_{S_Filter} value is because the section before T_{S_Filter} is typically very dynamic and therefore the fitting of the functions leads to rather large square mean root errors.

The fitted function is then extrapolated to $T_{limit} = 1.5 *(T_{Final}-T_S) + T_S$, which is useful in case the sample did not degrade by 20% within the measurement period. Limiting the extrapolation by only 1.5 times is useful in order to keep the predicted section of the curve reasonably close to realistic scenarios.

The fitted function (in the range T_{S_Filter}-T_{limit}) is combined with the measured data in the range T_0-T_{S_Filter} and *Hampel* function is applied to the total data to assure the combination of the two is smooth.

Similar to the process made for the measured data T_{80} lifetime value is calculated for every data point of the fitted curve until the 20% degradation point is beyond the T_{limit} value and new T_{S_Fit} point is defined based on same criteria of maximum energy. Based on determined T_{S_Fit} value E_{S_Fit} and T_{S80_Fit} are identified.

Output

Algorithm then produces a row of the following lifetime data:

E_0, T_0, T_{80} for initial part of measured data

E_{S_Filter}, T_{S_Filter}, T_{S80_Filter} for stabilized part of measured data

E_{S_Fit}, T_{S_Fit}, T_{S80_Fit} for fitted data

The corresponding energy values $Energy_0$, $Energy_{S\_Filter}$ and $Energy_{S\_Fit}$ (the areas under the ageing curve defined by the corresponding T_0-T_{80} time ranges).

Algorithm additionally publishes two plots on the website described above. Fig. 4.1.5 shows an example of the plots. The first plot presents the measured data and the data after filtering, as well as highlights the determined lifetime parameters and the corresponding energy values (area under the curves defined by the lifetime values). The second plot shows the measured data with the fitted curve and highlights the lifetime parameters and energy values of the fitted curve. Finally, a table containing all the lifetime data is additionally printed. This allows easily assessing the accuracy of filtering process and the determined parameters. It also allows choosing the best pair between the measured and fitted lifetime parameters for describing the lifetime of the sample, although in almost all the cases the fitted data produces the most accurate prediction of lifetime. In the results section a set of examples is presented of the processed data and plots.

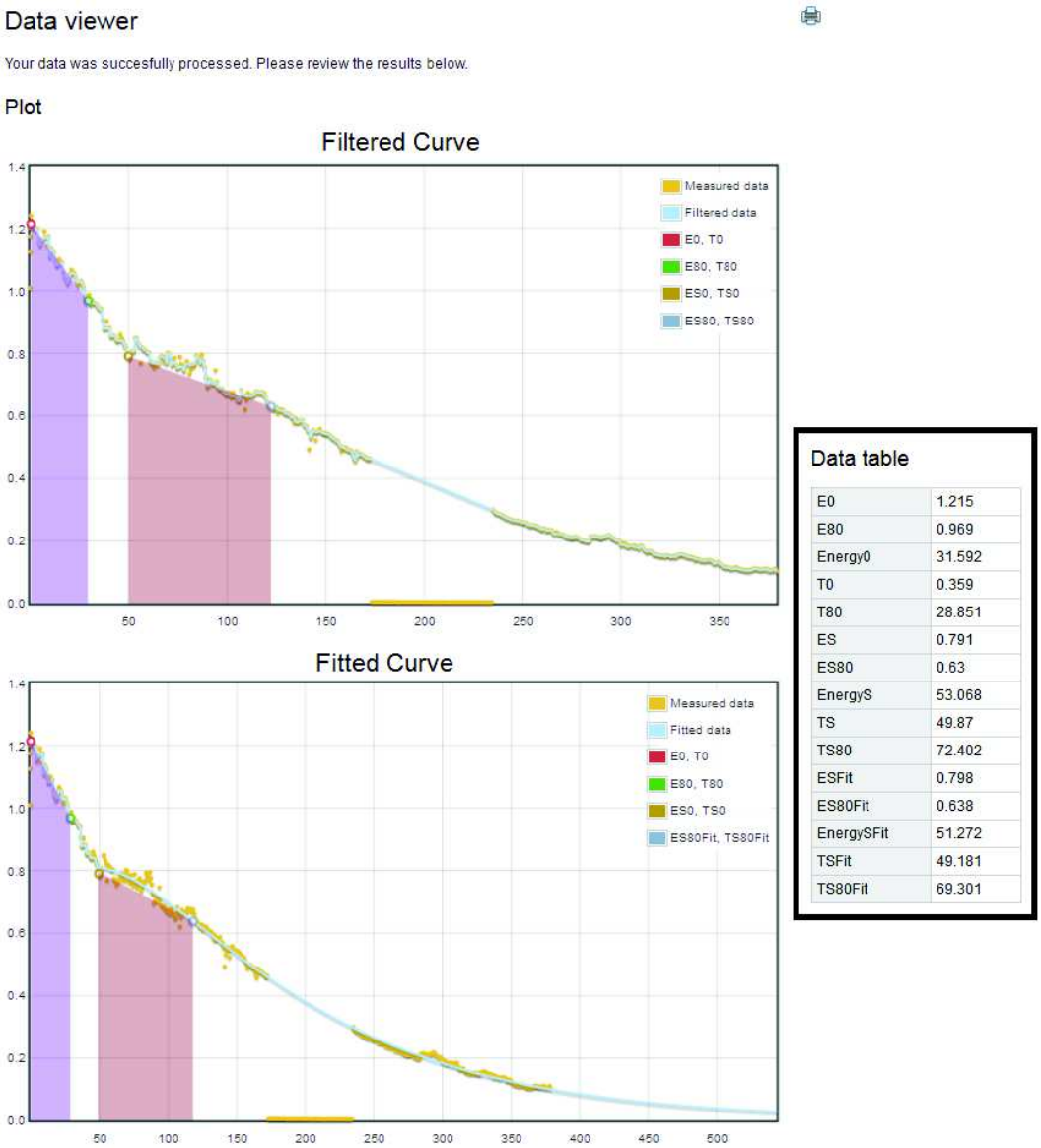

Fig. 4.1.5 Print screen picture of the results plotted on the web interface (http://plasticphotovoltaics.com). X-axis represent the time value and y-axes PCE value. Both plots show E_0, T_0, T_{80} in comparison with the output obtained from filtered data E_{S_Filter}, T_{S_Filter}, T_{S80_Filter} in the upper window, or the E_{S_Fit}, T_{S_Fit}, T_{S80_Fit} in the lower picture resulting from the fitting procedure (E stands for PCE).

4.1.3 Results and Discussions

4.1.3.1 Data Analysis

It is important to emphasize that all the stability data used for experimenting the algorithm features are based on ageing of commonly used P3HT (Poly(3-hexylthiophene-2,5-diyl)): PCBM (Phenyl-C61-butyric acid methyl ester) based roll coated OPV devices. The fill factors and efficiencies of such freshly prepared devices are in the ranges of 55 to 60% and 1 to 2% respectively, which is close to the average performance for such devices [202]. Thus, the samples are good representatives for such studies. Fig. 4.1.6 O-graph [206] illustrates the differences of E_S and T_{S80} markers obtained from filtered and fitted data on a considerable number of different samples. Black circles represent markers calculated from Ph. I data while stars from Ph. II. We underlined an increase in the lifetime T_{S80} obtained from the fitting process in light blue. On the other hand, we used purple stars in the opposite case. Observing the diagram, we notice that fitted markers tend to result in shorter T_{S80} and higher E_S values compared to the filtered ones. Indeed, the number of purple stars is considerably higher than light blue ones and purple markers show a higher PCE value compared to the corresponding filtered markers. The reason filtered data in most case will lead to longer lifetimes compared to fitted data is because despite the filtering process the curve may still contain sudden bumps and recessions (see for ex. Fig. 4.1.5). The algorithm is set up such that it will always look for the section of the curve where the largest energy is produced and will calculate the lifetime in that section. Since in the filtered data there are many peaks, which artificially increase the produced energy, this prolongs the lifetime compared to the fitted data, where the curves is rather smooth and is free of peaks. The effect of the peaks in the filtered data becomes also more pronounced at the more stabilized part of the curves and therefore, the lifetime window with the largest energy will normally shift towards these sections for filtered data and will therefore have also lower starting point E_S compared to fitted data. This situation results into a T_{S80} overestimation, while lowering E_S.

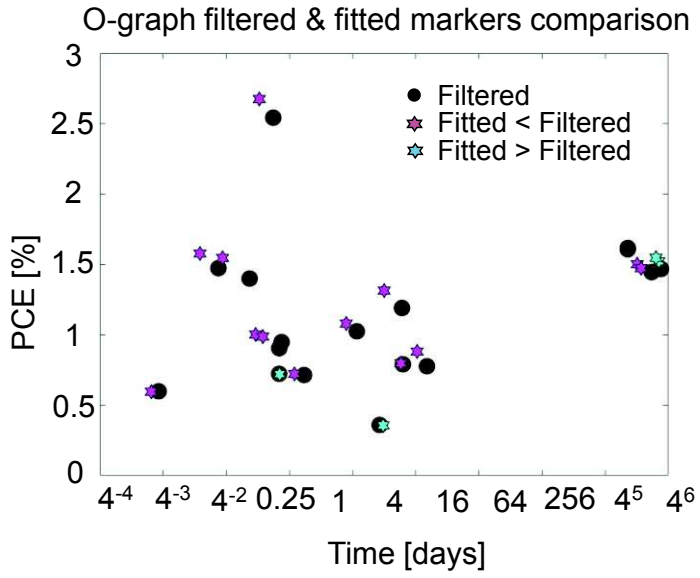

Fig. 4.1.6 O-graph representing the difference of filtered and fitted lifetime parameters: E_S on PCE axis and T_{S80} on Time axis. Markers obtained from filtered data are in black circles, while stars represent markers resulting from fitting Ph. II. We underlined an increase of the marker T_{S80} calculated on Ph. II compared to the corresponding marker resulting from Ph. I data with a light blue color, while a decrease is indicated by the purple star markers.

In these cases, of course it is important to compare the results with the fitted curve, which normally filters out all the sudden bumps and recessions and therefore delivers the most accurately determined lifetime values.

Fig. 4.1.7 provides some examples of data processed by the online platform discussed above. This tool plots two graphs per each incoming lifetime data set: the first one with PCE resulting only from filtering (Ph.I) (Fig. 4.1.7a, Fig. 4.1.7c) and the second one with fitting (Ph. II) processed data (Fig. 4.1.7b, Fig. 4.1.7d). Tab. 4.1-C summarizes the energy and lifetime markers estimated for all the devices shown in Fig. 4.1.7. In these examples Fig. 4.1.7a and Fig. 4.1.7b relate to a device where markers calculated from Ph. I, Ph. II data are alike. The plots show that in case of a device producing sporadic noisy points, Ph. I of the algorithm is enough to remove these points (Fig. 4.1.7a) and calculate the correct markers, while Ph. II is useful just to forecast the lifetime. On the other hand, Fig. 4.1.7c and Fig. 4.1.7d are processed starting from a device with lifetime data filled with dumps and rifts. Comparing the two plots allows us to underline the extent to which the complete algorithm allows a better lifetime marker estimation compared to simply filtering noisy data. In this example, the [E_{S_Filter}; T_{S80_Filter}] energy window (underlined in Fig. 4.1.7c) calculated for filtered curve (Ph. I) is erroneous, since the bumps in the curve affect the lifetime determination. Meanwhile, the fitted curve (Ph. II) leads to overlap of [E_{S_Fit}; T_{S80_Fit}] and [E_0; T_{80}] window, pointing to the fact that for this specific device the maximum lifetime in reality is reached at the initial stage and therefore T_{80} and T_{S80} are the same.

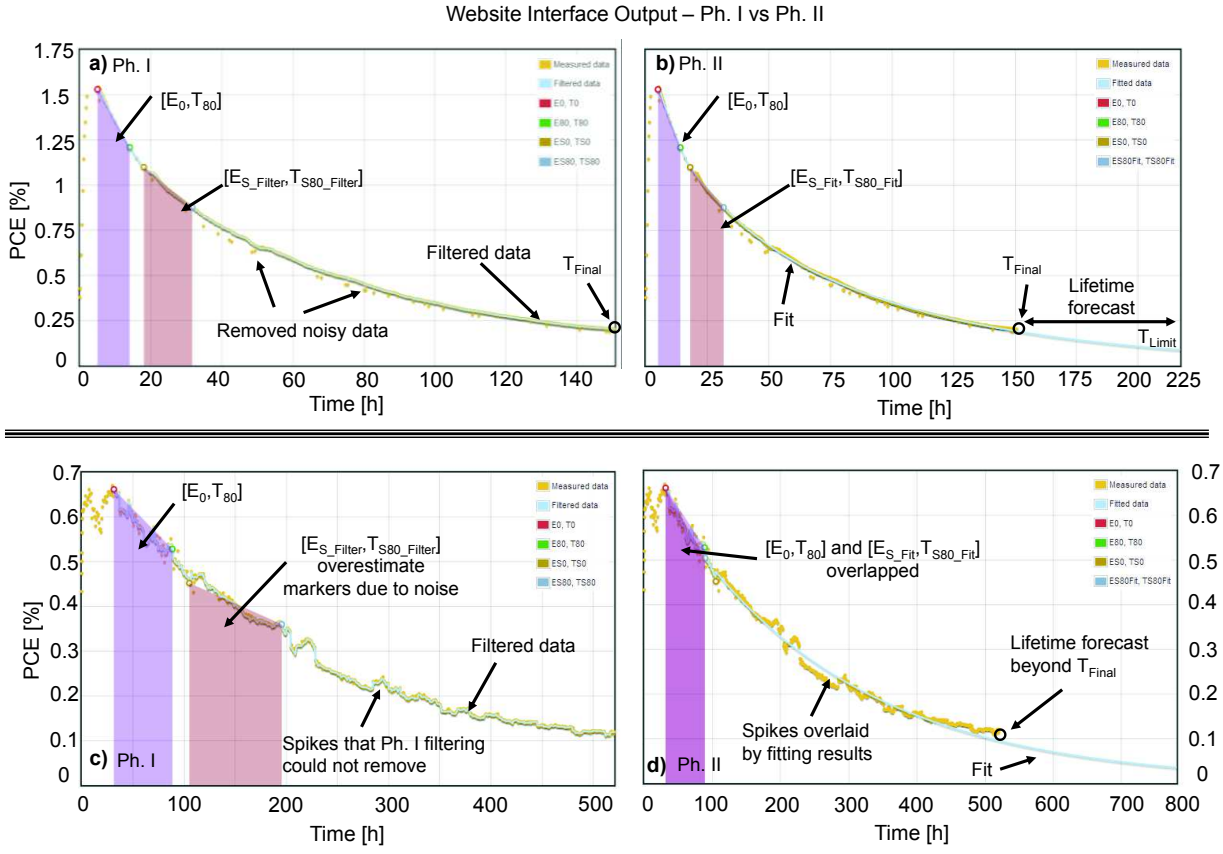

Fig. 4.1.7 Examples of processed data by using the web platform tool. a) and c) are data processed only by Ph. I while b) and d) are data processed by the whole algorithm (Ph. I and Ph. II), forecasting the lifetime beyond T_{Final}. Within each subfigure, we underlined some examples of peculiar behaviors of PCE over time and how the algorithm solves most of these problems.

Device	$[E_0; T_{80}]$ [(%); (h)]	$[E_{S\_Filter}; T_{S80\_Filter}]$ [(%); (h)]	$[E_{S\_Fit}; T_{S80\_Fit}]$ [(%); (h)]
a) & b)	[1.53; 9.1]	[1.1; 13.6]	[1.1; 13.6]
c) & d)	[0.66; 57.2]	[0.45; 90.4]	[0.66; 57.9]

Tab. 4.1-C Lifetime marker estimated by the Extrapolation procedure from data processed during Ph. I and/or Ph. II showed in Fig. 4.1.7.

In the Tab. 4.1-C we observe that for some devices, as the cases a), the fitting procedure applied during Ph. II is redundant since the algorithm does not obtain substantial differences from estimation performed after Ph. I or Ph. II. On the other hand, in some cases, as the example device used in Fig. 4.1.7c, Fig. 4.1.7d, the fit is a key resource to prevent misleading estimation and avoid erroneous markers calculation.

While it may appear that lifetime estimation from fitted curve will always be more accurate compared to filtered curve, it is still important to check the data from fitting against the filtered data. Indeed, due to very dynamic nature of the curves the fitting may in some circumstances not represent the real data accurate enough, especially in the predicted section of the curve. Thus, although the algorithm is significantly aiding the process of reproducibly estimating the lifetime values and greatly decreasing the time of data treatment, the user of the tool still needs to carefully monitor the shapes of filtered and fitted curve after each processing and assess the accuracy of lifetime determination with one or the other method.

4.1.3.2 Algorithm Future Optimizations

The following paragraph summarizes some drawbacks and possible future improvements of the algorithm.

First, in the current version the tuning of the parameters (number of samples and *k*) used during the application of the *Hampel* filtering procedure (see *Phase I* in the *Algorithm Structure* paragraph) was done by an iterative empirical approach, by increasing or decreasing *k* and the number of samples, based on the results observed during data processing. The parameters are mostly defined by the frequency of the measurement and therefore, for data with different periodicity of measurements the parameters need to be adjusted accordingly. Indeed, the higher the sampling frequency, the higher number of samples can be used to calculate the moving average. A proposed improvement to the algorithm would be to develop automatic procedure where the algorithm identifies the frequency of the measurements and selects the parameter values accordingly. The *k* parameter however, depends on both the number of samples chosen and the curve dynamic. When the decay is highly exponential, using an exceedingly small *k* value in combination with a high number of samples will clamp the initial dynamic behavior. Therefore, the algorithm additionally should estimate the tangential of the ageing curves at different sections and adjust the *k* value depending on the range of the value of tangential.

Second, in the current version of the algorithm one of the filtering steps constitutes application of double exponential fitting to the product V_{OC}*I_{SC} and although, double exponential can to some extend be fitted to linear functions, it still imposes constrains. Therefore, the future versions of the algorithm should include a possibility of choosing between exponential and linear functions.

Finally, the functions currently adopted to forecast the device lifetime are only the linear, single and double exponential. In the future, a wider range of choices may allow the users to personalize the fitting functions applied during Ph. II. Furthermore, a tool providing users' custom defined functions could be useful in order to give the users higher flexibility and interaction with the algorithm processing steps.

It is our hope that after carrying several optimization steps in the algorithm and testing and validating it for many different data scenarios, we will build a publically available tool for automatic lifetime calculation, where any user can upload data and extract lifetime parameters. Meanwhile, this manuscript will serve as a guideline for anyone willing to go through the process of programming the presented algorithm. For manual determination of the lifetime from any ageing curve, we once more refer the reader to Tab. 4.1-A.

4.1.4 Summary

An algorithm was presented that allows automatic estimation of the lifetime markers from different ageing curves of photovoltaic devices with rather dynamic behavior, such as organic or hybrid PVs. The algorithm consists of two parts, the data filtering, which reduces the noise and the fitting part, which applies a fitted curve to the ageing curve to accurately determine the lifetime or predict it by extrapolation of the ageing curve within a limited time range. The article discussed in detail the algorithm as well as the online tool that allows uploading measured data and monitoring the data processed by the algorithm. A range of examples of data treatment on real measured samples was presented and the difference between filtered and fitted data was discussed. It was demonstrated that the combination of the two methods was the optimal for the most accurate and reproducible lifetime assessment. Finally, a few possible improvements of the algorithm were discussed, that would allow optimizing the data processing. It was highlighted that the important advantage of the algorithm is the significant reduction of data processing time compared to manual determination of lifetime from multitude of ageing curves with different shapes.

The drawback of such a method is that although it automatically detects and fits the shape of the ageing curves, it may still in certain circumstances not be able to fit correctly some of the very dynamic degradation features and therefore, to a certain degree human control of the final fitted curves is necessary.

5 Conclusions

Photovoltaics is undergoing continuous evolution since its first demonstration and different technologies developed in the years of industrial and academic research. Among the several technologies, organic and hybrid photovoltaics represent a low cost and short payback time alternative to more efficient but expensive inorganic solar cells. However, several issues are still to be address in order to make organic and hybrid PV technologies advantageous compared to widespread inorganic competitors. In particular, reliability and stability must be investigated and tested, verifying which are the reasons behind UV, temperature, moisture and electric field induced degradation. Revealing the physics behind these degradation mechanisms allows adopting proper countermeasures that will permit extending organic and hybrid solar cells lifetime and making these sustainable technologies competitive with the market ready inorganic PVs. To this purpose, we characterize, model and stress both organic and hybrid solar cells.

We analyzed heterojunction P3HT:PCBM solar cell by means of I-V and IS measurements at various bias voltage and illumination intensity. This large collection of data allows obtaining a more comprehensive picture of IS peaks and permits us to elaborate a model for describing the cell characteristics. ZnO generates a peak at high frequency in IS curves of fresh cells. This peak moves towards lower frequency values and increases in size when ZnO is degraded by exposing the electrode to UV during the fabrication process. The main peak, which widely varies with increasing reverse bias voltage and illumination, is ascribed to the space charge region impedance. This agrees with the evolution of the extracted parameters as a function of bias and illumination. Noticeably, due to a higher impedance value of ZnO interface, the polarization conditions of SCR in fresh cells and UV degraded ones are definitely dissimilar and we cannot directly compare extracted physical coefficients without taking into account these differences.

Furthermore, we performed electrical stress at forward current and thermal storage on P3HT:PCBM solar cells. During electrical stress, we applied several levels of current both in dark and under illumination, while we tested three different temperatures for thermal storage. Applying a modified version of the Sokel-Hughes/Braun-Onsager model, we extracted the diffusion photocurrent contribution at the zero-field voltage and we analyzed the variations of these two parameters with stress time. Stresses generate both degradation and recovery on solar cells. During constant current stress we observe an increase of the zero-field voltage for all devices that we related to the p-doping induced by oxidation process within P3HT. Differently, thermal storage may induce a recovery of the diffusion current density depending on the time of storage and if the temperature of stress is above or below the glass transition point. A possible explanation for observed variations is that a phase change occurs within the cells that induce a rearrangement of the active layer morphology. We proved that IS performed during stresses allow a better comprehension of interface degradation. Indeed, with IS we clearly observe that current stress and thermal storage generate different damages on the active layer and the ZnO interface. We deepened the investigation of the degradation mechanisms during the constant current stress in forward bias condition and we showed that the polaron recombination rate is one of the major reasons for the cell degradation. Besides, our data and the model show that a correlation exists between the band bending at the interfaces and the photocurrent, and these bending contribute to cell performances together with the polaron recombination rate. Even though the applied model is very simple and qualitative, it is still suitable for finding a relation between the cell degradation and the variation of some parameters, such as the exciton separation probability or the contact barrier heights. Of course, some limits still exist. For instance, it is possible to extract the cumulative effects of the barrier height at the contacts, but it is not possible to distinguish and separate the contribution of the single barrier. Afterward, we improved this qualitative model by developing our detailed and complete analytical representation of the photocurrent dynamics.

Perovskite based solar cells promise high efficiency at low cost; however, this technology is not stable and reliable and thus advancement in materials and processing is mandatory. The laser ablation synthesis in organic solvent of PbI_2 nanocrystals made possible to obtain different types of perovskite materials more resistant to ionic motion. A hybrid graphite-lead iodide precursor was obtained with a strong interaction among materials, since the graphite was obtained with the decomposition of the solvent on the surfaces of the nanocrystals. Among the characterization techniques, the EPR one allowed to evidence the presence of a charge exchange between the nanocrystals and graphene-like patches at the grain boundaries making less available the defect states of perovskite material to the ionic motion. The electrical characterizations confirm that thin film graphite lead-iodide based perovskite has a less hysteretic behavior than the reference spin-coated thin film perovskite. These results shed light on the key role of defect sites on the mechanism of ionic motion, providing a path for the synthesis of stable materials.

In order to disclose the mechanisms behind perovskite instability, we studied methyl-ammonium lead-iodide perovskite material. MAPI is synthetized starting from spray-coated PbI_2 precursor obtained by laser ablation technique explained above and is more robust against ions migration and electric field induced degradation, although being very similar to the standard spin-coated MAPI. The aim of our investigation was recognizing all the possible phenomena at the base of the electrical hysteresis characterizing perovskite devices. In particular, we aimed to distinguish between temporary and permanent phenomena generated during the current-voltage scans. We used electrical characterization at different scan rates and optical measurements to reach our goal. The results of our measurements are straightforward: no or negligible ferroelectric phenomenon exists in the PVK and ions migration in the PVK has several effects, both positive and negative. The ions move following the drift-diffusion law and the migration occurs mainly in the MAPI grain boundaries. Under the effect of applied bias, ions accumulate at the interfaces with the electrodes, generating dipoles. The dipoles change the band alignment of the semiconductor with the electrodes work function and thus they change the current injection dynamics, in particular changing the current injected by tunneling effect. However, due to the high electric field at the interfaces generated by the accumulated ions, a degradation mechanism occurs that converts back to the initial precursors (MAI and PbI_2) the PVK layer. Therefore, insulating degraded layers generate around the electrodes, limiting the current injected in dark and extracted in light. The presence of these layers was detected both in the current-voltage scans and in the optical measurements. In order to explain the dynamics observed in the devices during the current-voltage scans, we presented a qualitative model describing the bands bending under different conditions. Our model takes account for all the phenomena observed in the electrical and optical characterizations. Although we made all these observations and models to explain the characterizations of a planar structure, the same phenomena occur in case of vertical structures, which are used in perovskite solar cells. However, these phenomena are less evident in vertical structures, due to the different thickness of the active layer and the different number of grains and boundaries involved in the charge/ion transport. Remarkably, the damage induced by the dipoles is a relevant problem on vertical as well as on planar structures. Despite the positive improved band alignment that dipoles might induce, the high electric field generated is destructive. Thus, we provided a wiser view of the ions migration effects, giving a further demonstration that ionic motion must be suppressed in order to optimize functionality and reliability of PVK materials, extending perovskite solar cells lifetime.

On full perovskite solar cells using Spiro-OMeTAD as hole transport material, we performed storage and thermal stresses. The cells are encapsulated using two different sealing techniques. Both stresses and simple storage induced degradation on the samples, lowering efficiency, short-circuit current, open-circuit voltage and fill factor. Storing

devices in dark leads only to small performances loss mainly due to the measurement process itself, while thermal stress generated increasing damage to the devices. Edge sealing results to be a better approach to reduce moisture percolation and oxidation mechanisms at least at stress temperatures below 80°C, resulting into an increased lifetime. On the other hand, at high stress temperatures the additional sealing becomes counterproductive and accelerates the performances decay. However, further investigation is necessary in order to fully understand the kinetics and dynamics occurring within perovskite solar cells exposed to thermal stresses. In conclusion, by coupling thermal stress and electrical measurements, we detected and distinguished at least two possible sources of degradation that can give insights into the understanding of losses mechanisms of perovskite solar cells.

Since organic or hybrid PV ageing curves have a rather dynamic behavior, we developed an algorithm that allows automatic estimation of the lifetime markers from different ageing curves. The algorithm consists of two parts, the data filtering, which reduces the noise and the fitting part, which applies a fitted curve to the ageing curve to accurately determine the lifetime or predict it by extrapolation of the ageing curve within a limited time range. We discuss in detail the algorithm as well as the online tool that allows uploading measured data and monitoring the data processed by the algorithm. We present a range of examples of data treatment on real measured samples and we discuss the difference between filtered and fitted data. We demonstrate that the combination of the two methods was the optimal for the most accurate and reproducible lifetime assessment. Finally, we discuss a few possible improvements of the algorithm, which would allow optimizing the data processing. We highlight that the important advantage of the algorithm is the significant reduction of data processing time compared to manual determination of lifetime from multitude of ageing curves with different shapes. The drawback of such a method is that although it automatically detects and fits the shape of the ageing curves, it may still in certain circumstances not be able to fit correctly some of the very dynamic degradation features and therefore, to a certain degree human control of the final fitted curves is necessary.

6 Publications

6.1 List of publications on international journals

J1. Wrachien, N., Lago, N., Rizzo, A., D'Alpaos, R., Stefani, A., Turatti, G., Muccini, M., Meneghesso, G., Cester, A., *Effects of thermal and electrical stress on DH4T-based organic thin-film-transistors with PMMA gate dielectrics*, (2015) **Microelectronics Reliability**, 55 (9-10), pp. 1790-1794. DOI: 10.1016/j.microrel.2015.06.073

J2. Cester, A., Rizzo, A., Bazzega, A., Lago, N., Favaro, J., Barbato, M., Wrachien, N., Gevorgyan, S.A., Corazza, M., Krebs, F.C., *Effects of constant voltage and constant current stress in PCBM:P3HT solar cells*, (2015) **Microelectronics Reliability**, 55 (9-10), pp. 1795-1799. DOI: 10.1016/j.microrel.2015.06.082

J3. Wrachien, N., Cester, A., Lago, N., Rizzo, A., D'Alpaos, R., Stefani, A., Turatti, G., Muccini, M., Meneghesso, G., *Reliability study of organic complementary logic inverters using constant voltage stress* ,(2015) **Solid-State Electronics**, 113, art. no. 6817, pp. 151-156. DOI: 10.1016/j.sse.2015.05.028

J4. Lago, N., Cester, A., Wrachien, N., Natali, M., Quiroga, S.D., Bonetti, S., Barbato, M., Rizzo, A., Benvenuti, E., Benfenati, V., Muccini, M., Toffanin, S., Meneghesso, G., *A physical-based equivalent circuit model for an organic/electrolyte interface*, (2016) **Organic Electronics**, 35, pp. 176-185. DOI: 10.1016/j.orgel.2016.05.018

J5. Rizzo, A., Cester, A., Torto, L., Barbato, M., Wrachien, N., Lago, N., Corazza, M., Krebs, F.C., Gevorgyan, S.A., *Effects of current stress and thermal storage on polymeric heterojunction P3HT:PCBM solar cell*, (2016) **IEEE International Reliability Physics Symposium Proceedings**, 2016-September, art. no. 7574523, pp. 3C21-3C26. DOI: 10.1109/IRPS.2016.7574523

J6. Wrachien, N., Barbato, M., Cester, A., Rizzo, A., Meneghesso, G., D'Alpaos, R., Turatti, G., Generali, G., Muccini, M., *Analysis of ESD effects on organic thin-film-transistors by means of TLP technique,* (2016) **IEEE International Reliability Physics Symposium Proceedings**, 2016-September, art. no. 7574607, pp. EL61-EL65. DOI: 10.1109/IRPS.2016.7574607

J7. Torto, L., Cester, A., Rizzo, A., Wrachien, N., Gevorgyan, S.A., Corazza, M., Krebs, F.C., *Model of Organic Solar Cell Photocurrent Including the Effect of Charge Accumulation at Interfaces and Non-Uniform Carrier Generation*, (2016) **IEEE Journal of the Electron Devices Society**, 4 (6), art. no. 7549082, pp. 387-395. DOI: 10.1109/JEDS.2016.2602563

J8. Rizzo, A., Torto, L., Wrachien, N., Corazza, M., Krebs, F.C., Gevorgyan, S.A., Cester, A., *Application of photocurrent model on polymer solar cells under forward bias stress*, (2016) **IEEE Journal of Photovoltaics**, 6 (6), pp. 1542-1548. DOI: 10.1109/JPHOTOV.2016.2603841

J9. Rizzo, A., Cester, A., Wrachien, N., Lago, N., Torto, L., Barbato, M., Favaro, J., Gevorgyan, S.A., Corazza, M., Krebs, F.C., *Characterization and modeling of organic (P3HT:PCBM) solar cells as a function of bias and illumination*, (2016) **Solar Energy Materials and Solar Cells**, 157, pp. 337-345. DOI: 10.1016/j.solmat.2016.06.001

J10. Torto, L., Cester, A., Passarini, L., Rizzo, A., Wrachien, N., Seri, M., Muccini, M., *Open circuit voltage decay as a tool to assess the reliability of organic solar cells: P3HT:PCBM vs. HBG1:PCBM*, (2017) **IEEE International Reliability Physics Symposium Proceedings**, art. no. 7936272, pp. 2F2.1-2F2.10. DOI:

10.1109/IRPS.2017.7936272

J11. Torto, L., Rizzo, A., Cester, A., Wrachien, N., Passarini, L., Krebs, F.C., Corazza, M., Gevorgyan, S.A., *Analysis of electrical and thermal stress effects on PCBM:P3HT solar cells by photocurrent and impedance spectroscopy modeling*, (2017) **IEEE International Reliability Physics Symposium Proceedings**, art. no. 7936274, pp. 2F4.1-2F4.10. DOI: 10.1109/IRPS.2017.7936274

J12. Rizzo, A., Ortolan, L., Murrone, S., Torto, L., Barbato, M., Wrachien, N., Cester, A., Matteocci, F., Di Carlo, A., *Effects of thermal stress on hybrid perovskite solar cells with different encapsulation techniques*, (2017) **IEEE International Reliability Physics Symposium Proceedings**, art. no. 7936396, pp. PV1.1-PV1.6. DOI: 10.1109/IRPS.2017.7936396

J13. Rizzo, A., Cester, A., Madsen, M.V., Krebs, F.C., Gevorgyan, S.A., *A Novel Algorithm for Lifetime Extrapolation, Prediction, and Estimation of Emerging PV Technologies*, (2017) **Small Methods**, 2 (1), art. no. 1700285. DOI: 10.1002/smtd.201700285

J14. Buonomo, M., Torto, L., Barbato, M., Wrachien, N., Rizzo, A., Gevorgyan, S.A., Krebs, F.C., Cester, A., *Analysis of the effects of voltage pulses on P3HT:PCBM polymeric solar cells by means of TLP technique*, (2018) **Microelectronics Reliability**. DOI: 10.1016/j.microrel.2018.06.059

J15. Torto, L., Cester, A., Wrachien, N., Rizzo, A., Gedefaw, D., Andersson, M.R., Seri, M., Muccini, M., *Application of an Open-Circuit Voltage Decay Model to Compare the Performances of Donor Polymers in Bulk Heterojunction Solar Cells*, (2018) **IEEE Journal of Photovoltaics**, 8 (2), pp. 517-524. DOI: 10.1109/JPHOTOV.2018.2792461

J16. Rizzo, A., Lamberti, F., Buonomo, M., Wrachien, N., Torto, L., Lago, N., Sansoni, S., Pilot, R., Prato, M., Michieli, N., Meneghetti, M., Meneghesso, G., Cester, A., *Understanding lead iodide perovskite hysteresis and degradation causes by extensive electrical characterization*, (2019) **Solar Energy Materials and Solar Cells**, 189, pp. 43-52. DOI:10.1016/j.solmat.2018.09.021.

6.2 List of publications on conference proceedings

C1. Wrachien, N., Lago, N., Rizzo, A., D'Alpaos, R., Stefani, A., Turatti, G., Muccini, M., Meneghesso, G., Cester, A., *Effects of thermal and electrical stress on DH4T-based organic thin-film-transistors with PMMA gate dielectrics*, (2015) **26th European Symposium on Reliability of Electron Devices**, 55 (9-10), pp. 1790-1794. DOI: 10.1016/j.microrel.2015.06.073

C2. Cester, A., Rizzo, A., Bazzega, A., Lago, N., Favaro, J., Barbato, M., Wrachien, N., Gevorgyan, S.A., Corazza, M., Krebs, F.C., *Effects of constant voltage and constant current stress in PCBM:P3HT solar cells*, (2015) **26th European Symposium on Reliability of Electron Devices**, 55 (9-10), pp. 1795-1799. DOI: 10.1016/j.microrel.2015.06.082

C3. Rizzo, A., Cester, A., Torto, L., Barbato, M., Wrachien, N., Lago, N., Corazza, M., Krebs, F.C., Gevorgyan, S.A., *Effects of current stress and thermal storage on polymeric heterojunction P3HT:PCBM solar cell*, (2016) **IEEE International Reliability Physics Symposium**, 2016-September, art. no. 7574523, pp. 3C21-3C26. DOI: 10.1109/IRPS.2016.7574523

C4. Wrachien, N., Barbato, M., Cester, A., Rizzo, A., Meneghesso, G., D'Alpaos, R., Turatti, G., Generali, G., Muccini, M., *Analysis of ESD effects on organic thin-film-transistors by means of TLP technique,* (2016) **IEEE International Reliability Physics Symposium**, 2016-September, art. no. 7574607, pp. EL61-EL65. DOI: 10.1109/IRPS.2016.7574607

C5. Torto, L., Cester, A., Passarini, L., Rizzo, A., Wrachien, N., Seri, M., Muccini, M., *Open circuit voltage decay as a tool to assess the reliability of organic solar cells: P3HT:PCBM vs. HBG1:PCBM*, (2017) **IEEE International Reliability Physics Symposium**, art. no. 7936272, pp. 2F2.1-2F2.10. DOI: 10.1109/IRPS.2017.7936272

C6. Torto, L., Rizzo, A., Cester, A., Wrachien, N., Passarini, L., Krebs, F.C., Corazza, M., Gevorgyan, S.A., *Analysis of electrical and thermal stress effects on PCBM:P3HT solar cells by photocurrent and impedance spectroscopy modeling*, (2017) **IEEE International Reliability Physics Symposium**, art. no. 7936274, pp. 2F4.1-2F4.10. DOI: 10.1109/IRPS.2017.7936274

C7. Rizzo, A., Ortolan, L., Murrone, S., Torto, L., Barbato, M., Wrachien, N., Cester, A., Matteocci, F., Di Carlo, A., *Effects of thermal stress on hybrid perovskite solar cells with different encapsulation techniques*, (2017) **IEEE International Reliability Physics Symposium**, art. no. 7936396, pp. PV1.1-PV1.6. DOI: 10.1109/IRPS.2017.7936396

C8. Buonomo, M., Torto, L., Barbato, M., Wrachien, N., Rizzo, A., Gevorgyan, S.A., Krebs, F.C., Cester, A., *Analysis of the effects of voltage pulses on P3HT:PCBM polymeric solar cells by means of TLP technique*, (2018) **29th European Symposium on Reliability of Electron Devices**. DOI: 10.1016/j.microrel.2018.06.059

6.3 List of submitted works

S1. Lamberti, F., Rizzo, A., Cescon, E., Sorrentino, R., Litti, L., Reguera, J., Salerno, M., Michieli, N., Buonomo, M., Toffoletti, A., Cester, A., Meneghesso, G., Franco, L., Petrozza, A., Meneghetti, M., *Suppression of ionic motions in a perovskite thin film for optoelectronic applications*, (2018)

7 Index of graphical elements

7.1 Index of figures

7.2 Index of Tables

7.3 Index of schemes

8 Bibliography

[1] A. des sciences (France). A. du texte, Comptes rendus hebdomadaires des séances de l'Académie des sciences / publiés... par MM. les secrétaires perpétuels, (1839). http://gallica.bnf.fr/ark:/12148/bpt6k2968p/f561.chemindefer (accessed June 4, 2018).

[2] D.M. Bagnall, M. Boreland, Photovoltaic technologies, Energy Policy. 36 (2008) 4390–4396. doi:10.1016/J.ENPOL.2008.09.070.

[3] W. Shockley, H.J. Queisser, Detailed Balance Limit of Efficiency of *p-n* Junction Solar Cells, J. Appl. Phys. 32 (1961) 510–519. doi:10.1063/1.1736034.

[4] M.A. Green, Y. Hishikawa, E.D. Dunlop, D.H. Levi, J. Hohl-Ebinger, A.W.Y. Ho-Baillie, Solar cell efficiency tables (version 52), Prog. Photovoltaics Res. Appl. 26 (2018) 427–436. doi:10.1002/pip.3040.

[5] L.K. NREL, Best Research-Cell Efficiencies, 57] MA Green," Corrigendum to Sol. Cell Effic. Tables (Version 46)[Prog. Photovolt Res. Appl. 23 (2015) 1202. http://www.nrel.gov/pv/assets/images/efficiency-chart.png (accessed January 1, 2018).

[6] A. Pochettino, No Title, Acad. Lincei Rendus. 15 (1906) 355.

[7] B. O'Regan, M. Grätzel, A low-cost, high-efficiency solar cell based on dye-sensitized colloidal TiO2 films, Nature. 353 (1991) 737–740. doi:10.1038/353737a0.

[8] F.C. Krebs, Roll-to-roll fabrication of monolithic large-area polymer solar cells free from indium-tin-oxide, Sol. Energy Mater. Sol. Cells. 93 (2009) 1636–1641. doi:10.1016/j.solmat.2009.04.020.

[9] J.H. Noh, S.H. Im, J.H. Heo, T.N. Mandal, S. Il Seok, Chemical Management for Colorful, Efficient, and Stable Inorganic–Organic Hybrid Nanostructured Solar Cells, Nano Lett. 13 (2013) 1764–1769. doi:10.1021/nl400349b.

[10] N. Wrachien, A. Cester, D. Bari, J. Kovac, J. Jakabovic, D. Donoval, et al., Near-UV Irradiation Effects on Pentacene-Based Organic Thin Film Transistors, IEEE Trans. Nucl. Sci. 58 (2011) 2911–2917. doi:10.1109/TNS.2011.2170432.

[11] D. Bari, N. Wrachien, R. Tagliaferro, T.M. Brown, A. Reale, A. Di Carlo, et al., Reliability study of dye-sensitized solar cells by means of solar simulator and white LED, Microelectron. Reliab. 52 (2012) 2495–2499. doi:10.1016/j.microrel.2012.06.061.

[12] N. Robertson, Organic Photovoltaics. Mechanisms, Materials and Devices. Edited by Sam-Shajing Sun and Niyazi Serdar Sariciftci., Angew. Chemie Int. Ed. 45 (2006) 7321–7321. doi:10.1002/anie.200585423.

[13] G. Calogero, P. Calandra, A. Irrera, A. Sinopoli, I. Citro, G. Di Marco., A new type of transparent and low cost counter-electrode based on platinum nanoparticles for dye-sensitized solar cells, Energy Environ. Sci. 4 (2011) 1838. doi:10.1039/c0ee00463d.

[14] C.J. Brabec, S. Gowrisanker, J.J.M. Halls, D. Laird, S. Jia, S.P. Williams, Polymer-Fullerene Bulk-Heterojunction Solar Cells, Adv. Mater. 22 (2010) 3839–3856. doi:10.1002/adma.200903697.

[15] E. Greul, M.L. Petrus, A. Binek, P. Docampo, T. Bein, Highly stable, phase pure $Cs_2AgBiBr_6$ double perovskite thin films for optoelectronic applications, J. Mater. Chem. A. 5 (2017) 19972–19981. doi:10.1039/C7TA06816F.

[16] F. Hao, C.C. Stoumpos, D.H. Cao, R.P.H. Chang, M.G. Kanatzidis, Lead-free solid-state organic–inorganic halide perovskite solar cells, Nat. Photonics. 8 (2014) 489–494. doi:10.1038/nphoton.2014.82.

[17] NREL PV Efficiency chart, (n.d.). https://www.nrel.gov/pv/assets/images/efficiency-chart-20180716.jpg (accessed July 23, 2018).

[18] D. Bari, N. Wrachien, R. Tagliaferro, T.M. Brown, A. Reale, A. Di Carlo, et al., Comparison between positive and negative constant current stress on dye-sensitized solar cells, Microelectron. Reliab. 53 (2013) 1804–1808. doi:10.1016/j.microrel.2013.07.093.

[19] A. Rizzo, A. Cester, L. Torto, M. Barbato, N. Wrachien, N. Lago, et al., Effects of current stress and thermal storage on polymeric heterojunction P3HT:PCBM solar cell, in: IEEE Int. Reliab. Phys. Symp. Proc., Institute of Electrical and Electronics Engineers Inc., Pasadena - CA, 2016: p. 3C21-3C26. doi:10.1109/IRPS.2016.7574523.

[20] A. Rizzo, L. Ortolan, S. Murrone, L. Torto, M. Barbato, N. Wrachien, et al., Effects of thermal stress on hybrid perovskite solar cells with different encapsulation techniques, in: 2017 IEEE Int. Reliab. Phys. Symp., IEEE, 2017: p. PV-1.1-PV-1.6. doi:10.1109/IRPS.2017.7936396.

[21] A. Rizzo, L. Torto, N. Wrachien, M. Corazza, F.C. Krebs, S.A. Gevorgyan, et al., Application of Photocurrent Model on Polymer Solar Cells Under Forward Bias Stress, IEEE J. Photovoltaics. 6 (2016) 1542–1548. doi:10.1109/JPHOTOV.2016.2603841.

[22] D. Bari, N. Wrachien, R. Tagliaferro, S. Penna, T.M. Brown, A. Reale, et al., Thermal stress effects on Dye-Sensitized Solar Cells (DSSCs), Microelectron. Reliab. 51 (2011) 1762–1766. doi:10.1016/j.microrel.2011.07.061.

[23] A. Cester, A. Rizzo, A. Bazzega, N. Lago, J. Favaro, M. Barbato, et al., Effects of constant voltage and constant current stress in PCBM:P3HT solar cells, Microelectron. Reliab. 55 (2015) 1795–1799. doi:10.1016/j.microrel.2015.06.082.

[24] Toshiba Corporate Research & Development Center : NEDO and Toshiba Develops World's Largest Film-based Perovskite Photovoltaic Module -703cm^2 module achieves 11.7% power conversion efficiency-, (n.d.). https://www.toshiba.co.jp/rdc/rd/detail_e/e1806_03.html (accessed July 24, 2018).

[25] J.A. Christians, J.S. Manser, P. V. Kamat, Best Practices in Perovskite Solar Cell Efficiency Measurements. Avoiding the Error of *Making Bad Cells Look Good*, J. Phys. Chem. Lett. 6 (2015) 852–857. doi:10.1021/acs.jpclett.5b00289.

[26] R. Rösch, D.M. Tanenbaum, M. Jørgensen, M. Seeland, M. Bärenklau, M. Hermenau, et al., Investigation of the degradation mechanisms of a variety of organic photovoltaic devices by combination of imaging techniques—the ISOS-3 inter-laboratory collaboration, Energy Environ. Sci. 5 (2012) 6521. doi:10.1039/c2ee03508a.

[27] S. Schiefer, B. Zimmermann, S.W. Glunz, U. Würfel, Applicability of the suns-VOC method on organic solar cells, IEEE J. Photovoltaics. 4 (2014) 271–277. doi:10.1109/JPHOTOV.2013.2288527.

[28] H. Shen, L. Cai, Z. Liu, W. Wu, J. Bao, Influence of the Bottom WO3 Layer on the Series Resistance in Silicon Based Solar Cells with WO3/Ag/WO3 Emitter, 32nd Eur. Photovolt. Sol. Energy Conf. Exhib. (2016) 775–779. doi:10.4229/EUPVSEC20162016-2AV.3.3.

[29] M.O. Reese, S. a. Gevorgyan, M. Jørgensen, E. Bundgaard, S.R. Kurtz, D.S. Ginley, et al., Consensus stability testing protocols for organic photovoltaic materials and devices, Sol. Energy Mater. Sol. Cells. 95 (2011) 1253–1267. doi:10.1016/j.solmat.2011.01.036.

[30] A. Facchetti, Polymer donor–polymer acceptor (all-polymer) solar cells, Mater. Today. 16 (2013) 123–132. doi:10.1016/J.MATTOD.2013.04.005.

[31] F.C. Krebs, M. Hoesel, M. Corazza, B. Roth, M. V. Madsen, S. a. Gevorgyan, et al., Freely Available OPV-The Fast Way to Progress, Energy Technol. 1 (2013) 378–381. doi:10.1002/ente.201300057.

[32] H.F. Dam, T.R. Andersen, M. V. Madsen, T.K. Mortensen, M.F. Pedersen, U. Nielsen, et al., Roll and roll-to-roll process scaling through development of a compact flexo unit for printing of back electrodes, Sol. Energy Mater. Sol. Cells. 140 (2015) 187–192. doi:10.1016/j.solmat.2015.04.007.

[33] H. Hoppe, N.S. Sariciftci, Organic solar cells: An overview, J. Mater. Res. 19 (2004) 1924–1945. doi:10.1557/JMR.2004.0252.

[34] H.F. Dam, F.C. Krebs, Simple roll coater with variable coating and temperature control for printed polymer solar cells, Sol. Energy Mater. Sol. Cells. 97 (2012) 191–196. doi:10.1016/j.solmat.2011.08.027.

[35] D. Angmo, S. a. Gevorgyan, T.T. Larsen-Olsen, R.R. Søndergaard, M. Hösel, M. Jørgensen, et al., Scalability and stability of very thin, roll-to-roll processed, large area, indium-tin-oxide free polymer solar cell modules, Org. Electron. Physics, Mater. Appl. 14 (2013) 984–994. doi:10.1016/j.orgel.2012.12.033.

[36] F.C. Krebs, Air stable polymer photovoltaics based on a process free from vacuum steps and fullerenes, Sol. Energy Mater. Sol. Cells. 92 (2008) 715–726. doi:10.1016/j.solmat.2008.01.013.

[37] E. Dunlop, T. Sample, G. Bardizza, A. Pozza, Analysis Based on I-V Curve Changes of Organic Photovoltaic Mini-Modules Subjected to Degradation under Different Temperature and Humidity Conditions, 29th Eur. Photovolt. Sol. Energy Conf. Exhib. (2014) 1523–1529. doi:10.4229/EUPVSEC20142014-3CO.8.1.

[38] M.R. Lilliedal, A.J. Medford, M. V. Madsen, K. Norrman, F.C. Krebs, The effect of post-processing treatments on inflection points in current–voltage curves of roll-to-roll processed polymer photovoltaics, Sol. Energy Mater. Sol. Cells. 94 (2010) 2018–2031. doi:10.1016/j.solmat.2010.06.007.

[39] Z.E. Ooi, T.L. Tam, A. Sellinger, J.C. deMello, Field-dependent carrier generation in bulk heterojunction solar cells, Energy Environ. Sci. 1 (2008) 300. doi:10.1039/b805435e.

[40] Z.E. Ooi, R. Jin, J. Huang, Y.F. Loo, A. Sellinger, J.C. deMello, On the pseudo-symmetric current–voltage response of bulk heterojunction solar cells, J. Mater. Chem. 18 (2008) 1644. doi:10.1039/b718563d.

[41] M. Limpinsel, A. Wagenpfahl, M. Mingebach, C. Deibel, V. Dyakonov, Photocurrent in bulk heterojunction solar cells, Phys. Rev. B. 81 (2010) 085203. doi:10.1103/PhysRevB.81.085203.

[42] M. Glatthaar, N. Mingirulli, B. Zimmermann, T. Ziegler, R. Kern, M. Niggemann, et al., Impedance spectroscopy on organic bulk-heterojunction solar cells, Phys. Status Solidi Appl. Mater. Sci. 202 (2005) 125–127. doi:10.1002/pssa.200521149.

[43] T. Kuwabara, Y. Kawahara, T. Yamaguchi, K. Takahashi, Characterization of inverted-type organic solar cells with a ZnO layer as the electron collection electrode by ac impedance spectroscopy, ACS Appl. Mater. Interfaces. 1 (2009) 2107–2110. doi:10.1021/am900446x.

[44] T. Ripolles-Sanchis, A. Guerrero, J. Bisquert, G. Garcia-Belmonte, Diffusion-Recombination Determines Collected Current and Voltage in Polymer:Fullerene Solar Cells, J. Phys. Chem. C. 116 (2012) 16925–16933. doi:10.1021/jp305941f.

[45] G. Perrier, R. de Bettignies, S. Berson, N. Lemaître, S. Guillerez, Impedance spectrometry of optimized standard and inverted P3HT-PCBM organic solar cells, Sol. Energy Mater. Sol. Cells. 101 (2012) 210–216. doi:10.1016/j.solmat.2012.01.013.

[46] R. Sokel, Numerical analysis of transient photoconductivity in insulators, J. Appl. Phys. 53 (1982) 7414. doi:10.1063/1.330111.

[47] O.E. Barcia, E. D'Elia, I. Frateur, O.R. Mattos, N. Pébère, B. Tribollet, Application of the impedance model of de Levie for the characterization of porous electrodes, Electrochim. Acta. 47 (2002) 2109–2116. doi:10.1016/S0013-4686(02)00081-6.

[48] T.T. Larsen-Olsen, R.R. Søndergaard, K. Norrman, M. Jørgensen, F.C. Krebs, All printed transparent electrodes through an electrical switching mechanism: A convincing alternative to indium-tin-oxide, silver and vacuum, Energy Environ. Sci. 5 (2012) 9467. doi:10.1039/c2ee23244h.

[49] M. Hösel, R.R. Søndergaard, M. Jørgensen, F.C. Krebs, Fast Inline Roll-to-Roll Printing for Indium-Tin-Oxide-Free Polymer Solar Cells Using Automatic Registration, Energy Technol. 1 (2013) 102–107. doi:10.1002/ente.201200029.

[50] J. Idígoras, E. Guillén, F.J. Ramos, J.A. Anta, M.K. Nazeeruddin, S. Ahmad, Highly efficient flexible cathodes for dye sensitized solar cells to complement Pt@TCO coatings, J. Mater. Chem. A. 2 (2014) 3175. doi:10.1039/c3ta13524a.

[51] Y. Kato, M.-C. Jung, M. V. Lee, Y. Qi, Electrical and optical properties of transparent flexible electrodes: Effects of UV ozone and oxygen plasma treatments, Org. Electron. 15 (2014) 721–728. doi:10.1016/j.orgel.2014.01.002.

[52] a. Wagenpfahl, D. Rauh, M. Binder, C. Deibel, V. Dyakonov, S-shaped current-voltage characteristics of organic solar devices, Phys. Rev. B. 82 (2010) 1–9. doi:10.1103/PhysRevB.82.115306.

[53] W. Tress, A. Petrich, M. Hummert, M. Hein, K. Leo, M. Riede, Imbalanced mobilities causing S-shaped IV curves in planar heterojunction organic solar cells, Appl. Phys. Lett. 98 (2011) 063301. doi:10.1063/1.3553764.

[54] W. Tress, S. Corvers, K. Leo, M. Riede, Investigation of Driving Forces for Charge Extraction in Organic Solar Cells: Transient Photocurrent Measurements on Solar Cells Showing S-Shaped Current-Voltage Characteristics, Adv. Energy Mater. 3 (2013) 873–880. doi:10.1002/aenm.201200931.

[55] C.L. Braun, Electric field assisted dissociation of charge transfer states as a mechanism of photocarrier production, J. Chem. Phys. 80 (1984) 4157–4161. doi:10.1063/1.447243.

[56] L. Onsager, Initial recombination of ions, Phys. Rev. 54 (1938) 554–557. doi:10.1103/PhysRev.54.554.

[57] R. de Levie, On the impedance of electrodes with rough interfaces, J. Electroanal. Chem. Interfacial Electrochem. 261 (1989) 1–9. doi:10.1016/0022-0728(89)87121-9.

[58] J. Bouclé, P. Ravirajan, J. Nelson, Hybrid polymer–metal oxide thin films for photovoltaic applications, J. Mater. Chem. 17 (2007) 3141. doi:10.1039/b706547g.

[59] L. Schmidt-Mende, J.L. MacManus-Driscoll, ZnO – nanostructures, defects, and devices, Mater. Today. 10 (2007) 40–48. doi:10.1016/S1369-7021(07)70078-0.

[60] M.S. White, D.C. Olson, S.E. Shaheen, N. Kopidakis, D.S. Ginley, Inverted bulk-heterojunction organic photovoltaic device using a solution-derived ZnO underlayer, Appl. Phys. Lett. 89 (2006) 143517. doi:10.1063/1.2359579.

[61] S.A. Choulis, Y. Kim, J. Nelson, D.D.C. Bradley, M. Giles, M. Shkunov, et al., High ambipolar and balanced carrier mobility in regioregular poly(3-hexylthiophene), Appl. Phys. Lett. 85 (2004) 3890. doi:10.1063/1.1805175.

[62] G. Garcia-Belmonte, A. Munar, E.M. Barea, J. Bisquert, I. Ugarte, R. Pacios, Charge carrier mobility and lifetime of organic bulk heterojunctions analyzed by impedance spectroscopy, Org. Electron. Physics, Mater. Appl. 9 (2008) 847–851. doi:10.1016/j.orgel.2008.06.007.

[63] P. Wagner, R. Helbig, Halleffekt und anisotropie der beweglichkeit der elektronen in ZnO, J. Phys. Chem. Solids. 35 (1974) 327–335. doi:10.1016/S0022-3697(74)80026-0.

[64] U. Rössler, ed., New Data and Updates for IV-IV, III-V, II-VI and I-VII Compounds, their Mixed Crystals and Diluted Magnetic Semiconductors, Springer Berlin Heidelberg, Berlin, Heidelberg, 2011. doi:10.1007/978-3-642-14148-5.

[65] D.C. Look, D.C. Reynolds, J.R. Sizelove, R.L. Jones, C.W. Litton, G. Cantwell, et al., Electrical properties of bulk ZnO, Solid State Commun. 105 (1998) 399–401. doi:10.1016/S0038-1098(97)10145-4.

[66] C. Brabec, Organic photovoltaics : materials, device physics, and manufacturing technologies, Wiley-VCH, Weinheim, 2008.

[67] D. Hertel, H. Bässler, Photoconduction in amorphous organic solids., Chemphyschem. 9 (2008) 666–88. doi:10.1002/cphc.200700575.

[68] M. Mingebach, C. Deibel, V. Dyakonov, Built-in potential and validity of the Mott-Schottky analysis in organic bulk heterojunction solar cells, Phys. Rev. B. 84 (2011) 153201. doi:10.1103/PhysRevB.84.153201.

[69] P.P. Boix, G. Garcia-Belmonte, U. Muñecas, M. Neophytou, C. Waldauf, R. Pacios, Determination of gap defect states in organic bulk heterojunction solar cells from capacitance measurements, Appl. Phys. Lett. 95 (2009) 233302. doi:10.1063/1.3270105.

[70] J. Bisquert, G. Garcia-Belmonte, A. Munar, M. Sessolo, A. Soriano, H.J. Bolink, Band unpinning and photovoltaic model for P3HT:PCBM organic bulk heterojunctions under illumination, Chem. Phys. Lett. 465 (2008) 57–62. doi:10.1016/j.cplett.2008.09.035.

[71] T. Kirchartz, W. Gong, S.A. Hawks, T. Agostinelli, R.C.I. MacKenzie, Y. Yang, et al., Sensitivity of the Mott–Schottky Analysis in Organic Solar Cells, J. Phys. Chem. C. 116 (2012) 7672–7680. doi:10.1021/jp300397f.

[72] J. Nelson, Diffusion-limited recombination in polymer-fullerene blends and its influence on photocurrent collection, Phys. Rev. B. 67 (2003) 155209. doi:10.1103/PhysRevB.67.155209.

[73] J. Schafferhans, A. Baumann, A. Wagenpfahl, C. Deibel, V. Dyakonov, Oxygen doping of P3HT:PCBM blends: Influence on trap states, charge carrier mobility and solar cell performance, Org. Electron. 11 (2010) 1693–1700. doi:10.1016/j.orgel.2010.07.016.

[74] F.C. Krebs, All solution roll-to-roll processed polymer solar cells free from indium-tin-oxide and vacuum coating steps, Org. Electron. Physics, Mater. Appl. 10 (2009) 761–768. doi:10.1016/j.orgel.2009.03.009.

[75] A. Guerrero, P.P. Boix, L.F. Marchesi, T. Ripolles-Sanchis, E.C. Pereira, G. Garcia-Belmonte, Oxygen doping-induced photogeneration loss in P3HT:PCBM solar cells, Sol. Energy Mater. Sol. Cells. 100 (2012) 185–191. doi:10.1016/j.solmat.2012.01.012.

[76] M. Jørgensen, K. Norrman, F.C. Krebs, Stability/degradation of polymer solar cells, Sol. Energy Mater. Sol. Cells. 92 (2008) 686–714. doi:10.1016/j.solmat.2008.01.005.

[77] M. Jørgensen, K. Norrman, S. a. Gevorgyan, T. Tromholt, B. Andreasen, F.C. Krebs, Stability of polymer solar cells, Adv. Mater. 24 (2012) 580–612. doi:10.1002/adma.201104187.

[78] H. Hintz, H. Peisert, H.-J. Egelhaaf, T. Chassé, Reversible and Irreversible Light-Induced p-Doping of P3HT by Oxygen Studied by Photoelectron Spectroscopy (XPS/UPS), J. Phys. Chem. C. 115 (2011) 13373–13376. doi:10.1021/jp2032737.

[79] J. Zhao, A. Swinnen, G. Van Assche, J. Manca, D. Vanderzande, B. Van Mele, Phase diagram of P3HT/PCBM blends and its implication for the stability of morphology., J. Phys. Chem. B. 113 (2009) 1587–91. doi:10.1021/jp804151a.

[80] B. Walker, A.B. Tamayo, X.-D. Dang, P. Zalar, J.H. Seo, A. Garcia, et al., Nanoscale Phase Separation and High Photovoltaic Efficiency in Solution-Processed, Small-Molecule Bulk Heterojunction Solar Cells, Adv. Funct. Mater. 19 (2009) 3063–3069. doi:10.1002/adfm.200900832.

[81] P.G. Karagiannidis, D. Georgiou, C. Pitsalidis, A. Laskarakis, S. Logothetidis, Evolution of vertical phase separation in P3HT:PCBM thin films induced by thermal annealing, Mater. Chem. Phys. 129 (2011) 1207–1213. doi:10.1016/j.matchemphys.2011.06.007.

[82] J.E. Carlé, T.R. Andersen, M. Helgesen, E. Bundgaard, M. Jorgensen, F.C. Krebs, A laboratory scale approach to polymer solar cells using one coating/printing machine, flexible substrates, no ITO, no vacuum and no spincoating, Sol. Energy Mater. Sol. Cells. 108 (2013) 126–128. doi:10.1016/j.solmat.2012.09.008.

[83] N. Ćelić, E. Pavlica, M. Borovšak, J. Strle, J. Buh, J. Zavašnik, et al., Factors determining large observed increases in power conversion efficiency of P3HT:PCBM solar cells embedded with Mo6S9−xIx nanowires, Synth. Met. 212 (2016) 105–112. doi:10.1016/j.synthmet.2015.12.009.

[84] D. Chen, A. Nakahara, D. Wei, D. Nordlund, T.P. Russell, P3HT/PCBM Bulk Heterojunction Organic Photovoltaics: Correlating Efficiency and Morphology, (2010).

[85] V. Vohra, K. Kawashima, T. Kakara, T. Koganezawa, I. Osaka, K. Takimiya, et al., Efficient inverted polymer solar cells employing favourable molecular orientation, Nat. Photonics. 9 (2015) 403–408. doi:10.1038/nphoton.2015.84.

[86] I. Etxebarria, J. Ajuria, R. Pacios, Solution-processable polymeric solar cells: A review on materials, strategies and cell architectures to overcome 10%, Org. Electron. 19 (2015) 34–60. doi:10.1016/j.orgel.2015.01.014.

[87] A. Kojima, K. Teshima, Y. Shirai, T. Miyasaka, Organometal Halide Perovskites as Visible-Light Sensitizers for Photovoltaic Cells, J. Am. Chem. Soc. 131 (2009) 6050–6051. doi:10.1021/ja809598r.

[88] W.E.I. Sha, X. Ren, L. Chen, W.C.H. Choy, The efficiency limit of $CH_3NH_3PbI_3$ perovskite solar cells, Appl. Phys. Lett. 106 (2015) 221104. doi:10.1063/1.4922150.

[89] G.E. Eperon, S.D. Stranks, C. Menelaou, M.B. Johnston, L.M. Herz, H.J. Snaith, Formamidinium lead trihalide: a broadly tunable perovskite for efficient planar heterojunction solar cells, Energy Environ. Sci. 7 (2014) 982. doi:10.1039/c3ee43822h.

[90] H.-J. Feng, T.R. Paudel, E.Y. Tsymbal, X.C. Zeng, Tunable Optical Properties and Charge Separation in $CH_3NH_3Sn_xPb_{1-x}I_3$ /TiO_2 -Based Planar Perovskites Cells, J. Am. Chem. Soc. 137 (2015) 8227–8236. doi:10.1021/jacs.5b04015.

[91] Q.A. Akkerman, V. D'Innocenzo, S. Accornero, A. Scarpellini, A. Petrozza, M. Prato, et al., Tuning the Optical Properties of Cesium Lead Halide Perovskite Nanocrystals by Anion Exchange Reactions, J. Am. Chem. Soc. 137 (2015) 10276–10281. doi:10.1021/jacs.5b05602.

[92] K. Hwang, Y.-S. Jung, Y.-J. Heo, F.H. Scholes, S.E. Watkins, J. Subbiah, et al., Toward Large Scale Roll-to-Roll Production of Fully Printed Perovskite Solar Cells, Adv. Mater. 27 (2015) 1241–1247. doi:10.1002/adma.201404598.

[93] T.M. Schmidt, T.T. Larsen-Olsen, J.E. Carlé, D. Angmo, F.C. Krebs, Upscaling of Perovskite Solar Cells: Fully Ambient Roll Processing of Flexible Perovskite Solar Cells with Printed Back Electrodes, Adv. Energy Mater. 5 (2015) 1500569. doi:10.1002/aenm.201500569.

[94] F. Matteocci, L. Cinà, F. Di Giacomo, S. Razza, A.L. Palma, A. Guidobaldi, et al., High efficiency photovoltaic module based on mesoscopic organometal halide perovskite, Prog. Photovoltaics Res. Appl. 24 (2016) 436–445. doi:10.1002/pip.2557.

[95] F. Di Giacomo, V. Zardetto, A. D'Epifanio, S. Pescetelli, F. Matteocci, S. Razza, et al., Flexible Perovskite Photovoltaic Modules and Solar Cells Based on Atomic Layer Deposited Compact Layers and UV-Irradiated TiO_2 Scaffolds on Plastic Substrates, Adv. Energy Mater. 5 (2015) 1401808. doi:10.1002/aenm.201401808.

[96] N. Lago, A. Cester, Flexible and Organic Neural Interfaces: A Review, Appl. Sci. 7 (2017) 1292. doi:10.3390/app7121292.

[97] H. Wang, D.H. Kim, Perovskite-based photodetectors: materials and devices, Chem. Soc. Rev. 46 (2017) 5204–5236. doi:10.1039/C6CS00896H.

[98] J.H.L. Ngai, J.K.W. Ho, R.K.H. Chan, S.H. Cheung, L.M. Leung, S.K. So, Growth, characterization, and thin film transistor application of CH 3 NH 3 PbI 3 perovskite on polymeric gate dielectric layers, (n.d.). doi:10.1039/c7ra08699g.

[99] J.R. Harwell, G.L. Whitworth, G.A. Turnbull, I.D.W. Samuel, Green Perovskite Distributed Feedback Lasers, Sci. Rep. 7 (2017) 11727. doi:10.1038/s41598-017-11569-3.

[100] Q. Zhang, R. Su, W. Du, X. Liu, L. Zhao, S.T. Ha, et al., Advances in Small Perovskite-Based Lasers, Small Methods. 1 (2017) 1700163. doi:10.1002/smtd.201700163.

[101] P. Liu, X. He, J. Ren, Q. Liao, J. Yao, H. Fu, Organic–Inorganic Hybrid Perovskite Nanowire Laser Arrays, ACS Nano. 11 (2017) 5766–5773. doi:10.1021/acsnano.7b01351.

[102] Y. Jia, R.A. Kerner, A.J. Grede, A.N. Brigeman, B.P. Rand, N.C. Giebink, Diode-Pumped Organo-Lead Halide Perovskite Lasing in a Metal-Clad Distributed Feedback Resonator, Nano Lett. 16 (2016) 4624–4629. doi:10.1021/acs.nanolett.6b01946.

[103] H. Zhu, Y. Fu, F. Meng, X. Wu, Z. Gong, Q. Ding, et al., Lead halide perovskite nanowire lasers with low lasing thresholds and high quality factors, Nat. Mater. 14 (2015) 636–642. doi:10.1038/nmat4271.

[104] K. Wang, Z. Gu, S. Liu, J. Li, S. Xiao, Q. Song, Formation of single-mode laser in transverse plane of perovskite microwire via micromanipulation, Opt. Lett. 41 (2016) 555. doi:10.1364/OL.41.000555.

[105] S.J. Kim, J. Byun, T. Jeon, H.M. Jin, H.R. Hong, S.O. Kim, Perovskite Light-Emitting Diodes via Laser Crystallization: Systematic Investigation on Grain Size Effects for Device Performance, ACS Appl. Mater. Interfaces. 10 (2018) 2490–2495. doi:10.1021/acsami.7b15470.

[106] B.R. Sutherland, E.H. Sargent, Perovskite photonic sources, Nat. Photonics. 10 (2016) 295–302. doi:10.1038/nphoton.2016.62.

[107] H.J. Snaith, Perovskites: The Emergence of a New Era for Low-Cost, High-Efficiency Solar Cells, J. Phys. Chem. Lett. 4 (2013) 3623–3630. doi:10.1021/jz4020162.

[108] G. Divitini, S. Cacovich, F. Matteocci, L. Cinà, A. Di Carlo, In situ observation of heat-induced degradation of perovskite solar cells, Nat. Energy. 1 (2016) 15012. doi:10.1038/nenergy.2015.12.

[109] G. Niu, X. Guo, L. Wang, Review of recent progress in chemical stability of perovskite solar cells, J. Mater. Chem. A. 3 (2015) 8970–8980. doi:10.1039/C4TA04994B.

[110] N. Wrachien, N. Lago, A. Rizzo, R. D'Alpaos, A. Stefani, G. Turatti, et al., Effects of thermal and electrical stress on DH4T-based organic thin-film-transistors with PMMA gate dielectrics, Microelectron. Reliab. 55 (2015) 1790–1794. doi:10.1016/j.microrel.2015.06.073.

[111] A. Rizzo, A. Cester, N. Wrachien, N. Lago, L. Torto, M. Barbato, et al., Characterization and modeling of organic (P3HT:PCBM) solar cells as a function of bias and illumination, Sol. Energy Mater. Sol. Cells. 157 (2016) 337–345. doi:10.1016/j.solmat.2016.06.001.

[112] X. Dong, X. Fang, M. Lv, Improvement of the humidity stability of organic–inorganic perovskite solar cells using ultrathin Al 2 O 3 layers prepared by atomic layer deposition, J. Mater. Chem. A. 3 (2015) 5360–5367. doi:10.1039/C4TA06128D.

[113] F. Matteocci, L. Cinà, E. Lamanna, S. Cacovich, G. Divitini, P.A. Midgley, et al., Encapsulation for long-term stability enhancement of perovskite solar cells, Nano Energy. 30 (2016) 162–172. doi:10.1016/j.nanoen.2016.09.041.

[114] T. Gatti, F. Lamberti, P. Topolovsek, M. Abdu-Aguye, R. Sorrentino, L. Perino, et al., Interfacial Morphology Addresses Performance of Perovskite Solar Cells Based on Composite Hole Transporting Materials of Functionalized Reduced Graphene Oxide and P3HT, Sol. RRL. 2 (2018) 1800013. doi:10.1002/solr.201800013.

[115] Q. Chen, N. De Marco, Y. (Michael) Yang, T.-B. Song, C.-C. Chen, H. Zhao, et al., Under the spotlight: The organic–inorganic hybrid halide perovskite for optoelectronic applications, Nano Today. 10 (2015) 355–396. doi:10.1016/j.nantod.2015.04.009.

[116] P. Fiorentin, A. Scroccaro, R. Bertani, M. Moronato, F. Simionato, A. Zaggia, Commercial TiO<inf>2</inf> P25 activation: Evaluation of efficacy in photodegration processes of different radiating sources, in: 2014 IEEE Int. Instrum. Meas. Technol. Conf. Proc., IEEE, 2014: pp. 1359–1363. doi:10.1109/I2MTC.2014.6860968.

[117] P.R.F. Barnes, K. Miettunen, X. Li, A.Y. Anderson, T. Bessho, M. Gratzel, et al., Interpretation of Optoelectronic Transient and Charge Extraction Measurements in Dye-Sensitized Solar Cells, Adv. Mater. 25 (2013) 1881–1922. doi:10.1002/adma.201201372.

[118] B. Hwang, J.-S. Lee, Hybrid Organic-Inorganic Perovskite Memory with Long-Term Stability in Air, Sci. Rep. 7 (2017) 673. doi:10.1038/s41598-017-00778-5.

[119] S. van Reenen, M. Kemerink, H.J. Snaith, Modeling Anomalous Hysteresis in Perovskite Solar Cells, J. Phys. Chem. Lett. 6 (2015) 3808–3814. doi:10.1021/acs.jpclett.5b01645.

[120] G. Richardson, S.E.J. O'Kane, R.G. Niemann, T.A. Peltola, J.M. Foster, P.J. Cameron, et al., Can slow-moving ions explain hysteresis in the current–voltage curves of perovskite solar cells?, Energy Environ. Sci. 9 (2016) 1476–1485. doi:10.1039/C5EE02740C.

[121] J. Beilsten-Edmands, G.E. Eperon, R.D. Johnson, H.J. Snaith, P.G. Radaelli, Non-ferroelectric nature of the conductance hysteresis in CH 3 NH 3 PbI 3 perovskite-based photovoltaic devices, Appl. Phys. Lett. 106 (2015) 173502. doi:10.1063/1.4919109.

[122] Y. Shao, Y. Fang, T. Li, Q. Wang, Q. Dong, Y. Deng, et al., Grain boundary dominated ion migration in polycrystalline organic–inorganic halide perovskite films, Energy Environ. Sci. 9 (2016) 1752–1759. doi:10.1039/C6EE00413J.

[123] Z. Xiao, Y. Yuan, Y. Shao, Q. Wang, Q. Dong, C. Bi, et al., Giant switchable photovoltaic effect in organometal trihalide perovskite devices, Nat. Mater. 14 (2015) 193–198. doi:10.1038/nmat4150.

[124] M. De Bastiani, G. Dell'Erba, M. Gandini, V. D'Innocenzo, S. Neutzner, A.R.S. Kandada, et al., Solar Cells: Ion Migration and the Role of Preconditioning Cycles in the Stabilization of the *J* - *V* Characteristics of Inverted Hybrid Perovskite Solar Cells (Adv. Energy Mater. 2/2016), Adv. Energy Mater. 6 (2016). doi:10.1002/aenm.201670009.

[125] M. Bag, L.A. Renna, R.Y. Adhikari, S. Karak, F. Liu, P.M. Lahti, et al., Kinetics of Ion Transport in Perovskite Active Layers and Its Implications for Active Layer Stability, J. Am. Chem. Soc. 137 (2015) 13130–13137. doi:10.1021/jacs.5b08535.

[126] P. Calado, A.M. Telford, D. Bryant, X. Li, J. Nelson, B.C. O'Regan, et al., Evidence for ion migration in hybrid perovskite solar cells with minimal hysteresis, Nat. Commun. 7 (2016) 13831. doi:10.1038/ncomms13831.

[127] C.C. Stoumpos, C.D. Malliakas, M.G. Kanatzidis, Semiconducting tin and lead iodide perovskites with organic cations: phase transitions, high mobilities, and near-infrared photoluminescent properties., Inorg. Chem. 52 (2013) 9019–38. doi:10.1021/ic401215x.

[128] Y. Kutes, L. Ye, Y. Zhou, S. Pang, B.D. Huey, N.P. Padture, Direct Observation of Ferroelectric Domains in Solution-

Processed $CH_3NH_3PbI_3$ Perovskite Thin Films, J. Phys. Chem. Lett. 5 (2014) 3335–3339. doi:10.1021/jz501697b.

[129] K.T. Butler, J.M. Frost, A. Walsh, Ferroelectric materials for solar energy conversion: photoferroics revisited, Energy Environ. Sci. 8 (2015) 838–848. doi:10.1039/C4EE03523B.

[130] H. Guo, P. Liu, S. Zheng, S. Zeng, N. Liu, S. Hong, Re-entrant relaxor ferroelectricity of methylammonium lead iodide, Curr. Appl. Phys. 16 (2016) 1603–1606. doi:10.1016/J.CAP.2016.09.016.

[131] S. Liu, F. Zheng, N.Z. Koocher, H. Takenaka, F. Wang, A.M. Rappe, Ferroelectric Domain Wall Induced Band Gap Reduction and Charge Separation in Organometal Halide Perovskites, J. Phys. Chem. Lett. 6 (2015) 693–699. doi:10.1021/jz502666j.

[132] Y. Zhao, C. Liang, H. Zhang, D. Li, D. Tian, G. Li, et al., Anomalously large interface charge in polarity-switchable photovoltaic devices: an indication of mobile ions in organic–inorganic halide perovskites, Energy Environ. Sci. 8 (2015) 1256–1260. doi:10.1039/C4EE04064C.

[133] J.M. Azpiroz, E. Mosconi, J. Bisquert, F. De Angelis, Defect migration in methylammonium lead iodide and its role in perovskite solar cell operation, Energy Environ. Sci. 8 (2015) 2118–2127. doi:10.1039/C5EE01265A.

[134] E. Mosconi, D. Meggiolaro, H.J. Snaith, S.D. Stranks, F. De Angelis, Light-induced annihilation of Frenkel defects in organo-lead halide perovskites, Energy Environ. Sci. 9 (2016) 3180–3187. doi:10.1039/C6EE01504B.

[135] A.J. Barker, A. Sadhanala, F. Deschler, M. Gandini, S.P. Senanayak, P.M. Pearce, et al., Defect-Assisted Photoinduced Halide Segregation in Mixed-Halide Perovskite Thin Films, ACS Energy Lett. 2 (2017) 1416–1424. doi:10.1021/acsenergylett.7b00282.

[136] Y. Xing, C. Sun, H.-L. Yip, G.C. Bazan, F. Huang, Y. Cao, New fullerene design enables efficient passivation of surface traps in high performance p-i-n heterojunction perovskite solar cells, Nano Energy. 26 (2016) 7–15. doi:10.1016/J.NANOEN.2016.04.057.

[137] Q. Wang, Y. Shao, Q. Dong, Z. Xiao, Y. Yuan, J. Huang, Large fill-factor bilayer iodine perovskite solar cells fabricated by a low-temperature solution-process, Energy Environ. Sci. 7 (2014) 2359–2365. doi:10.1039/C4EE00233D.

[138] W. Nie, H. Tsai, R. Asadpour, J.-C. Blancon, A.J. Neukirch, G. Gupta, et al., Solar cells. High-efficiency solution-processed perovskite solar cells with millimeter-scale grains., Science. 347 (2015) 522–5. doi:10.1126/science.aaa0472.

[139] L.K. Ono, Y. Qi, S. (Frank) Liu, Progress toward Stable Lead Halide Perovskite Solar Cells, Joule. 0 (2018). doi:10.1016/j.joule.2018.07.007.

[140] J. Hu, R. Gottesman, L. Gouda, A. Kama, M. Priel, S. Tirosh, et al., Photovoltage Behavior in Perovskite Solar Cells under Light-Soaking Showing Photoinduced Interfacial Changes, ACS Energy Lett. 2 (2017) 950–956. doi:10.1021/acsenergylett.7b00212.

[141] T. Gatti, E. Menna, M. Meneghetti, M. Maggini, A. Petrozza, F. Lamberti, The Renaissance of fullerenes with perovskite solar cells, Nano Energy. 41 (2017) 84–100. doi:10.1016/J.NANOEN.2017.09.016.

[142] H. Yoon, S.M. Kang, J.-K. Lee, M. Choi, Hysteresis-free low-temperature-processed planar perovskite solar cells with 19.1% efficiency, Energy Environ. Sci. 9 (2016) 2262–2266. doi:10.1039/C6EE01037G.

[143] K. Wojciechowski, T. Leijtens, S. Siprova, C. Schlueter, M.T. Hörantner, J.T.-W. Wang, et al., C_{60} as an Efficient n-Type Compact Layer in Perovskite Solar Cells, J. Phys. Chem. Lett. 6 (2015) 2399–2405. doi:10.1021/acs.jpclett.5b00902.

[144] P. Topolovsek, F. Lamberti, T. Gatti, A. Cito, J.M. Ball, E. Menna, et al., Functionalization of transparent conductive oxide electrode for TiO_2 -free perovskite solar cells, J. Mater. Chem. A. 5 (2017) 11882–11893. doi:10.1039/C7TA02405C.

[145] F. Lamberti, L. Litti, M. De Bastiani, R. Sorrentino, M. Gandini, M. Meneghetti, et al., High-Quality, Ligands-Free, Mixed-Halide Perovskite Nanocrystals Inks for Optoelectronic Applications, Adv. Energy Mater. 7 (2017) 1601703. doi:10.1002/aenm.201601703.

[146] C. Tao, J. Van Der Velden, L. Cabau, N.F. Montcada, S. Neutzner, A.R. Srimath Kandada, et al., Fully Solution-Processed n-i-p-Like Perovskite Solar Cells with Planar Junction: How the Charge Extracting Layer Determines the Open-Circuit Voltage, Adv. Mater. 29 (2017) 1604493. doi:10.1002/adma.201604493.

[147] † Vincenzo Amendola, † Gian Andrea Rizzi, ‡ and Stefano Polizzi, † Moreno Meneghetti*, Synthesis of Gold Nanoparticles by Laser Ablation in Toluene: Quenching and Recovery of the Surface Plasmon Absorption, (2005). doi:10.1021/JP055783V.

[148] J.H. Beaumont, A.J. Bourdillon, J. Bordas, Optical properties of PbI_2 and PbF_2, J. Phys. C Solid State Phys. 10 (1977) 761–771. doi:10.1088/0022-3719/10/5/018.

[149] A.L. Patterson, The Diffraction of X-Rays by Small Crystalline Particles, Phys. Rev. 56 (1939) 972–977. doi:10.1103/PhysRev.56.972.

[150] F. Lamberti, L. Brigo, M. Favaro, C. Luni, A. Zoso, M. Cattelan, et al., Optoelectrochemical Biorecognition by Optically Transparent Highly Conductive Graphene-Modified Fluorine-Doped Tin Oxide Substrates, ACS Appl. Mater. Interfaces. 6 (2014) 22769–22777. doi:10.1021/am506941u.

[151] W. Ren, R. Saito, L. Gao, F. Zheng, Z. Wu, B. Liu, et al., Edge phonon state of mono- and few-layer graphene nanoribbons observed by surface and interference co-enhanced Raman spectroscopy, Phys. Rev. B. 81 (2010) 035412. doi:10.1103/PhysRevB.81.035412.

[152] J.-K. Lee, J.-G. Kim, K.P.S.S. Hembram, Y.-I. Kim, B.-K. Min, Y. Park, et al., The Nature of Metastable AA' Graphite: Low Dimensional Nano- and Single-Crystalline Forms, Sci. Rep. 6 (2016) 39624. doi:10.1038/srep39624.

[153] B. Pałosz, E. Salje, Lattice parameters and spontaneous strain in AX_2 polytypes: CdI_2 , PbI_2 SnS_2 and $SnSe_2$, J. Appl. Crystallogr. 22 (1989) 622–623. doi:10.1107/S0021889889006916.

[154] L. Romano, V. Privitera, C. (Chennupati) Jagadish, L. Romano, Defects in semiconductors, n.d.

[155] M. Tommasini, C. Castiglioni, G. Zerbi, A. Barbon, M. Brustolon, A joint Raman and EPR spectroscopic study on ball-milled nanographites, Chem. Phys. Lett. 516 (2011) 220–224. doi:10.1016/J.CPLETT.2011.09.094.

[156] A. Barbon, M. Brustolon, An EPR Study on Nanographites, Appl. Magn. Reson. 42 (2012) 197–210. doi:10.1007/s00723-011-0285-6.

[157] G.A. Viana, R.G. Lacerda, F.L. Freire, F.C. Marques, ESR investigation of graphite-like amorphous carbon films revealing itinerant states as the ones responsible for the signal, J. Non. Cryst. Solids. 354 (2008) 2135–2137. doi:10.1016/J.JNONCRYSOL.2007.10.063.

[158] G. Volonakis, F. Giustino, Ferroelectric Graphene–Perovskite Interfaces, J. Phys. Chem. Lett. 6 (2015) 2496–2502. doi:10.1021/acs.jpclett.5b01099.

[159] Q. Chen, H. Zhou, T.-B. Song, S. Luo, Z. Hong, H.-S. Duan, et al., Controllable Self-Induced Passivation of Hybrid Lead Iodide Perovskites toward High Performance Solar Cells, Nano Lett. 14 (2014) 4158–4163. doi:10.1021/nl501838y.

[160] T. Takahashi, H. Tokailin, T. Sagawa, Angle-resolved ultraviolet photoelectron spectroscopy of the unoccupied band structure of graphite, Phys. Rev. B. 32 (1985) 8317–8324. doi:10.1103/PhysRevB.32.8317.

[161] O. Leenaerts, B. Partoens, F.M. Peeters, A. Volodin, C. Van Haesendonck, The work function of few-layer graphene, J. Phys. Condens. Matter. 29 (2017) 035003. doi:10.1088/0953-8984/29/3/035003.

[162] Y. Shao, Z. Xiao, C. Bi, Y. Yuan, J. Huang, Origin and elimination of photocurrent hysteresis by fullerene passivation in CH3NH3PbI3 planar heterojunction solar cells, Nat. Commun. 5 (2014) 5784. doi:10.1038/ncomms6784.

[163] A. Walsh, D.O. Scanlon, S. Chen, X.G. Gong, S.-H. Wei, Self-Regulation Mechanism for Charged Point Defects in Hybrid Halide Perovskites, Angew. Chemie Int. Ed. 54 (2015) 1791–1794. doi:10.1002/anie.201409740.

[164] W.-J. Yin, T. Shi, Y. Yan, Unusual defect physics in $CH_3NH_3PbI_3$ perovskite solar cell absorber, Appl. Phys. Lett. 104 (2014) 063903. doi:10.1063/1.4864778.

[165] A. Buin, P. Pietsch, J. Xu, O. Voznyy, A.H. Ip, R. Comin, et al., Materials Processing Routes to Trap-Free Halide Perovskites, Nano Lett. 14 (2014) 6281–6286. doi:10.1021/nl502612m.

[166] M.-H. Du, Density Functional Calculations of Native Defects in $CH_3NH_3PbI_3$: Effects of Spin–Orbit Coupling and Self-Interaction Error, J. Phys. Chem. Lett. 6 (2015) 1461–1466. doi:10.1021/acs.jpclett.5b00199.

[167] D. Meggiolaro, S.G. Motti, E. Mosconi, A.J. Barker, J. Ball, C. Andrea Riccardo Perini, et al., Iodine chemistry determines the defect tolerance of lead-halide perovskites, Energy Environ. Sci. 11 (2018) 702–713. doi:10.1039/C8EE00124C.

[168] V. Adinolfi, M. Yuan, R. Comin, E.S. Thibau, D. Shi, M.I. Saidaminov, et al., The In-Gap Electronic State Spectrum of Methylammonium Lead Iodide Single-Crystal Perovskites, Adv. Mater. 28 (2016) 3406–3410. doi:10.1002/adma.201505162.

[169] F. Lamberti, A. Rizzo, E. Cescon, R. Sorrentino, L. Litti, J. Reguera, et al., Suppression of ionic motions in a perovskite thin film for opto-electronic applications, Submitted (2018).

[170] M.G. Helander, M.T. Greiner, Z.B. Wang, Z.H. Lu, Pitfalls in measuring work function using photoelectron spectroscopy, Appl. Surf. Sci. 256 (2010) 2602–2605. doi:10.1016/J.APSUSC.2009.11.002.

[171] N. Lago, A. Cester, N. Wrachien, M. Natali, S.D. Quiroga, S. Bonetti, et al., A physical-based equivalent circuit model for an organic/electrolyte interface, Org. Electron. 35 (2016) 176–185. doi:10.1016/j.orgel.2016.05.018.

[172] A. Laiho, L. Herlogsson, R. Forchheimer, X. Crispin, M. Berggren, Controlling the dimensionality of charge transport in organic thin-film transistors., Proc. Natl. Acad. Sci. U. S. A. 108 (2011) 15069–73. doi:10.1073/pnas.1107063108.

[173] D.A. Bernards, G.G. Malliaras, Steady-State and Transient Behavior of Organic Electrochemical Transistors, Adv. Funct. Mater. 17 (2007) 3538–3544. doi:10.1002/adfm.200601239.

[174] S.B. Meier, D. Tordera, A. Pertegás, C. Roldán-Carmona, E. Ortí, H.J. Bolink, Light-emitting electrochemical cells: recent progress and future prospects, Mater. Today. 17 (2014) 217–223. doi:10.1016/J.MATTOD.2014.04.029.

[175] J. Tauc, Optical properties and electronic structure of amorphous Ge and Si, Mater. Res. Bull. 3 (1968) 37–46. doi:10.1016/0025-5408(68)90023-8.

[176] T. Baikie, Y. Fang, J.M. Kadro, M. Schreyer, F. Wei, S.G. Mhaisalkar, et al., Synthesis and crystal chemistry of the hybrid perovskite (CH3NH3)PbI3 for solid-state sensitised solar cell applications, J. Mater. Chem. A. 1 (2013) 5628. doi:10.1039/c3ta10518k.

[177] J.R. Harwell, T.K. Baikie, I.D. Baikie, J.L. Payne, C. Ni, J.T.S. Irvine, et al., Probing the energy levels of perovskite solar cells via Kelvin probe and UV ambient pressure photoemission spectroscopy, Phys. Chem. Chem. Phys. 18 (2016) 19738–19745. doi:10.1039/C6CP02446G.

[178] B.C. O'Regan, P.R.F. Barnes, X. Li, C. Law, E. Palomares, J.M. Marin-Beloqui, Optoelectronic studies of methylammonium lead iodide perovskite solar cells with mesoporous TiO2, J. Am. Chem. Soc. 137 (2015) 5087–5099. doi:10.1021/jacs.5b00761.

[179] Y. Zhou, H.F. Garces, N.P. Padture, Challenges in the ambient Raman spectroscopy characterization of methylammonium lead triiodide perovskite thin films, Front. Optoelectron. 9 (2016) 81–86. doi:10.1007/s12200-016-0573-8.

[180] C. Quarti, G. Grancini, E. Mosconi, P. Bruno, J.M. Ball, M.M. Lee, et al., The Raman Spectrum of the $CH_3NH_3PbI_3$ Hybrid Perovskite: Interplay of Theory and Experiment, J. Phys. Chem. Lett. 5 (2014) 279–284. doi:10.1021/jz402589q.

[181] N.A. Davydova, J. Baran, M.K. Marchewka, H. Ratajczak, Interface vibrational modes in layered crystals with stacking faults,

J. Mol. Struct. 404 (1997) 163–165. doi:10.1016/S0022-2860(96)09376-3.

[182] M.Y. Khilji, W.F. Sherman, G.R. Wilkinson, Raman study of three polytypes of PbI2, J. Raman Spectrosc. 13 (1982) 127–133. doi:10.1002/jrs.1250130206.

[183] J.F. Condeles, R.A. Ando, M. Mulato, Optical and structural properties of PbI2 thin films, J. Mater. Sci. 43 (2008) 525–529. doi:10.1007/s10853-007-1854-9.

[184] Y. Yang, Q. Pei, Efficient blue-green and white light-emitting electrochemical cells based on poly[9,9-bis(3,6-dioxaheptyl)-fluorene-2,7-diyl], J. Appl. Phys. 81 (1998) 3294. doi:10.1063/1.364313.

[185] N.N. Shlenskaya, N.A. Belich, M. Grätzel, E.A. Goodilin, A.B. Tarasov, Light-induced reactivity of gold and hybrid perovskite as a new possible degradation mechanism in perovskite solar cells, J. Mater. Chem. A. 6 (2018) 1780–1786. doi:10.1039/C7TA10217H.

[186] V.W. Bergmann, Y. Guo, H. Tanaka, I.M. Hermes, D. Li, A. Klasen, et al., Local Time-Dependent Charging in a Perovskite Solar Cell, ACS Appl. Mater. Interfaces. 8 (2016) 19402–19409. doi:10.1021/acsami.6b04104.

[187] I.G. Hill, A. Rajagopal, A. Kahn, Y. Hu, Molecular level alignment at organic semiconductor-metal interfaces, Appl. Phys. Lett. 73 (1998) 662. doi:10.1063/1.121940.

[188] I.G. Hill, A. Kahn, Energy level alignment at interfaces of organic semiconductor heterostructures, J. Appl. Phys. 84 (1998) 5583–5586. doi:10.1063/1.368864.

[189] Z. Xu, L.-M. Chen, M.-H. Chen, G. Li, Y. Yang, Energy level alignment of poly(3-hexylthiophene): [6,6]-phenyl C[sub 61] butyric acid methyl ester bulk heterojunction, Appl. Phys. Lett. 95 (2009) 013301. doi:10.1063/1.3163056.

[190] L. Bertoluzzi, Cooperative kinetics of depolarization in CH 3 NH 3 PbI 3 perovskite solar cells, Energy Environ. Sci. 8 (2015) 910–915. doi:10.1039/C4EE03171G.

[191] L. Hu, G. Shao, T. Jiang, D. Li, X. Lv, H. Wang, et al., Investigation of the Interaction between Perovskite Films with Moisture via in Situ Electrical Resistance Measurement, ACS Appl. Mater. Interfaces. 7 (2015) 25113–25120. doi:10.1021/acsami.5b06268.

[192] O. Haillant, Accelerated weathering testing principles to estimate the service life of organic PV modules, Sol. Energy Mater. Sol. Cells. 95 (2011) 1284–1292. doi:10.1016/j.solmat.2010.08.033.

[193] N. Espinosa, F.O. Lenzmann, S. Ryley, D. Angmo, M. Hösel, R.R. Søndergaard, et al., OPV for mobile applications: an evaluation of roll-to-roll processed indium and silver free polymer solar cells through analysis of life cycle, cost and layer quality using inline optical and functional inspection tools, J. Mater. Chem. A. 1 (2013) 7037. doi:10.1039/c3ta01611k.

[194] C.J. Mulligan, C. Bilen, X. Zhou, W.J. Belcher, P.C. Dastoor, Levelised cost of electricity for organic photovoltaics, Sol. Energy Mater. Sol. Cells. 133 (2015) 26–31. doi:10.1016/j.solmat.2014.10.043.

[195] C.J. Mulligan, M. Wilson, G. Bryant, B. Vaughan, X. Zhou, W.J. Belcher, et al., A projection of commercial-scale organic photovoltaic module costs, Sol. Energy Mater. Sol. Cells. 120 (2014) 9–17. doi:10.1016/j.solmat.2013.07.041.

[196] C.J. Brabec, Organic photovoltaics: technology and market, Sol. Energy Mater. Sol. Cells. 83 (2004) 273–292. doi:10.1016/j.solmat.2004.02.030.

[197] C. Powell, Y. Lawryshyn, T. Bender, Using stochastic models to determine financial indicators and technical objectives for organic solar cells, Sol. Energy Mater. Sol. Cells. 107 (2012) 236–247. doi:10.1016/j.solmat.2012.06.038.

[198] F. Yan, J. Noble, J. Peltola, S. Wicks, S. Balasubramanian, Semitransparent OPV modules pass environmental chamber test requirements, Sol. Energy Mater. Sol. Cells. 114 (2012) 214–218. doi:10.1016/j.solmat.2012.09.031.

[199] M. Helgesen, J.E. Carlé, G.A. dos Reis Benatto, R.R. Søndergaard, M. Jørgensen, E. Bundgaard, et al., Making Ends Meet: Flow Synthesis as the Answer to Reproducible High-Performance Conjugated Polymers on the Scale that Roll-to-Roll Processing Demands, Adv. Energy Mater. 5 (2015) 1401996. doi:10.1002/aenm.201401996.

[200] M. Vilkman, P. Apilo, M. Välimäki, M. Ylikunnari, A. Bernardi, R. Po, et al., Gravure-Printed ZnO in Fully Roll-to-Roll Printed Inverted Organic Solar Cells: Optimization of Adhesion and Performance, Energy Technol. 3 (2015) 407–413. doi:10.1002/ente.201402155.

[201] National Renewable Energy Laboratory, Research Cell Efficiency, (2016). http://www.nrel.gov/pv/ (accessed January 1, 2016).

[202] M. Jørgensen, J.E. Carlé, R.R. Søndergaard, M. Lauritzen, N.A. Dagnæs-Hansen, S.L. Byskov, et al., The state of organic solar cells—A meta analysis, Sol. Energy Mater. Sol. Cells. 119 (2013) 84–93. doi:10.1016/j.solmat.2013.05.034.

[203] S.A. Gevorgyan, A.J. Medford, E. Bundgaard, S.B. Sapkota, H.-F. Schleiermacher, B. Zimmermann, et al., An inter-laboratory stability study of roll-to-roll coated flexible polymer solar modules, Sol. Energy Mater. Sol. Cells. 95 (2011) 1398–1416. doi:10.1016/j.solmat.2011.01.010.

[204] S.A. Gevorgyan, M. Corazza, M. V. Madsen, G. Bardizza, A. Pozza, H. Müllejans, et al., Interlaboratory indoor ageing of roll-to-roll and spin coated organic photovoltaic devices: Testing the ISOS tests, Polym. Degrad. Stab. 109 (2014) 162–170. doi:10.1016/j.polymdegradstab.2014.07.013.

[205] M. Giannouli, V.M. Drakonakis, A. Savva, P. Eleftheriou, G. Florides, S.A. Choulis, Methods for Improving the Lifetime Performance of Organic Photovoltaics with Low-Costing Encapsulation, ChemPhysChem. 16 (2015) 1134–1154. doi:10.1002/cphc.201402749.

[206] S.A. Gevorgyan, M. V. Madsen, B. Roth, M. Corazza, M. Hösel, R.R. Søndergaard, et al., Lifetime of Organic Photovoltaics: Status and Predictions, Adv. Energy Mater. 6 (2016) 1501208. doi:10.1002/aenm.201501208.

[207] Outlier removal using Hampel identifier - MATLAB hampel - MathWorks Italia, (n.d.). https://it.mathworks.com/help/signal/ref/hampel.html.

[208] V.J. Hodge, J. Austin, A survey of outlier detection methodologies, Artif. Intell. Rev. 22 (2004) 85–126. doi:10.1023/B:AIRE.0000045502.10941.a9.

[209] H. Liu, S. Shah, W. Jiang, On-line outlier detection and data cleaning, Comput. Chem. Eng. 28 (2004) 1635–1647. doi:10.1016/j.compchemeng.2004.01.009.